

Self-Absorption Corrected X-Ray Microtomography with Structural and Elemental Contrast

Dissertation
zur Erlangung des Doktorgrades
an der Fakultät für Mathematik, Informatik und Naturwissenschaften
Fachbereich Physik
der Universität Hamburg

vorgelegt von
Dennis Brückner

Hamburg
2021

Gutachter/innen der Dissertation:

Prof. Dr. Christian G. Schroer
Jun.-Prof. Dr. Peter Modregger

Zusammensetzung der Prüfungskommission:

Prof. Dr. Florian Grüner
Jun.-Prof. Dr. Peter Modregger
Prof. Dr. Wolfgang J. Parak
Prof. Dr. Daniela Pfannkuche
Prof. Dr. Christian G. Schroer

Vorsitzende/r der Prüfungskommission:

Prof. Dr. Wolfgang J. Parak

Datum der Disputation:

29.11.2021

Vorsitzender Fach-Promotionsausschusses PHYSIK:

Prof. Dr. Wolfgang Hansen

Leiter des Fachbereichs PHYSIK:

Prof. Dr. Günter H. W. Sigl

Dekan der Fakultät MIN:

Prof. Dr. Heinrich Graener

Abstract

X-ray fluorescence tomograms of large or highly absorbing samples often suffer from self-absorption effects. For qualitative and quantitative results, it is necessary to correct these effects. In this thesis, a fully 3D self-absorption corrected reconstruction algorithm for X-ray fluorescence tomography datasets is presented. As an extension of the tomographic maximum-likelihood expectation-maximization algorithm, it is an iterative algorithm that reconstructs the density volumes of all measured elements in parallel. The algorithm includes multiple optional parts to aid its convergence, including density and background constraints. Noise may be reduced by using *a priori* information of the sample to introduce a weighted penalty term. All calibration parameters are derived from experimental measurements and small inconsistencies in those values may be corrected by a rudimentary adaptive calibration. Parallel calculations on CPU and GPU as well as downscaling approximations are used to assure high performance of the algorithm and to allow for online reconstruction during experiments.

Numerical simulations of multi-element phantoms without and with added noise confirmed the qualitative as well as quantitative properties of the self-absorption correction. Additionally, tomographic STXM and XRF measurements of a barred olivine micrometeorite were performed at beamline P06 of the PETRA III synchrotron storage ring at DESY in Hamburg, Germany. Although the algorithm was able to correct parts of the self-absorption effects in the micrometeorite data, the qualitative and quantitative properties of the final reconstructions were severely limited by inconsistencies in the experimental calibration, mainly the deadtime and pile-up corrections.

Zusammenfassung

Röntgenfluoreszenztomogramme großer oder stark absorbierender Proben leiden oft an Selbstabsorptionseffekten. Für qualitative und quantitative Ergebnisse ist es notwendig diese Effekte zu korrigieren.

In dieser Arbeit wird ein 3D selbstabsorptionskorrigierter Rekonstruktionsalgorithmus für Röntgenfluoreszenztomographiedatensätze präsentiert. Als eine Erweiterung des tomographischen Maximum-Likelihood Expectation-Maximization Algorithmus ist es ein iterativer Algorithmus der die Dichtevolumen aller gemessenen Elemente parallel rekonstruiert. Der Algorithmus beinhaltet mehrere optionale Teile die die Konvergenz fördern, inklusive Dichte- und Hintergrundbeschränkungen. Rauschen kann reduziert werden, indem *a priori* Informationen über die Probe dazu benutzt werden einen gewichteten Strafterm einzuführen. Alle Kalibrationsparameter sind von experimentellen Messungen abgeleitet und kleine Inkonsistenzen in diesen Werten können mit einer rudimentären adaptiven Kalibrierung korrigiert werden. Parallele Berechnungen auf CPU und GPU sowie Downscaling-Näherungen werden benutzt um eine hohe Performance des Algorithmus sicherzustellen und Online-Rekonstruktion während der Experimente zu ermöglichen.

Numerische Simulationen von Mehrelement-Phantomen ohne und mit zusätzlichem Rauschen bestätigten die qualitativen sowie quantitativen Eigenschaften der Selbstabsorptionskorrektur. Zusätzlich wurden Röntgenabsorptions- und Röntgenfluoreszenzmessungen an einem Barred Olivine Mikrometeoriten an Strahlführung P06 des PETRA III Speicherrings am DESY in Hamburg, Deutschland, durchgeführt. Obwohl der Algorithmus in der Lage war Teile der Selbstabsorptionseffekte in den Mikrometeoritdaten zu korrigieren, haben Inkonsistenzen in der experimentellen Kalibrierung, insbesondere der Totzeit- und Pile-Up-Korrektur, die qualitativen und quantitativen Eigenschaften der finalen Rekonstruktionen eingeschränkt.

Contents

1	Introduction	1
2	Theoretical Background	3
2.1	X-Rays	3
2.1.1	Synchrotron Radiation	3
2.2	Interaction of X-Rays with Matter	6
2.2.1	X-Ray Absorption	6
2.2.2	X-Ray Fluorescence	7
2.3	Optical Elements for X-Rays	9
2.3.1	Double Crystal Monochromator	9
2.3.2	Kirkpatrick-Baez Mirrors	10
3	Experimental Methods	12
3.1	X-Ray Microscopy	12
3.1.1	Principles of Scanning XRM	12
3.1.2	Continuous Motion Scanning	13
3.1.3	Deadtime and Pile-Up	14
3.2	X-Ray Tomography	18
3.2.1	Radon Transform	18
3.2.2	Inverse Radon Transform	20
3.2.3	MLEM Algorithm	23
4	X-Ray Fluorescence Self-Absorption Correction	31
4.1	XRF Self-Absorption	31
4.1.1	Self-Absorption Effects	31
4.1.2	State of the Science	32
4.2	Self-Absorption Correction Algorithm	34
4.2.1	Initial Calculations	34
4.2.2	Self-Absorption Radon Transform	38
4.2.3	Self-Absorption MLEM Algorithm	44
4.2.4	Consistency Refinement Loop	47

4.3	Technical Implementation	53
4.3.1	Dependencies	53
4.3.2	Arrays	53
4.3.3	Downscaling	54
4.3.4	Config-File	56
4.4	Numerical Simulations	57
4.4.1	Phantoms	57
4.4.2	Simulation Parameters	57
4.4.3	Tomographic Reconstruction	59
5	Synchrotron Experiments	67
5.1	Setup	67
5.1.1	PETRA III Beamline P06	67
5.1.2	P06 Tomography Setup	70
5.1.3	Detectors	70
5.2	Experiment	73
5.2.1	Samples	73
5.2.2	Measurements	73
6	Experimental Results	75
6.1	Data Processing	75
6.1.1	XRF Fitting	75
6.1.2	Deadtime and Pile-Up Correction	76
6.1.3	Sorting	78
6.1.4	Calibration	78
6.2	Tomographic Reconstruction	81
6.2.1	Data Alignment	81
6.2.2	MLEM Reconstruction	83
6.3	Volume Analysis	86
7	Conclusion & Outlook	93
	Supplement	95
	Bibliography	105
	Acknowledgments	110
	Eidesstattliche Versicherung / Declaration on oath	112

Chapter 1

Introduction

X-ray fluorescence (XRF) tomography is a nondestructive imaging method used to measure the spatially resolved elemental composition of a sample. Owing to its versatility, it is universally applied in a broad range of research fields, like plant biology, catalysis and medicine. In recent years, for example, XRF tomography was successfully used to image changes in elemental distribution and speciation in plants as a response to viral infections [MMB⁺19], the elemental distribution in seeds [vdESB⁺19] and fronds [vdEdJS⁺20] of plants hyperaccumulating otherwise toxic concentrations of metals, the distribution of metals decreasing the efficiency of catalysts [GVF⁺20], the elemental distribution in Langerhans islets, pancreatic regions that contain insulin producing cells relevant to type 1 diabetes [dSBvM⁺20], as well as the distribution of nanoparticles inside glioblastoma models, used to potentially increase the efficiency of cancer treatments [BBC⁺20].

However, as a type of emission tomography it suffers from self-absorption effects, which are caused by the reabsorption of the emitted signal inside the sample. While the self-absorption effects are often negligible for very small samples or for high energy XRF emission inside low Z sample matrices, they can have a significant influence on qualitative and quantitative properties for measurements of larger or strongly absorbing samples.

With the advancement of science allowing for modern X-ray sources that provide increasingly higher flux and the development of faster stages as well as detectors, X-ray measurements become more and more time efficient. This improved time efficiency may be exploited in multiple ways, for example by measuring more samples, measuring at higher resolutions or measuring larger samples. For larger samples, self-absorption will increasingly become a problem. Thus, it is important to develop a self-absorption correction algorithms that are quantitative and qualitative as well as efficient, to keep up with the experimental measurements.

Aim of this thesis is the development of a fully 3D self-absorption correction algorithm for the qualitative and quantitative reconstruction of XRF tomography datasets. The algorithm will be based on the tomographic maximum-likelihood expectation-maximization (MLEM) algorithm and focus on parallel computation for performance and eventual online reconstruction of tomograms during experiments.

Chapter 2 includes a short overview of basic X-ray theory with a focus on the creation of synchrotron radiation, absorption in matter and x-ray optics.

Chapter 3 covers the topics of X-ray microscopy and tomography. For X-ray microscopy, the discussion focuses on absorption and XRF microscopy, continuous scanning as well as dead-time and pile-up effects. The tomographic part explains the fundamentals of tomographic reconstruction, especially using the MLEM algorithm.

Chapter 4 gives an overview of the general XRF tomography self-absorption problem and the current state of the science regarding self-absorption correction. Furthermore, the chapter includes a detailed derivation of the 3D self-absorption corrected MLEM algorithm, information about its technical implementation as well as numerical simulations to test its performance.

Chapter 5 describes the setup used during the synchrotron experiment, the samples as well as the measurement parameters.

Chapter 6 discusses the data analysis of the tomographic data, including the preprocessing and the reconstruction, as well as qualitative and quantitative aspects of the resulting volumes.

Chapter 7 gives a short summary of the achieved results and an outlook of possible future developments.

Chapter 2

Theoretical Background

2.1 X-Rays

X-rays are electromagnetic waves with photon energies in the range from a few hundreds eV to about 100 keV and wavelengths of a few nanometers down to tens of picometers. Due to their properties, they can be used as probe to gain information about the electronic and geometric structure of samples not accessible otherwise, for example by using visible light or ultraviolet radiation.

2.1.1 Synchrotron Radiation

One method of creating X-rays is to utilize synchrotron radiation. Electrons, or alternatively positrons, are accelerated to relativistic velocities using high frequency voltage and forced onto circular orbits by magnetic electron optics, for example bending magnets.

Bending Magnet Radiation

Due to the Lorentz force caused by the magnetic field of the bending magnets, the electrons are radially accelerated in the direction perpendicular to the magnetic field as well as their moving direction. This acceleration causes the electrons to act as oscillating dipoles and thus to emit dipole radiation, which is linear polarized in the plane of the electron orbit with additional circular components out of plane. As the electrons move at highly relativistic velocities, the toroidal emission pattern of oscillating dipoles in the reference frame of the moving electron resembles a narrow forward cone with a half angle of θ_c in the laboratory frame [Att99]:

$$\theta_c \simeq \frac{1}{2\gamma}, \text{ for } \gamma \gg 1 \quad (2.1)$$

with γ being the Lorentz factor:

$$\gamma = \frac{1}{\sqrt{1 - \frac{v^2}{c^2}}} \quad (2.2)$$

where v is the velocity of the electrons and c the speed of light. This bending magnet radiation exhibits a broad energy spectrum with a critical energy E_c of:

$$E_c = \frac{3e\hbar B\gamma^2}{2m} \quad (2.3)$$

where e is the elementary charge, B the magnetic flux density of the magnetic field and m the mass of accelerated charged particle. Per definition, the critical energy E_c is the energy at which half of the emitted power is radiated at lower and the other half at higher energies.

Insertion Devices

The concept of bending magnet radiation can be expanded on by utilizing arrays of magnets creating a series of antiparallel magnetic fields. These insertion devices, depending on their properties either called undulators or wigglers, force electrons on a sinusoidal path, causing them to emit dipole radiation over longer distances than it would be the case for single bending magnets. Their properties are mainly defined by the undulator parameter K [Att99]:

$$K = \frac{eB_0\lambda_u}{2\pi mc} \quad (2.4)$$

where B_0 is the amplitude of the periodic magnetic field and λ_u the period of the magnetic structure. Usually, the period of the magnet structure is a constant parameter of the insertion device, while the amplitude of the magnetic field can be modified by changing the size of the vertical gap between the magnetic poles.

For small magnetic amplitudes and short magnet periods the undulator parameter will be $K \leq 1$, in which case the insertion device is called an undulator. In this case the amplitude of the oscillating electron beam is smaller than the natural opening angle $2\theta_c$ of the forward radiation cone emitted by each of the electrons (eq. 2.1). This allows the emitted radiation from each electron to overlap coherently, causing the generation of harmonic radiation with small bandwidths as described by the undulator equation:

$$\lambda_n = \frac{\lambda_u}{2\gamma^2 n} \left(1 + \frac{K^2}{2} + \gamma^2 \theta_o^2 \right) \quad (2.5)$$

where λ_n is the wavelength generated by the n -th harmonic of the undulator and θ_o the observation angle from the central undulator axis. It has to be noted that the odd and even harmonics do have different radiation patterns, with the odd harmonics radiating mainly on the central axis. In contrast, the even harmonics are only observable off-axis as they are generated by oscillations parallel to the electron beam moving direction.

As the wavelength of the emitted radiation is dependent on its angle from the central axis, the concept of a central radiation cone defined by its bandwidth $\lambda/\Delta\lambda = N$ is introduced, where N is the number of undulator periods. In this case, it can be calculated that the opening angle of the central cone θ_{cen} is narrowed down by a factor of about $1/\sqrt{N}$ compared to the bending magnet case:

$$\theta_{\text{cen}} = \frac{\sqrt{1 + K^2/2}}{\gamma\sqrt{N}} \approx \frac{1}{\gamma\sqrt{N}}, \text{ for small } K \quad (2.6)$$

Overall, the advantages of undulator radiation over bending magnet radiation are thus an increased photon flux, a smaller spectral bandwidth as well as a narrowed radiation cone.

On the other hand, if the magnetic strength of an insertion device is high enough that the undulator parameter $K > 1$, the amplitude of the oscillating electron beam will exceed the size of the natural radiation cone and the insertion device is called a wiggler. In this case, the emitted radiation cones of each electron do not overlap coherently but incoherently instead. This still leads to an increase in photon flux by a factor of $2N$ compared to the bending magnet case, but also causes the spectrum of the wiggler to resemble the broad spectrum of a bending magnet and increases the horizontal width of the total radiation cone by about a factor of K .

2.2 Interaction of X-Rays with Matter

The interactions of X-rays with matter include effects like absorption, scattering and refraction. This work will limit its focus on the description of X-ray absorption and, in extension, of X-ray fluorescence.

2.2.1 X-Ray Absorption

X-ray photons may be absorbed in matter by interacting with the bound electrons of its atoms. If the photon energy is high enough, this interaction may induce the emission of formerly bound electrons into the continuum, leading to electron vacancies in the atomic shell.

On a macroscopic level, the transmitted intensity I of a beam with an initial intensity I_0 after propagating a distance d through a homogeneous sample can be calculated by the Beer-Lambert law [ANM11]:

$$I = I_0 \cdot e^{-\tau_{abs}(E)} = I_0 \cdot e^{-\mu_{abs}(E) \cdot d} \quad (2.7)$$

where $\tau_{abs}(E)$ is the energy dependent optical depth of the sample and $\mu_{abs}(E)$ the energy dependent linear absorption coefficient. For inhomogeneous samples, the optical depth is instead calculated as the integral over the absorption coefficient along the beam path:

$$\tau_{abs}(E) = \int_0^d \mu_{abs}(E, x) dx \quad (2.8)$$

Assuming the sample consists of j different types of atoms with volume mass densities $\rho_{3D,j}$ and energy dependent absorption cross sections $\sigma_{abs,j}(E)$, the linear absorption coefficient can be expressed as:

$$\mu_{abs}(E) = \sum_j \frac{N_A}{M_j} \rho_{3D,j} \sigma_{abs,j}(E) \quad (2.9)$$

where N_A is the Avogadro constant and M_j the molar mass of atom type j . Combining the equation for the optical depth with equation 2.9 then leads to a description of the optical depth dependent on the area mass density $\rho_{2D} = \rho_{3D} \cdot d$ in the plane intersected by the beam:

$$\tau_{abs}(E) = d \sum_j \frac{N_A}{M_j} \rho_{3D,j} \sigma_{abs,j}(E) = \sum_j \frac{N_A}{M_j} \rho_{2D,j} \sigma_{abs,j}(E) \quad (2.10)$$

The energy dependent absorption coefficients for Ti, Fe and Zn are plotted in figure 2.1. It can be seen that the absorption coefficients generally decrease with higher X-ray energies, except at certain specific energies at which they increase with a strong rise. These energies are equivalent to the binding energies E_B of the electrons in the atoms and called absorption edges. If the energy of the incident X-rays is equivalent to the energy of an absorption edge, the X-rays are absorbed resonantly. The resonant absorption is explained by Fermi's Golden Rule, which states

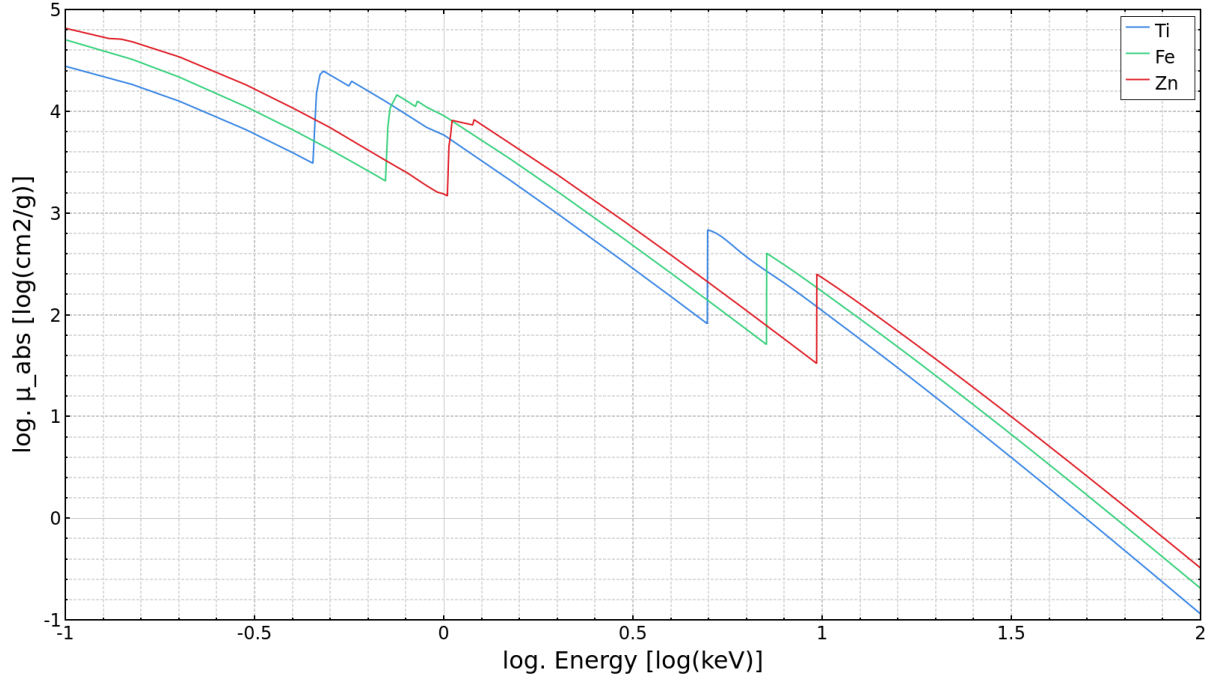


Figure 2.1: $\text{Log}_{10}\text{-log}_{10}$ plot of the energy dependent absorption coefficient for Ti, Fe and Zn in the energy range between 0.1 keV and 100 keV.

that during the absorption process the transition rate W between the initial bound state $|i\rangle$ and the final continuum state $|f\rangle$ is proportional to the absolute squared of the scaled overlap of the two states [ANM11]. This overlap has a maximum for excitation energies equal to the electron binding energies. If the excitation energy is increased further, the overlap, the transition rate, and therefore in extension also the absorption cross section, decrease.

Furthermore, as can be seen in figure 2.1, the change of the energy dependent absorption coefficients between the absorption edges can be approximated by linear functions in the $\text{log}_{10}\text{-log}_{10}$ plot. Empirically, this behavior can be described by Leroux's scaling law [Ler61]:

$$\mu_{abs}(E) \propto E^\gamma \quad (2.11)$$

where γ is an empirical scaling parameter. The exact value of the scaling parameter changes depending on the element in question and the considered region of energy in relation to the absorption edges of the element, but typically lies in the range $-3 \leq \gamma \leq -2.7$.

2.2.2 X-Ray Fluorescence

The absorption of an X-ray photon and the following emission of a core electron creates a vacancy in a core energy level of atomic shell. This vacancy can be filled by an electron from a higher energetic level, as long as the transition into the vacant energy level is quantum mechanically allowed [Att99]. During the transition, the electron releases an energy ΔE equivalent to the difference between its former higher and new lower energetic level. There are two main pathways this energy may be released.

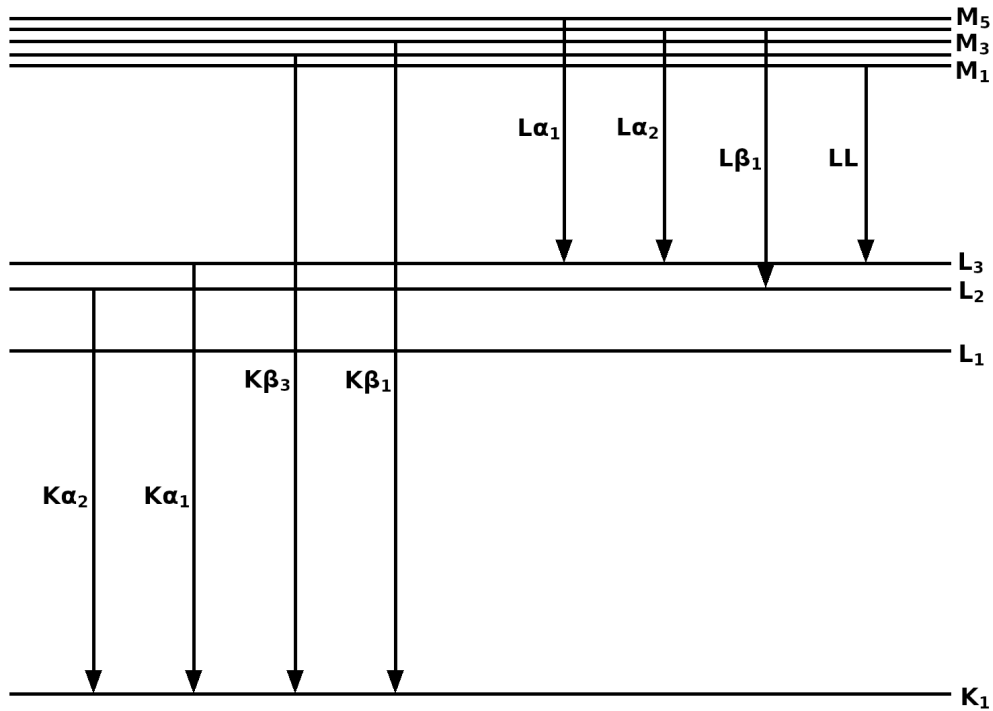


Figure 2.2: Example transitions between electronic energy levels and their corresponding XRF emission lines (following [T⁺09]).

For one, the energy can be directly emitted as a photon with an energy $\hbar\omega = \Delta E$ in a radiative process known as X-ray fluorescence (XRF). This emission is isotropic and thus covers the full solid angle of 4π . Depending on the initial and the final energy level of the electron that is filling the vacancy, the nomenclature of the transition and, in extension, of the corresponding emission line changes. Figure 2.2 shows a selection of allowed transitions between electronic levels and their naming in Siegbahn notation. Alternatively, the transitions may be named directly using the involved electronic levels (IUPAC notation). In cases in which multiple lines cannot be energetically resolved, the resulting combined line is named after their lowest common denominator. A combination of the $K\alpha_1$ and $K\alpha_2$ line, for example, would be a $K\alpha$ line.

As a consequence of the multitude of electronic transitions, the emitted XRF radiation usually encompasses an array of different energies unique to the type of absorbing atom. Each possible transition gives rise to a separate emission line, potentially leading to complex XRF spectra.

Alternatively, the released energy can lead to the emission of an electron from a higher energy level, as long as it is higher or equal than the binding energy of this electron $E_b \leq \Delta E$. This non-radiative process is called Auger emission and the emitted electron an Auger electron. Following the conservation of energy, the kinetic energy of the Auger electron can then be calculated as $E = \Delta E - E_b$.

As Auger emission is a competing process to X-ray fluorescence, it has to be considered in the planning of XRF experiments. As a general tendency, Auger emission is favored in atoms with low atomic number Z . With increasing Z , the relative yield of both processes shifts towards X-ray fluorescence [Att99].

2.3 Optical Elements for X-Rays

As the interaction of X-rays with matter differs from those of visible light, most elements utilized in classical optics cannot or can only be used in limits to modify X-rays. It is therefore important to develop and use special optical elements for X-ray experiments. Two of the optical elements suited for the manipulation of X-ray radiation are the double crystal monochromator and the Kirkpatrick-Baez mirrors.

2.3.1 Double Crystal Monochromator

A double crystal monochromator is an optical element that utilizes the diffraction of X-rays at a crystal lattice to monochromatize polychromatic X-ray beams.

If an X-ray beam interacts with the lattice of a crystal, it is scattered by the different atoms of the lattice. Assuming an elastic process, the scattered X-rays are able to interfere with each other. Because of the periodicity of the crystal lattice, this interference is destructive, except in cases in which the Bragg condition is met [Att99]:

$$n\lambda = 2d \sin \theta \quad (2.12)$$

where n is an arbitrary positive integer, λ the wavelength of the X-rays, d the distance between the planes of the periodic crystal lattice and θ the incident angle of the X-rays. Thus, it is possible to monochromatize an X-ray beam by tuning its incident angle on a crystal monochromator in such a way that only the desired wavelength is diffracted.

However, real crystal monochromators are not perfect and flawed crystal structures as well as surfaces may lead to the diffraction of wavelengths other than the desired one. These effects may be amplified by the high heat load caused by an intense X-ray beam, leading to thermal distortion of the crystal and further reducing its performance [ANM11]. In addition, the process of diffraction changes the direction of the X-ray beam as a function of the incident angle, which may be inconvenient depending on the experimental setup.

To mitigate these drawbacks, a combination of multiple crystal monochromators may be used instead of just a single one. The Bragg condition has to be met for all of the separate crystal monochromators. In this way, each subsequent crystal further suppresses the undesired wavelengths diffracted by the crystals before.

Figure 2.3 a) shows a schematic overview of the beam path through a double crystal monochromator. Both crystal are aligned in such a way that the Bragg condition is met for the X-ray beam with wavelength λ . Furthermore, due to the parallel geometry of the crystals, the exiting beam is parallel to the incident beam. This allows to utilize the double crystal monochromator at different X-ray energies without changing the direction of the beam.

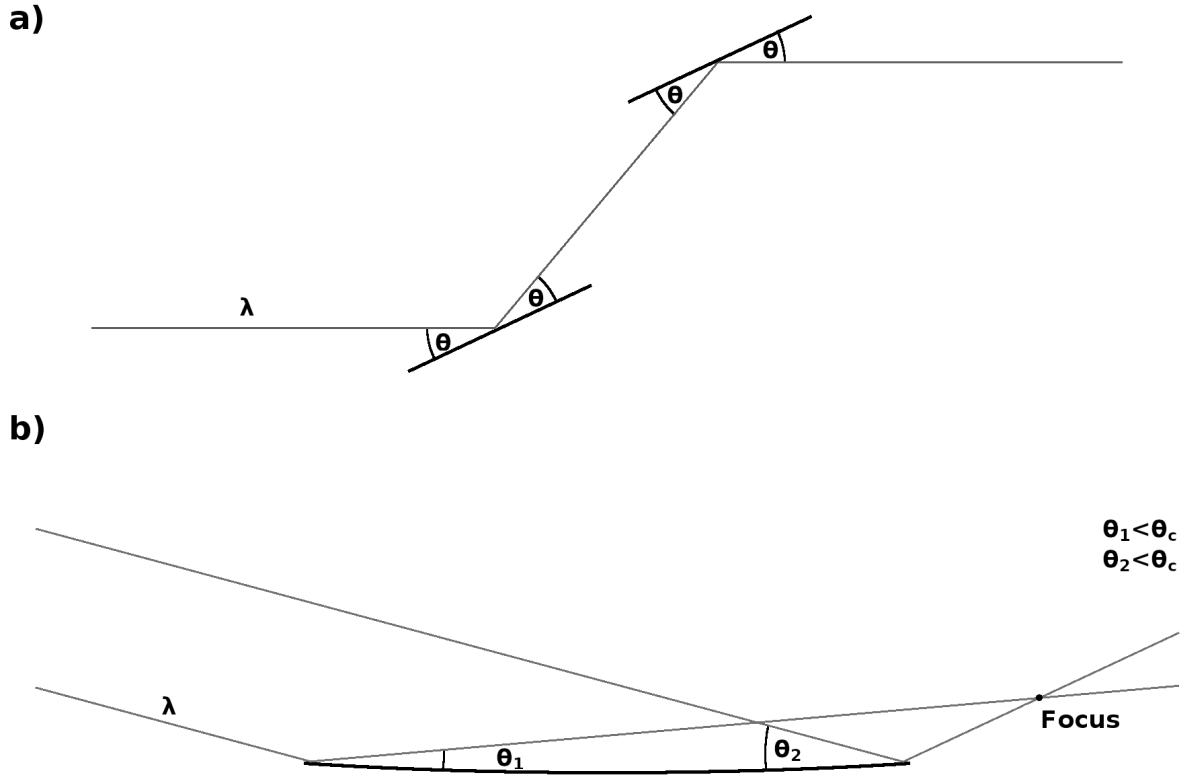


Figure 2.3: Schematic overview of the beam path in a) a double crystal monochromator and b) a single KB-mirror.

2.3.2 Kirkpatrick-Baez Mirrors

A Kirkpatrick-Baez (KB) mirror system is an optical element consisting of two elliptically curved mirrors used to focus X-ray beams. As each of these mirrors only focuses in one direction (fig. 2.3 b), the two mirrors are usually placed orthogonal to each other to allow for horizontal as well vertical focusing.

One of the main principles of a KB-mirror is the total external reflection of X-rays. The complex refractive index of a homogeneous medium for electromagnetic waves with an angular frequency of ω is given by [Att99]:

$$n(\omega) = 1 - \delta + i\beta \quad (2.13)$$

where the real part $1 - \delta$ is defined by the scattering properties of the medium and the imaginary part $i\beta$ by its absorption properties. By calculating the real part of the refractive index, it can be shown that $0 < \delta \ll 1$ inside the energy range occupied by X-rays and therefore $\Re\{n\} < 1$. Thus, for X-rays the refractive index of the vacuum is larger than the refractive index of other media, allowing for total external reflection. Utilizing Snell's law, the critical angle for total external reflection θ_c can be calculated using:

$$\theta_c = \sqrt{2\delta} \quad (2.14)$$

Each X-ray wave coming from vacuum and grazing a medium with an incident angle smaller than θ_c is nearly completely reflected by the surface of the medium. KB-mirrors, utilizing this effect, therefore tend to have a higher flux efficiency as other X-ray focusing optics, for example compound refractive lenses or Fresnel zone plates.

Another advantage of KB-mirrors over other focusing optics is their achromaticity. The angle of reflection is independent of the X-ray energy. As long as the incident angle of the reflected radiation is smaller than the critical angle, the influence of varying energy on the focusing is negligible. Experiments that require frequent X-ray energy changes can thus be performed without adjusting the experimental geometry between measurements.

The critical angle is dependent on the real part of the refractive index (eq. 2.14) and thus on the energy of the incident X-rays. It can be shown that the critical angle has a general tendency to decrease for higher energies. This can be exploited for higher order suppression. Assuming an X-ray source emitting multiple harmonics of increasing energy, for example an undulator, the KB-mirrors can be tilted in such a way that the critical angle is larger than the incident angle for the lower harmonics but smaller for the higher harmonics. In that case, total external reflection only applies to the lower harmonics, while the higher harmonics are suppressed. However, this can also be a disadvantage if the geometry of the KB-mirrors is fixed, as it would introduce a maximum cut-off energy above which the usage of the KB-mirrors is not feasible anymore.

Chapter 3

Experimental Methods

3.1 X-Ray Microscopy

X-ray microscopy (XRM) encompasses different experimental techniques of imaging samples using X-rays as a probe. Owing to the penetrative properties of X-rays, XRM is more suited to investigate the inner structures and properties of samples compared to optical or electron microscopy. Measurements may be performed using either full-field or scanning methods, depending on the requirements of the employed imaging modalities.

3.1.1 Principles of Scanning XRM

The basic principle of scanning XRM is the movement of a sample through a small, often focused, X-ray beam to achieve spatially resolved information on the properties of this sample. In some cases, especially if a sample is difficult to move, the X-ray beam may be scanned over the stationary sample instead. Modalities of scanning XRM include, for example, X-ray absorption, X-ray fluorescence, wide- and small-angle X-ray scattering, as well as coherent diffractive imaging. In comparison to full-field XRM, the spatially resolved modalities of scanning XRM cover a wider range. However, considering the time requirements of moving samples through the beam, scanning XRM measurements are usually slower than full-field XRM measurements, necessitating the development of fast scanning methods.

X-Ray Absorption Microscopy

Scanning transmission X-ray microscopy (STXM) is used to measure the spatially resolved projected optical depth τ of a sample. The transmission of an X-ray beam through the sample is measured by a detector placed directly downstream of or behind the sample.

Normalization of the transmitted intensity I to the incident intensity I_0 can be performed by either using the intensity data of an additional detector upstream of the sample or, if possible, by using the transmitted intensity measured by the downstream detector in regions with no sample in the beam. The former case requires the correct calibration of both detectors to each

other, while in the latter case fluctuations of the incident beam may be missed in regions where the sample is in the beam. To mitigate these drawbacks, both methods may be combined by first qualitatively normalizing the transmission data to uncalibrated incident intensity data of an upstream detector, followed by a quantitative normalization to the non-sample transmitted intensity data of the downstream detector.

After the measurement and normalization, the optical depth τ is calculated from the intensity ratio I/I_0 using the Beer-Lambert law (eq. 2.7).

X-Ray Fluorescence Microscopy

Scanning XRF microscopy is used to measure the spatially resolved elemental composition of a sample. As the XRF signal is emitted isotropically, the placement of the spectrally resolved XRF detector in relation to the sample is variable. However, there are some considerations that have to be made. To collect as much XRF signal as possible, the detector should be close to the sample. For horizontally polarized synchrotron radiation, placing the detector perpendicular to the X-ray beam reduces the influence of elastic and inelastic X-ray scattering on the spectra [PPK⁺14]. However, depending on the sample size and geometry, this may not be ideal. Especially for extended 2D samples, detectors placed perpendicular to the X-ray beam and close to the sample may interfere with the scanning geometry. For this reason, some detectors operate in “backscattering” geometry, sacrificing the reduction in scatter signal for larger scanning ranges at small sample-detector distances.

Independent of the placement of the detector, the result of a scanning XRF microscopy measurement will be a full XRF spectrum for every position of the scan. Depending on the composition of the sample, these spectra may consist of a variety of overlapping XRF emission lines. For this reason, the spectra have to be fitted to extract meaningful elemental information. Depending on the objective of the measurements, the fitted data may then be normalized and calibrated further. The final results are spatially resolved maps, showing the element specific distributions in the scanned regions of the sample.

3.1.2 Continuous Motion Scanning

Compared to full-field microscopy methods, scanning microscopy methods can be slow and time consuming. This is especially a problem if experimental time is limited. Modern scanning schemes, for example continuous motion or fly-scanning, can be employed to mitigate this problem.

A common scanning scheme for scanning X-ray microscopy is the step-scan. In this scheme, the scanning motors move the sample to a predetermined position and stop. Following that, the measurement is performed and the sample is moved to the next position. Therefore, the time spent at every scan point is made up of three separate times: First, the overhead time t_o the scanning stages require to accelerate, move to the requested position and to decelerate. Second, the time t_d it takes for the detectors to be ready for the exposure and finally the exposure time t_e

itself. The fraction of time w_{step} not used for the exposure for step-scans can then be defined as [DNC⁺15]:

$$w_{step} = \frac{t_o + t_d}{t_e + t_o + t_d} \quad (3.1)$$

In the case of fly-scanning the stages are moved continuously, without stopping at certain positions. Thus, the detectors are exposed while the sample is moving, effectively eliminating the overhead time t_o . Acceleration and deceleration is only required in the turning points at the edges of the scanned area. As the time spent at the turning points is usually only a small part of the entire scanning time, the fraction of time w_{fly} not used for the exposure during fly-scans can be calculated as:

$$w_{fly} = \frac{t_d}{t_e + t_d} \quad (3.2)$$

Assuming fast measurements with piezo-scanners as sample stages and an 1D XRF detector, realistic values would be in the order of $t_o = 10$ ms, $t_d = 100$ ns and $t_e = 2.75$ ms. Using these values, the fraction of time not spent on exposure is $w_{step} = 0.784$ for step-scans and $w_{fly} = 3.67 \cdot 10^{-5}$ for fly-scans. As can be seen, more than three fourths of the total required time for the step-scan is made up of movement overhead, while the total required time for the fly-scan is only slightly larger than the sum of all exposures would be. In this specific case, the fly-scan would be more than four times faster than the step-scan.

However, there are disadvantages to the fly-scanning approach. As the stages are moving constantly, data acquisition is more challenging. For example, the scanning stages need encoders to correctly correlate the time of exposure with their location in space. Furthermore, as the measurements are not taken at predetermined points but over certain distances, the spatial resolution along the scanning direction may be worse than it would be for step-scans. Also, with the measured points not being on a perfect grid, interpolation is required to sort the measured data into images, further worsening the resolution.

3.1.3 Deadtime and Pile-Up

Two additional effects important to consider for XRM measurements, especially for quantitative XRF measurements at high input count rates (ICR), are the detector deadtime losses and pulse pile-up. These effects lead to a reduction of the measured output count rates (OCR) compared to the ICR as well as artifact peaks in the XRF spectra.

Deadtime

After an event is detected inside a detector, the associated electronics require a certain amount of time to analyze the event and prepare the detector for the measurement of the next event. This time is called the deadtime of the detector and, in most cases, all events that occur inside the detector during this time are discarded. Thus, the deadtime leads to a reduction of measured

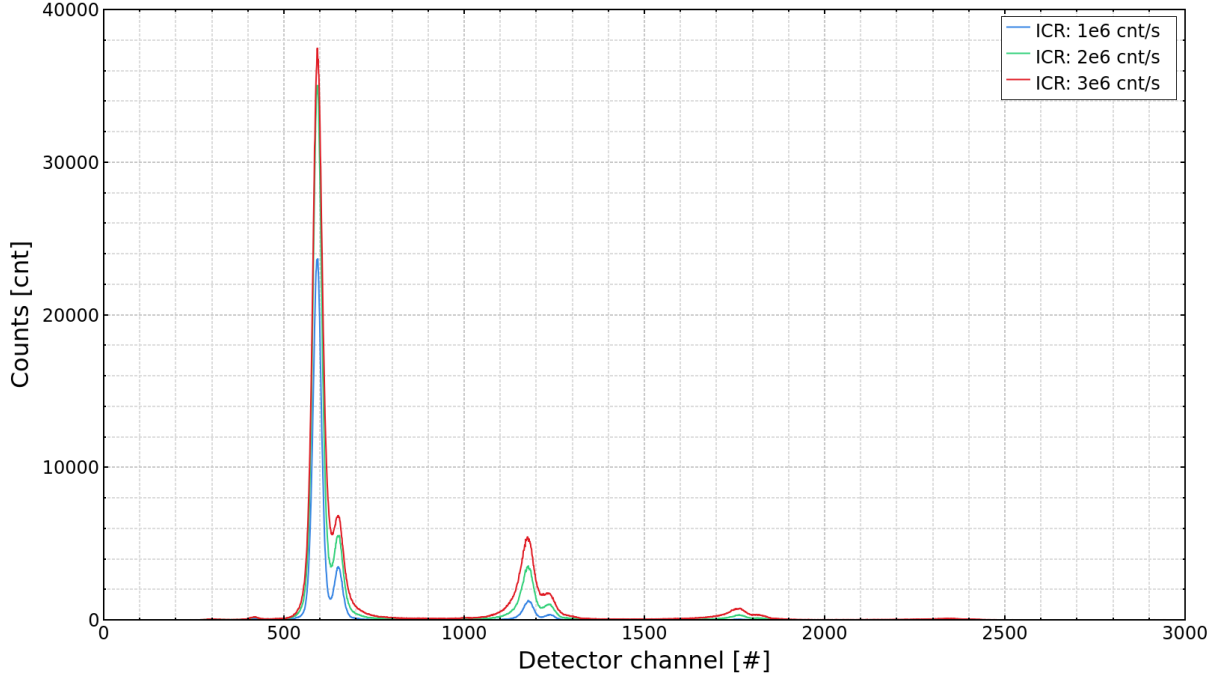


Figure 3.1: XRF spectra of a Mn-foil measured at an excitation energy of 7 keV, plotted for different input count rates. Each detector channel has a width of about 0.01 keV. The region between channel 500-700 mainly contains the Mn-K peaks. All peaks above channel 700 are caused by pulse pile-up.

count rate compared to the expected count rate. As deadtime losses can skew the results of quantitative measurements towards lower values, it is of importance to characterize the deadtime and correct for the resulting losses.

Figure 3.1 shows three XRF spectra measured using a Mn-foil. Focusing on the area of the Mn-K peaks between detector channel 500-700 illustrates the influence of deadtime losses on the quantitativity of the measurement. From assuming Gaussian shaped peaks with fixed FWHM and an amount of detected XRF photons which, in the ideal case, should be proportional to the ICR, it would follow that the heights of the measured peaks should also be proportional to the ICR. However, comparing the peak heights in the data, it is apparent that the increase of peak height reduces with higher ICR.

There are two idealized theories to describe the influence of deadtime on the OCR. The first, type I, assumes a nonparalyzable deadtime model, while the second, type II, assumes a paralyzable deadtime model [UP18]. Both of these models assume a Poisson distributed input at the detector.

In the nonparalyzable deadtime model every event inside the detector starts a deadtime τ_N during which all other occurring events are ignored. The duration of this deadtime is constant and after it expires events are recognized normally again. Mathematically, the effect of a nonparalyzable deadtime on the OCR can be described by equation 3.3 [UP18]:

$$\frac{\text{OCR}}{\text{ICR}} = 1 - \text{OCR} \cdot \tau_N \Leftrightarrow \text{ICR} = \frac{\text{OCR}}{1 - \text{OCR} \cdot \tau_N} \Leftrightarrow \text{OCR} = \frac{\text{ICR}}{1 + \text{ICR} \cdot \tau_N} \quad (3.3)$$

Evaluating equation 3.3 in the high ICR limit leads to the OCR approaching a value of $1/\tau_N$. Thus, the maximum OCR in the nonparalyzable model is a constant value.

In the paralyzable deadtime model every event inside the detector starts a deadtime τ_p . However, in contrast to the nonparalyzing case, every event occurring during this deadtime is not only ignored, but also extends the current deadtime by an additional τ_p . Only after the entire deadtime passes are events recognized again. Equation 3.4 describes this effect mathematically [UP18]:

$$\text{OCR} = \text{ICR} \cdot e^{-\text{ICR} \cdot \tau_p} \quad (3.4)$$

The high ICR limit of equation 3.4 approaches 0. In the paralyzable model it is possible to completely paralyze the detector, meaning that no events are detected.

Real systems rarely can be sufficiently described using only one of the idealized models as their response usually lies in between the two cases. Combining the nonparalyzable (eq. 3.3) and the paralyzable deadtime model (eq. 3.4) leads to a hybrid deadtime model [UP18]:

$$\text{OCR} = \frac{\text{ICR} \cdot e^{-\text{ICR} \cdot \tau_p}}{1 + \text{ICR} \cdot \tau_N} \quad (3.5)$$

which improves the description of the cases that do not fall under one of the idealized models.

Pile-Up

Pulse pile-up occurs when two or more photons get detected in a smaller time frame than the time resolution of the detector system τ_T . They cannot be resolved as independent events anymore and get detected as an event at an energy which is equal to the sum of energies of the individual events.

The effect of pulse pile-up on XRF spectra can be seen in figure 3.1. With an excitation energy of 7 keV, there should not be any peaks in the spectra above channel 700. However, the pile-up gives rise to multiple additional peak-regions: A 2-event pile-up region between channel 1000 and 1300, a 3-event pile-up region between channel 1600 and 1900 and for higher ICR even a 4-event pile-up region between channel 2200 and 2500.

The most simple model to describe pile-up assumes that the 2-event pile-up peak is the main component of all pile-up peaks, which is the case at lower ICR. Assuming Poisson distributed events, the ratio of the 2-event pile-up peaks S_2 and the single-event peaks S_1 can be described by equation 3.6 [BFG⁺19]:

$$\frac{S_2}{S_1} = \frac{PP(2, \tau_T \cdot \text{ICR})}{1 - e^{-\text{ICR} \cdot \tau_T}} \approx \frac{\text{ICR} \cdot \tau_T}{2} \quad (3.6)$$

where $PP(N, M)$ describes the Poisson probability to measure N events during the normalized mean $M = \text{ICR} \cdot \tau_T$, calculated following equation 3.7:

$$PP(N, M) = M^N \cdot \frac{e^{-M}}{N!} \quad (3.7)$$

and the right side of equation 3.6 follows from a first order approximation of the series expansion of the exponential function.

Combined Theory

Combining the equation for the hybrid deadtime model (eq. 3.5) and the equation defining the decrease of the intensity of the single-event peaks from the pulse pile-up model (eq. 3.6) leads to a model which describes the effect of deadtime and pile-up simultaneously [BFG⁺19]:

$$\text{OCR} = \frac{\text{ICR} \cdot ((e^{-\text{ICR} \cdot \tau_p}) + (1 - e^{-\text{ICR} \cdot \tau_T}))}{1 + \text{ICR} \cdot \tau_N} \quad (3.8)$$

However, as the pile-up model was derived with the assumption that the 2-event pile-up peak is the main component of all pile-up peaks, this equation may only be correct at lower ICR and become physically inaccurate at higher ICR.

3.2 X-Ray Tomography

X-Ray Tomography is a nondestructive, multi-modal imaging technique which uses multiple 1D projections of a physical property of a sample measured from different angular directions to reconstruct a 2D slice, or distribution, of this property. By measuring 2D projections of the sample and combining the resulting 2D slices, a 3D volume of the sample can be created.

3.2.1 Radon Transform

Mathematically, the tomographic measurement of recording multiple 1- or 2-dimensional projections of a sample property from different angular directions can be modeled by the Radon transform. The Radon transform describes the interaction of a beam with a sample as it passes through it and as such may vary for different measurement modes. While more simple measurement modes, such as absorption tomography, may be sufficiently described using only the distribution of one single physical parameter inside the sample, the Radon transforms describing more complex measurement modes, like emission tomography, may also require to include additional information about the sample, for example to describe the absorption of the emitted signal before it is detected. The following discussion of the Radon transform assumes the simple case of parallel beam absorption tomography.

The starting point for the Radon transform is a 2D image function $f(x,y)$ describing the distribution of a physical property, for example the optical depth as described in equation 2.10, inside the sample. Assuming the x - y -coordinate system of the image function is rotated by an angle φ into the t - s -coordinate system:

$$\begin{bmatrix} t \\ s \end{bmatrix} = \begin{bmatrix} \cos \varphi & \sin \varphi \\ -\sin \varphi & \cos \varphi \end{bmatrix} \begin{bmatrix} x \\ y \end{bmatrix} \quad (3.9)$$

the projection $P_\varphi(s)$ along the t -axis (fig. 3.2 a) can be described by the integral Radon transform [KS88]:

$$P_\varphi(s) = \int_{-\infty}^{\infty} f(t,s) dt \quad (3.10)$$

In most real-world cases, the values of the image function are not defined continuously but limited to discrete values, for example the pixel positions of an image. For those cases, the integral of the Radon transform changes into a sum:

$$P_\varphi(s) = \sum_t f(t,s) \quad (3.11)$$

It has to be noted that the calculation of this discrete Radon transform requires interpolation if the t - s -coordinates correspond to interpixel x - y -coordinates.

The combination of multiple projections measured from different angular directions φ_i into a

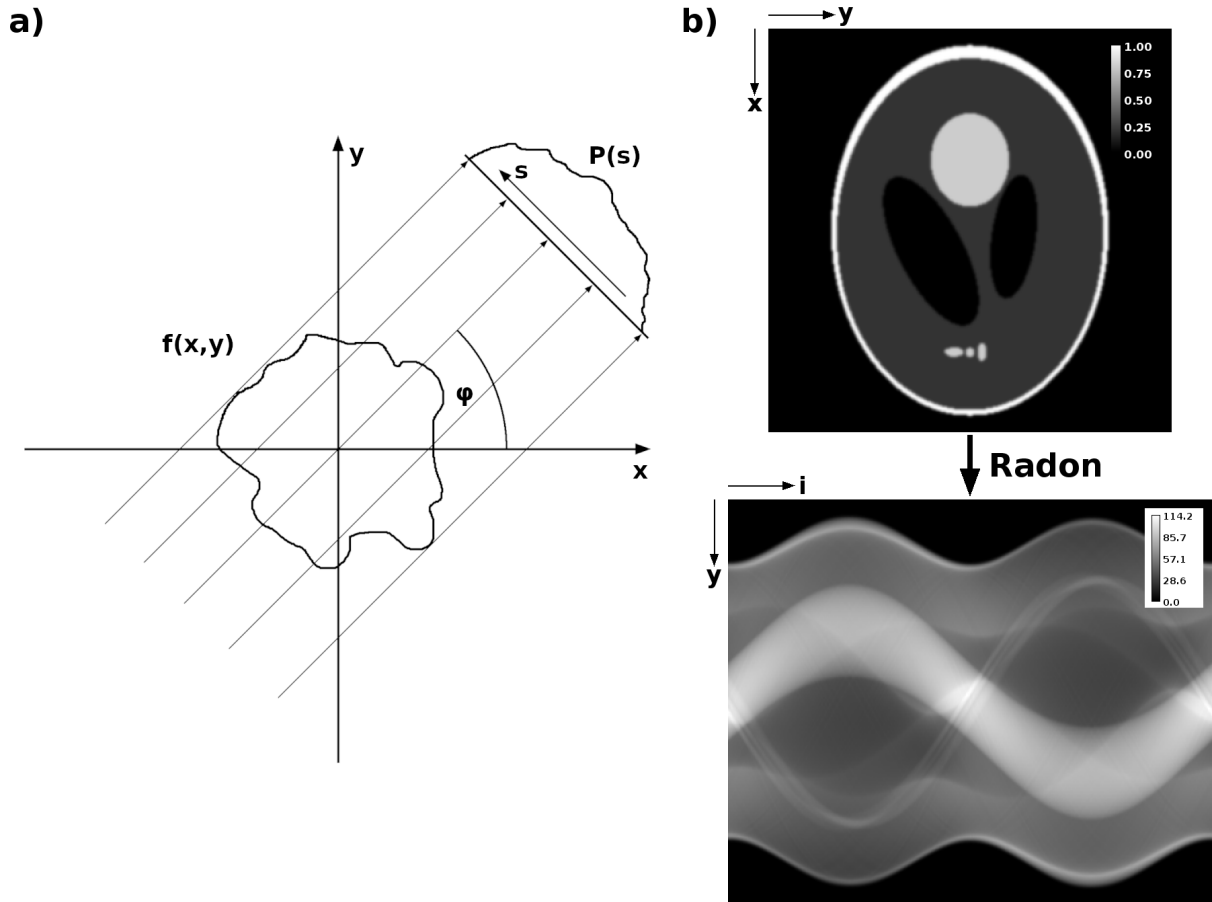


Figure 3.2: a) Projection $P_\varphi(s)$ of the image function $f(x,y)$ along the t -axis rotated against the x -axis by an angle φ as calculated by equation 3.10 (following [KS88]). b) Slice f (top) and corresponding sinogram g (bottom) calculated using algorithm 3.1 and assuming 360 evenly spaced 1° angular steps. The i -coordinate of the sinogram indicates the index of the i -th angular direction φ_i .

new, single image is called the sinogram g :

$$g(s, i) = P_{\varphi_i}(s) \quad (3.12)$$

The pseudo-code algorithm describing a Radon transform in x -direction is shown in algorithm 3.1. Contrary to the Radon transform as given in equation 3.11, here the image function itself, and not the coordinate system, is rotated using bilinear interpolation. As a result, all projections are calculated along the fixed x -axis instead of along the variable t -axis.

Figure 3.2 b) shows a Shepp-Logan phantom as an example slice and the resulting sinogram using algorithm 3.1. The angles chosen for the Radon transform cover the full 360° in 1° steps. It has to be noted that the sinogram in the depicted case shows a symmetry around the y -coordinate of the center of rotation r :

$$g(y - r, i) = g(r - y, i'), \text{ for } \varphi_{i'} = \varphi_i + 180^\circ \quad (3.13)$$

and thus it would be sufficient to only measure up to an angle of 180° without any loss of infor-

Algorithm 3.1: Radon Transform

Data: Slice f , list of angles φ_i

Result: Sinogram g

Assume projection along x -axis;

for all angles φ_i do

 Rotate original slice f by an angle φ_i into f_{φ_i} ;

for all y -coordinates of f_{φ_i} do

 Fill the sinogram with sum along x : $g(y, i) = \sum_x f_{\varphi_i}(x, y)$;

end for

end for

return g

mation. This is usually the case for absorption tomography, but not for emission tomography where the symmetry may be broken by, for example, self-absorption effects.

3.2.2 Inverse Radon Transform

Inverting the Radon transform, or using the data stored inside a sinogram to reconstruct a 2D tomographic slice, is a problem mostly limited by the sparsity of the projection data, caused by the fact that only a finite number of projections can be measured.

Over the years, different methods for tomographic reconstruction have been developed, with many of them being optimized for certain experimental parameters, geometries or measurement modalities. One of the most commonly known methods for tomographic reconstruction is the filtered backprojection algorithm, which is partially based on the backprojection algorithm.

Backprojection

Basic idea of the backprojection (BP) algorithm is to approximate the tomogram by “smearing” the projections over the image space of the slice. Mathematically, this operation can be described using the integral [Bru02]:

$$f_{BP}(x, y) = \int_0^{\pi} g(s, \varphi) d\varphi \quad (3.14)$$

where the upper limit of the integral is being chosen as π and not 2π as a consequence of the symmetry of the sinogram (see eq. 3.13). For discrete cases, the backprojection can be described using the sum:

$$f_{BP}(x, y) = \frac{1}{n_{\varphi}} \sum_i g(s, i) \quad (3.15)$$

with n_{φ} being the number of angles of the sinogram. Similar to as it is the case for the discrete Radon transform, the discrete backprojection requires interpolation for x - and y -coordinates that would correspond to interpixel s -coordinates.

Algorithm 3.2 shows a pseudo-code implementation for the BP algorithm. To be consistent with the Radon transform as described in algorithm 3.1, it is again assumed that the image function, and not the coordinate system, is rotated with the projections being measured along the fixed x -axis.

Algorithm 3.2: Backprojection

Data: Sinogram g , list of angles φ_i
Result: Backprojected slice f_{BP}
 Assume projection along x -axis;
 Initialize zero-value slice: $f_{BP} = 0$ for all x, y ;
for all angles φ_i do
 for all y -coordinates of g do
 Backproject the sinogram onto rotated slice: $f_{\varphi_i}(x, y) = g(y, i)$;
 end for
 Rotate f_{φ_i} by an angle $-\varphi_i$ into f ;
 Add to slice: $f_{BP} \leftarrow f_{BP} + f$;
end for
 Divide by the number of angles: $f_{BP} \leftarrow f_{BP}/n_\varphi$;
return f_{BP}

Depending on the implementation of the BP algorithm, the values of the reconstructed slice may differ. For example, the backprojection can also be implemented as “unfiltered” filtered backprojection (compare eq. 3.18 and 3.19), in which case a constant calibration factor C_{BP} may be included in the algorithm depending on the exact implementation of the filters and (inverse) Fourier transform.

Figure 3.3 a) shows the backprojection of the sinogram from figure 3.2. Comparing the reconstruction with the original slice, it can be seen that the BP reconstruction differs from the ground truth in quality as well as quantity. This is due to the fact that the backprojection does not calculate the inverse of the Radon transform but only an approximation. The “smearing” operation of the backprojection attributes projection data equally to every pixel along the corresponding beam, even if they are not contributing to the projection, which causes the reconstruction to be blurry and its values to differ from the original data. It does, however, reconstruct the general shape of the image function.

Filtered Backprojection

Compared to conventional backprojection, the filtered backprojection (FBP) algorithm is a more commonly used algorithm for tomographic reconstruction as it remedies most of its disadvantages. A detailed derivation of the FBP can be found in [KS88].

Basis of the FBP is the Fourier-Slice-Theorem, which declares that the 1D Fourier transform of a projection of an image function $S_\varphi(w)$ measured under an angle φ is equivalent to a slice through the 2D Fourier transform of the image function $F(u, v)$:

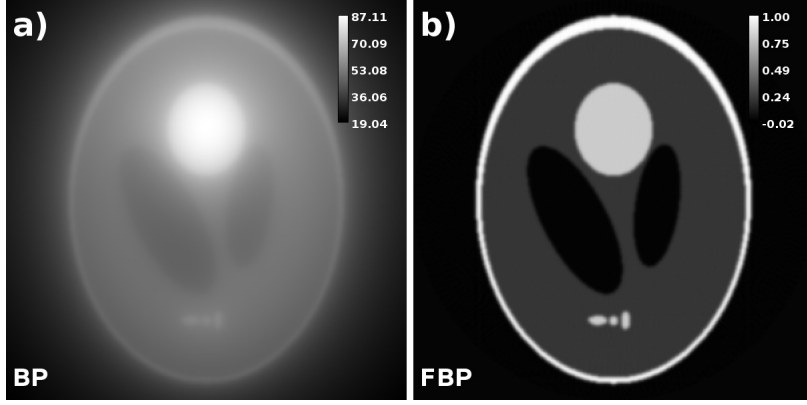


Figure 3.3: Reconstruction of the sinogram depicted in figure 3.2 using a) backprojection and b) filtered backprojection. The filter used for the FBP reconstruction is a Hann-filter.

$$S_{\varphi}(w) = F(w \sin \varphi, -w \cos \varphi) \quad (3.16)$$

Measuring projections and calculating their Fourier transform is therefore equivalent to sampling the 2D Fourier space of the complete image function. Assuming full sampling, $f(x, y)$ can then be calculated using the inverse 2D Fourier transform of $F(u, v)$:

$$f(x, y) = \int_{-\infty}^{\infty} \int_{-\infty}^{\infty} F(u, v) e^{-j2\pi(ux+vy)} du dv \quad (3.17)$$

However, as realistically only a finite amount of projections can be measured in finite time, full sampling of the Fourier space is unachievable. For this reason, it would be necessary to interpolate missing points, which may not be practical in some cases.

Alternatively, instead of interpolating the missing points in Fourier space, it is possible to achieve similar results by applying a ramp-filter $|w|$ to the projections in Fourier space:

$$Q_{\varphi}(s) = \int_{-\infty}^{\infty} S_{\varphi}(w) |w| e^{j2\pi ws} dw \quad (3.18)$$

where $Q_{\varphi}(s)$ is the filtered projection. As the projections sample lines in Fourier space, the sampled points are more dense at the center of the Fourier space and get sparser with increasing distance from it. This effect is counteracted by the ramp-filter by increasing the contribution of points the further they are away from the center of Fourier space. Alternatively, as the ramp-filter especially enhances high frequencies and tends to amplify noise in the data, other filters like the Shepp-Logan-, the cosine- or the Hann-filter may be used.

The filtered projections $Q_{\varphi}(s)$ are then backprojected to ultimately create the reconstruction of the tomogram:

$$f_{FBP}(x, y) = \int_0^{\pi} Q_{\varphi}(s) d\varphi \quad (3.19)$$

Combining both the filter and the backprojection step is called filtered backprojection.

Figure 3.3 b) shows the filtered backprojection of the sinogram from figure 3.2 using the Hann-filter. Compared to the reconstruction by conventional backprojection, the FBP is closer to the original slice and an improvement in both a qualitative as well as quantitative sense.

3.2.3 MLEM Algorithm

Another method to calculate the inverse Radon transform is the MLEM (Maximum-Likelihood Expectation-Maximization) algorithm. MLEM is an iterative algorithm which assumes that the measurements show Poisson probabilistic characteristics. It aims to calculate the inverse Radon transform by finding the reconstruction which is most likely to lead to the measured sinogram [SV82].

Mathematical Derivation

A simplified mathematical derivation of the MLEM algorithm can be found in [Bru02]. If \bar{f}_j is the mean number of events occurring in pixel j and a_{ij} is the probability that an event in pixel j gets detected in a bin i , then the mean number of events \bar{g}_i detected in bin i can be calculated as the sum of the mean number of detected events $a_{ij}\bar{f}_j$ in each pixel j :

$$\bar{g}_i = \sum_{j=1}^m a_{ij}\bar{f}_j \quad (3.20)$$

For probability values $a_{ij} = 1$ if the pixel j is in the path of the probing beam and $a_{ij} = 0$ if it is not, equation 3.20 can be seen as being equivalent to the discrete Radon transform as it is defined in equation 3.11.

As the MLEM algorithm assumes that the number of detected events is a Poisson variable, the probability $P(k)$ of measuring a value k can be modeled by a Poisson distribution:

$$P(k) = \frac{\lambda^k}{k!} e^{-\lambda} \quad (3.21)$$

where λ is the expected value of the measurement. With $k = g_i$ being the number of detected events in bin i and a mean number of detected events $\lambda = \bar{g}_i$ (eq. 3.20), the probability to measure a vector g with a given event map \bar{f} , also called the likelihood-function $L(\bar{f})$, can then be calculated by forming the product of all individual probabilities given in equation 3.21:

$$L(\bar{f}) = P(g|\bar{f}) = \prod_{i=1}^n P(g_i) = \prod_{i=1}^n \frac{\bar{g}_i^{g_i}}{g_i!} e^{-\bar{g}_i} \quad (3.22)$$

To maximize the expectation, usually the logarithm of the likelihood-function $l(f) = \ln(L(f))$ is considered. Applying the natural logarithm to equation 3.22 and using logarithm rules leads to:

$$l(\bar{f}) = \ln(L(\bar{f})) = \sum_{i=1}^n (-\bar{g}_i + g_i \ln(\bar{g}_i) - \ln(g_i!)) \quad (3.23)$$

or, after inserting equation 3.20 into equation 3.23:

$$l(\bar{f}) = \sum_{i=1}^n \left(-\sum_{j=1}^m a_{ij} \bar{f}_j + g_i \ln \left(\sum_{j=1}^m a_{ij} \bar{f}_j \right) - \ln(g_i!) \right) \quad (3.24)$$

The probability to measure g is the highest if $l(\bar{f})$ is maximal. It can be shown that the logarithm of the likelihood-function has only one global maximum [Kau87] and to find this maximum, the derivative of $l(\bar{f})$ has to be calculated:

$$\frac{\partial l(\bar{f})}{\partial \bar{f}_j} = -\sum_{i=1}^n a_{ij} + \sum_{i=1}^n \frac{g_i}{\sum_{j'=1}^m a_{ij'} \bar{f}_{j'}} a_{ij} = 0 \quad (3.25)$$

Multiplying equation 3.25 with \bar{f}_j and rearranging finally leads to:

$$\bar{f}_j = \frac{\bar{f}_j}{\sum_{i=1}^n a_{ij}} \sum_{i=1}^n \frac{g_i}{\sum_{j'=1}^m a_{ij'} \bar{f}_{j'}} a_{ij} \quad (3.26)$$

which is the fundamental iterative equation of the MLEM algorithm:

$$\bar{f}_j^{(k+1)} = \frac{\bar{f}_j^{(k)}}{\sum_{i=1}^n a_{ij}} \sum_{i=1}^n \frac{g_i}{\sum_{j'=1}^m a_{ij'} \bar{f}_{j'}^{(k)}} a_{ij} \quad (3.27)$$

where k indicates the k -th iteration.

A pseudo-code implementation of the MLEM algorithm for tomographic reconstruction is shown in algorithm 3.3. Essentially, this algorithm compares the sinogram of the current guess of the reconstruction to the measured sinogram and uses a normalized backprojection of this comparison to update the reconstruction.

Logically, the way the MLEM algorithm reconstructs tomograms can be understood by focusing on the backprojection of the sinogram ratio. Assuming the ideal case of the simulated sinogram being identical to the measured sinogram, then their ratio will have a value of one in every pixel. Backprojecting a sinogram which consists of one-values will result in a slice with one-values inside the reconstructed sample area. Thus, there will be no change during the multiplicative update. If the simulated sinogram has lower values than the measured sinogram, their ratio and its backprojection will consist of values greater than one. This will lead to an increase during the update and in that way to an increase of values in the simulated sinogram, bringing the simulated closer to the measured data. The inverse applies if the simulated sinogram has higher values than the measured sinogram.

Algorithm 3.3: Tomographic MLEM

Data: Measured sinogram g , number of iterations n_k

Result: Reconstructed slice f

Initialize the slice with a first guess, e.g. with a backprojection: $f^{(0)} = BP(g)$;

$k = 0$;

while $k < n_k$ **do**

 Radon transform to simulate a sinogram: $g_{sim} = R(f^{(k)})$;

 Divide measured and simulated sinograms: $r_g = g \oslash g_{sim}$;

 Backproject into a slice: $f_{ratio} = BP(r_g)$;

if calibration in backprojection $C_{BP} \neq 1$ **then**

 | Normalize to BP-calibration: $f_{ratio} \leftarrow f_{ratio}/C_{BP}$;

end if

 Update by multiplication: $f^{(k+1)} = f^{(k)} \odot f_{ratio}$;

$k \leftarrow k + 1$;

end while

return $f = f^{(n_k)}$

Advantages and Disadvantages

Main advantages of MLEM in comparison to FBP are the improved signal-to-noise ratio, especially in empty regions outside of the reconstructed sample, as well as the reduction of artifacts caused by insufficient angular sampling. In addition, assuming positive data, which is usually the case for emission tomography like XRF tomography, the multiplicative *ansatz* of MLEM ensures non-negativity of the reconstructed results. This is not the case for FBP, where nonphysical negative values are not explicitly excluded and often occur as part of the noise or around reconstruction artifacts. Also, the iterative nature of the MLEM algorithm allows the change of the tomographic model between iterations without restarting the entire reconstruction process, which is of importance in cases in which the tomographic model is not only dependent on the sinogram and reconstructed slice but also on other external parameters (e.g. the absorption of X-rays inside the sample).

The most apparent disadvantage of the MLEM algorithm is the fact that it is an iterative algorithm and reconstructions thus require an amount of time approximately linear to the amount of iterations to complete. Compared to one-step algorithms, like for example FBP, these reconstructions are slower and, depending on the required number of iterations, can be very time-consuming. For this reason, advanced computational hardware and efficient implementation of the algorithm are a necessity. Another common disadvantage of MLEM in specific, and of many iterative tomographic reconstruction algorithms in general, is the amplification of noise in the reconstruction for high numbers of iterations, which makes it difficult to define exit conditions for the iterative process. These effects, however, can be mitigated by reducing the number of iterations as well as by using filters or Bayesian penalizing priors between the iterations. Furthermore, some artifacts caused by inconsistencies in the tomographic model, like for example signal outside of the reconstructed field-of-view, tend to become worse with advancing recon-

struction, which makes the use of MLEM unsuitable for special tomographic cases like limited field-of-view tomography.

Figure 3.4 shows reconstructions of the sinogram displayed in figure 3.2 b) using FBP, 100 iterations and 300 iterations of MLEM as well as a line plot through all three reconstructions and through the ground truth. Poisson noise assuming a maximum value of 10000 counts was applied to the sinogram before reconstruction to simulate a measurement process. It can be seen that the FBP reconstruction, in contrast to the MLEM reconstructions, shows negative values and increased noise in areas without sample. For areas with sample, the noise of the FBP reconstruction and the 100 iteration MLEM reconstruction are on a similar level, with the MLEM reconstruction having a slightly worse resolution as evident from the transition from sample to the empty area inside the sample. The 300 iteration MLEM reconstruction has a similar resolution than the FBP reconstruction, but a higher noise level than the FBP as well as the 100 iteration MLEM reconstruction. It has to be noted that both MLEM reconstructions exhibit an artifact which presents itself as increased intensity inside the inner-sample empty area.

Reconstruction of Non-Poisson Data

The MLEM algorithm is derived assuming that the measured data exhibits a Poisson characteristic, which is the case for XRF and uncorrected transmission data. However, the reconstruction of absorption tomograms requires calculating the logarithm of the normalized transmission and thus skews the Poisson characteristic of the data.

While there are MLEM algorithms especially adapted to account for the specifics of absorption tomography, they are mathematically more complex, rely on assumptions and lack exact analytical solutions [LC84]. For those reasons, using the conventional MLEM algorithm is usually preferred, even if the statistic of the tomographic data does not follow an ideal Poisson distribution. This may lead to worse convergence and noise reduction during the reconstruction. However, the basic idea of MLEM of updating the reconstruction by comparing the measured and a simulated sinogram does not change and especially for high count rate data with good signal-to-noise ratio the negative influences caused by the deviation from the ideal model should be negligible.

In fact, if the aim of an experiment is to compare XRF and absorption tomograms, the variations caused by reconstructing the absorption tomogram using a different algorithm with different reconstruction characteristics may exceed the inaccuracies in the MLEM algorithm introduced by the non-Poisson characteristics of the absorption data.

OSL-MLEM

There are multiple methods to mitigate the effect of higher noise for many iterations of the MLEM algorithm. One method would be to apply filters, for example a smoothing filter, between the iterations. Another method would be the utilization of *a priori* information of the sam-

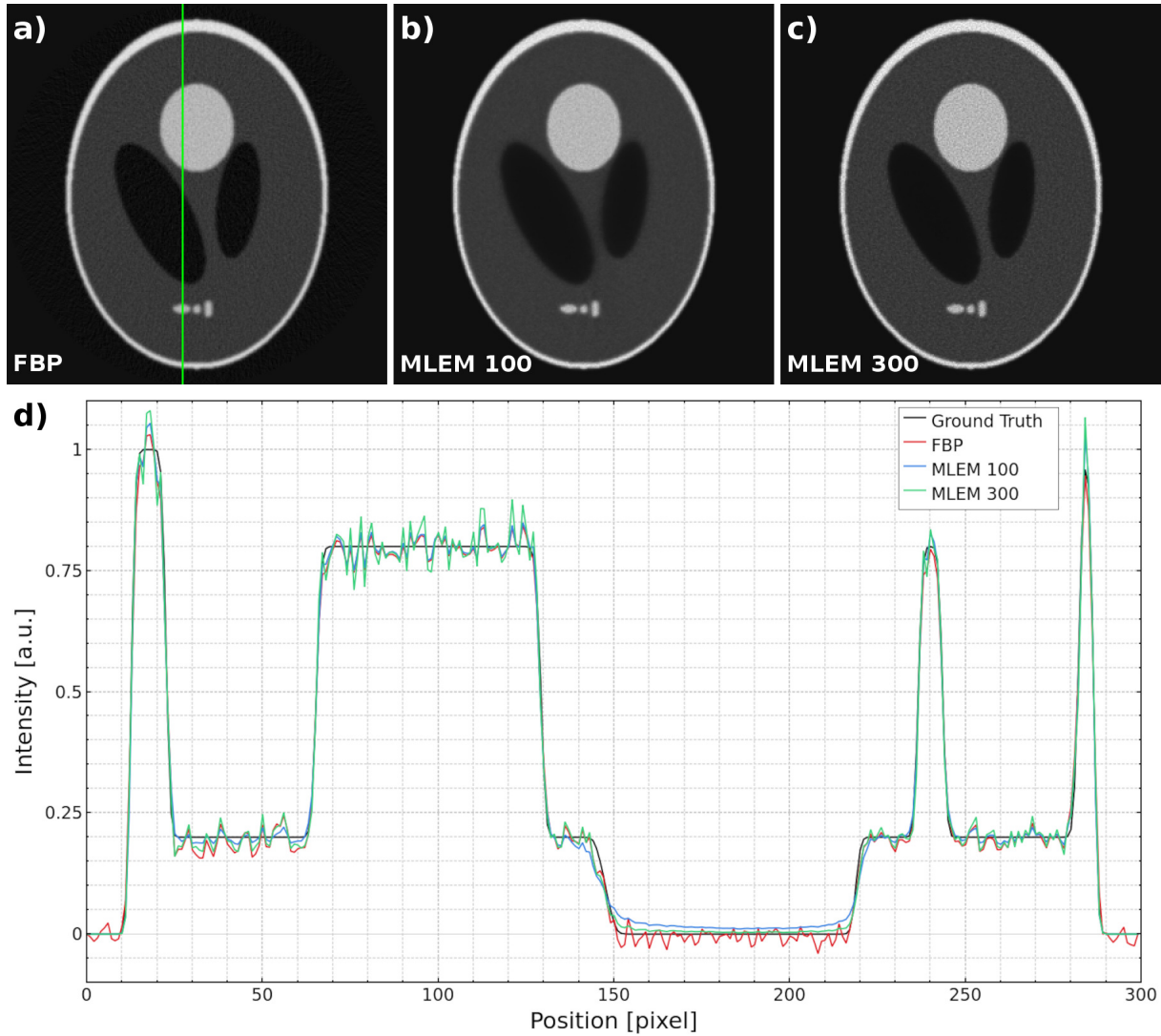


Figure 3.4: Tomographic reconstruction of the phantom using a) FBP with a Hann-filter, b) MLEM with 100 iterations and c) MLEM with 300 iteration. Poisson noise was applied to the sinogram assuming a maximum value of 10000 counts. The vertical green line in a) marks the position of the line profiles plotted in d).

ple by introducing a Bayesian prior, a weighted penalty term, into the reconstruction [ARA97]. Often, the prior is chosen in such a way that it penalizes local roughness and thus reduces the noise in the reconstruction.

A short mathematical derivation of this penalized MLEM algorithm using a Gibbs prior is presented in [Bru02]. Compared to equation 3.27, the final penalized MLEM algorithm introduces an additional term to the normalization part of the equation:

$$\bar{f}_j^{(k+1)} = \frac{\bar{f}_j^{(k)}}{\sum_{i=1}^n a_{ij} + \beta' \frac{\partial}{\partial \bar{f}_j} U(\bar{f}_j^{(k)})} \sum_{i=1}^n \frac{g_i}{\sum_{j'=1}^m a_{ij'} \bar{f}_{j'}^{(k)}} a_{ij} \quad (3.28)$$

where β' is the weight of the prior and U is an energy function of \bar{f} . Rearranging leads to:

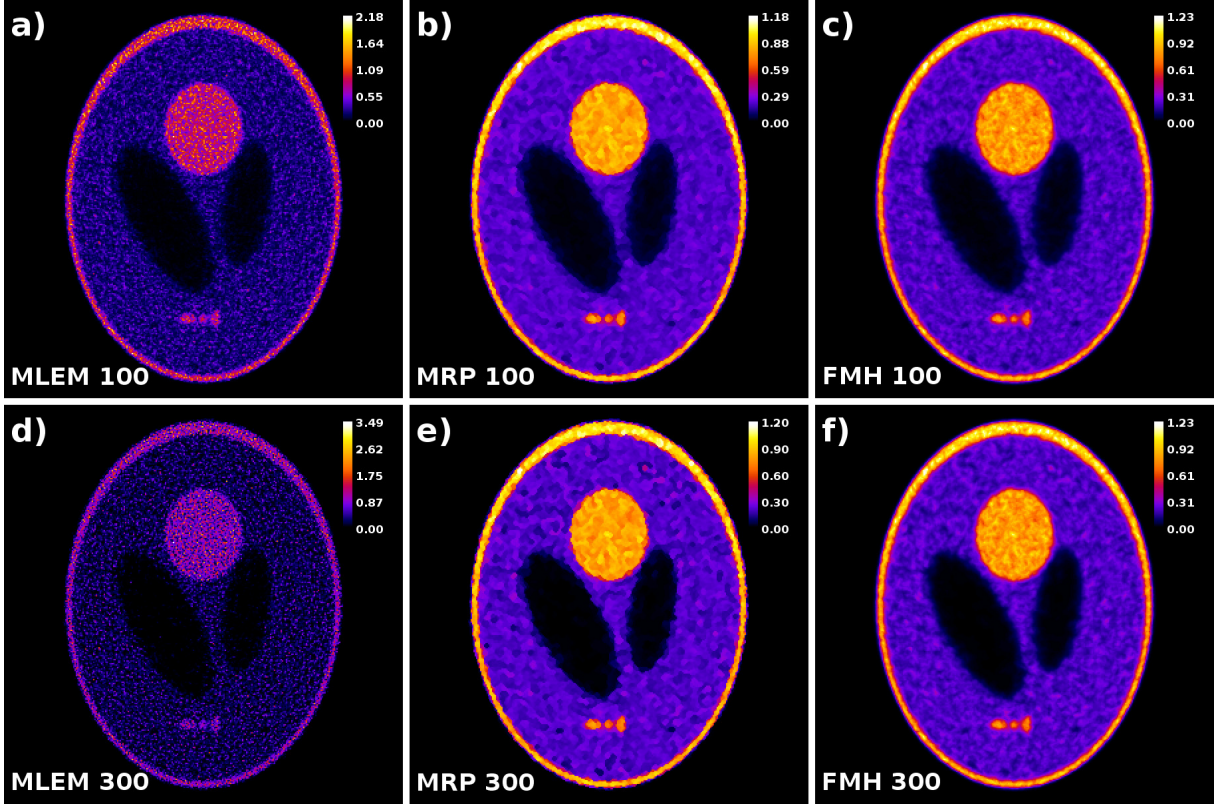


Figure 3.5: Tomographic reconstructions of the phantom using a) 100 iterations of MLEM, b) 100 iterations of MLEM-MRP, c) 100 iterations of MLEM-FMH, d) 300 iterations of MLEM, e) 300 iterations of MLEM-MRP and f) 300 iterations of MLEM-FMH. Poisson noise assuming a maximum value of 100 counts was applied to the sinogram before reconstruction and a weight of $\beta = 0.3$ was used for the OSL methods. All images are scaled to their respective maxima.

$$\bar{f}_j^{(k+1)} = \frac{\bar{f}_j^{MLEM(k+1)}}{1 + \beta \frac{\partial}{\partial f_j} U(\bar{f}_j^{(k)})} \quad (3.29)$$

$$\beta = \frac{\beta'}{\sum_{i=1}^n a_{ij}} \quad (3.30)$$

with $\bar{f}_j^{MLEM(k+1)}$ being the result of an iteration of the conventional MLEM algorithm and β being the modified weight of the prior. From equation 3.29 it becomes clear that for the penalized MLEM the result of the $(k+1)$ -th iteration gets modified by a term depending on the result of the k -th iteration. For this reason, these algorithms are also called one step late (OSL) algorithms.

A possible prior is the median-root-prior (MRP), which favors locally monotonous structures and penalizes isolated noise spikes [AR97]:

$$\left(\frac{\partial}{\partial f_j} U(\bar{f}_j^{(k)}) \right)_{MRP} = \frac{\bar{f}_j^{(k)} - med(\bar{f}_j^{(k)})}{med(\bar{f}_j^{(k)})} \quad (3.31)$$

where $med(\bar{f}_j^{(k)})$ is the median of all values of $\bar{f}_j^{(k)}$ that are located in a 3×3 area around pixel j .

Figure 3.5 b) and e) show the MRP reconstruction of a noisy version of the sinogram from figure 3.2 after 100 and 300 iterations, respectively. The Poisson noise was applied assuming a maximum value of the sinogram of 100 counts and the modified weight of the prior was set to $\beta = 0.3$. Compared to the reconstructions using conventional MLEM, shown in figure 3.5 a) and d), the noise levels of the MRP reconstructions are lower and the quantitative values closer to the ground truth. Furthermore, in contrast to for example smoothing filters, MRP preserves the edges inside the reconstruction. However, it can also be seen that the MRP algorithm creates artificially sharp edges and plateau-like structures. This is caused by the fact that MRP assumes monotonic, locally homogeneous sample regions and thus handles and penalizes small, non-monotonic details like noise.

An alternative to MRP is the finite-impulse-response median hybrid (FMH), which uses the median of multiple directional weighted averages instead of median of all values inside a certain region [AR02]:

$$\left(\frac{\partial}{\partial f_j} U(\bar{f}_j^{(k)}) \right)_{FMH} = \frac{\bar{f}_j^{(k)} - fmh(\bar{f}_j^{(k)})}{fmh(\bar{f}_j^{(k)})} \quad (3.32)$$

where $fmh(\bar{f}_j^{(k)})$ is the FIR median of the area around pixel j . An example implementation of a 3×3 FIR median is described in [AR02] and uses five directional weighted averages: The central value (weight: 4), the horizontal or vertical nearest neighbors (weight: $\sqrt{2}$) and the central value as well as the second neighbors (weight: 1) and the central value for both diagonals.

As can be seen from figure 3.5 c) and f), which shows the FMH reconstruction of the already described sinogram using 100 and 300 iterations, respectively, the FMH reconstruction maintains the quantitative accuracy and noise suppression of MRP without the artificial edges and plateau-like structures. However, the downside of FMH is a weaker edge preservation and thus increased blurring of the reconstruction.

Table 3.1 shows the normalized mean absolute error of the reconstruction for different implementations of the MLEM algorithm and different strength of Poisson noise calculated against the noiseless ground truth. The normalized mean absolute error (NMAE) of two positive datasets x and y is defined as:

$$NMAE(x, y) = \frac{\sum_i |x_i - y_i|}{\sum_i y_i} \quad (3.33)$$

Comparing the values given in table 3.1, it can be seen that the error of the reconstructions for conventional MLEM increases with the amount of iterations and the strength of the Poisson noise. This effect is reduced for OSL-MLEM reconstructions in such a way that the error even decreases with higher iterations for some versions of the FMH reconstructions. In those cases, the reconstructions are advanced with less noise but at the cost of smaller details and resolution. Thus, OSL-MLEM, and especially FMH, may be used during the earlier iterations of the algorithm to let the reconstruction develop with less noise influence and then turned off

Table 3.1: Normalized mean absolute errors (eq. 3.33) of reconstructions calculated against the noiseless ground truth for different amounts of iterations and strengths of Poisson noise.

NMAE(recon., truth)	Poisson 10000	Poisson 1000	Poisson 100	Poisson 10
MLEM 100	0.0536	0.1139	0.3146	0.8543
MLEM 300	0.0665	0.1955	0.5629	1.2194
MRP 100	0.0405	0.0622	0.1270	0.2988
MRP 300	0.0288	0.0610	0.1405	0.3412
FMH 100	0.0720	0.0843	0.1354	0.3222
FMH 300	0.0637	0.0773	0.1329	0.3305

during the later iterations to allow for higher resolution.

Chapter 4

X-Ray Fluorescence Self-Absorption Correction

4.1 XRF Self-Absorption

The accurate description and correction of X-ray fluorescence self-absorption effects is important to obtain qualitative as well as quantitative results from XRF measurements.

4.1.1 Self-Absorption Effects

Figure 4.1 shows the basic setup of an XRF tomography experiment. While propagating through the sample, the focused primary beam is absorbed and excites the isotropic emission of XRF signal, which is then measured by a spectrally resolved XRF detector. Behind the sample, another detector measures the total amount of transmitted beam. During the experiment, the sample is translated and rotated to allow for the measurement of spatially resolved data.

Depending on the size and the elemental composition of a sample, tomographic measurements may suffer from self-absorption effects. These effects are often negligible for very small samples with sizes in the low or submicron range and for elements with high energy XRF emission lines inside low-Z, low absorption sample matrices. However, as the flux of X-ray sources and the speed of sample stages and X-ray detectors increases, scanning tomography measurements become more time efficient. This allows for the scanning of bigger samples without additional expenditure of time, in which case the correct description and correction of self-absorption effects becomes increasingly important.

There are two main effects that have to be considered for the description of the self-absorption problem: The absorption of the primary beam in the sample before it excites the emission of XRF signal and the absorption of the emitted XRF signal in the sample before it is detected by the XRF detector.

The primary beam absorption volume is accessible by reconstructing the absorption tomogram at the primary beam energy using the transmission data measured behind the sample. With this data, the fraction of the primary beam reaching each voxel of the tomographic volume can be

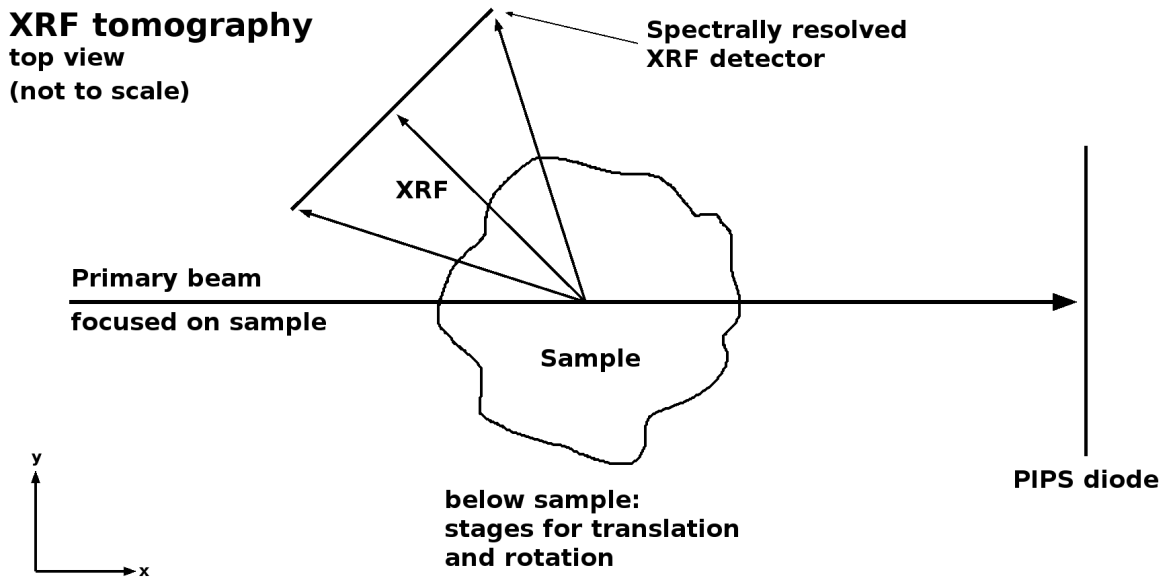


Figure 4.1: Schematic overview of the measurement geometry of an XRF tomography experiment. The primary X-ray beam is absorbed inside the sample and excites the emission of XRF signal. Transmission of the primary beam and spectrum of the XRF signal are measured by a PIPS diode behind the sample and an XRF detector, respectively.

easily determined by calculating the sum of the optical depths from the edge of the volume to the voxel and inserting this sum into the Beer-Lambert law (eq. 2.7).

Contrarily, the absorption of the XRF signal inside the sample is not as easily accessible. This has two main reasons: On one hand, the XRF signal is emitted isotropically, meaning the transmission of the XRF signal has to be calculated along all paths to the detector for all voxel of the volume. Depending on the chosen reconstruction parameters, this operation can be very computationally expensive. On the other hand, and more important, the absorption volumes at the XRF line energies are usually unknown as they are often not measured separately for time reasons. It is therefore necessary to find alternative methods to calculate these volumes.

Apart from the absorption of the primary beam and the absorption of the main XRF signal, additional self-absorption effects, like for example higher order XRF, do exist. However, as their calculation tend to be very computationally expensive in relation to their influence on the self-absorption problem, they are usually omitted in self-absorption correction algorithms.

4.1.2 State of the Science

Over the years, the importance of correcting XRF tomograms for self-absorption effects to obtain qualitatively and quantitatively accurate results led to the development of many different algorithms.

For example, in 2001 Schroer [Sch01] developed a self-absorption correction algorithm using the conjugate gradient method to optimize a non-linear least-squares problem to sequentially calculate the attenuation coefficients of elements and thus their mass density distributions. However, Schroer's algorithm uses a scaling law to calculate the energy dependence of absorption

coefficients, which only holds true far from any absorption edges. If the absorption edge of another element is present between the absorption edge and the fluorescence energy of an element, both of these elements need to be reconstructed simultaneously [SBG⁺02]. Furthermore, although in principle extendable into 3D, the algorithm was only demonstrated in 2D. This limitation is shared by most studies on self-absorption correction algorithms and is most likely caused by a lack of computational resources.

In 2006 La Rivière *et al.* [RBV⁺06] used an iterative penalized-likelihood algorithm to correct for self-absorption effects and also an extended scaling law to include empirically fitted analytic expressions for the energy dependence of the X-ray attenuation coefficients (see eq. 2.11). As their algorithm explicitly models the Poisson counting statistics of the XRF detection process, it produces fitting results even in the low-count regime. However, they assumed the absence of additional absorption edges between the absorption edge and the emission line of an element, with the suggestion that this problem may be solved by reconstructing elements simultaneously. Another difficulty is the need to determine appropriate smoothing parameters for the penalized-likelihood algorithm.

Yang *et al.* [YDD⁺14] proposed an algorithm based on AC-OSEM, a variation of MLEM, in 2014. Their algorithm further extends the scaling law to calculate fluorescence attenuation maps, but assumes a trace-element approximation with low elemental concentrations and a known low-Z background. Thus their algorithm is mostly suited for biological and biomedical samples.

A refined scaling law for L-shell XRF was proposed in 2015 by Long *et al.* [LYQ⁺15]. Using an algorithm based on MLEM, their focus was the reconstruction and absorption-correction of high-Z elemental data.

In 2017 Di *et al.* [DCH⁺17] extended the idea of self-absorption correction by including the joint reconstruction of XRF and absorption data by alternatively maximizing a Poisson likelihood objective. Their algorithm also uses tabulated values to calculate the XRF absorption instead of a scaling law.

Later the same year, Huang *et al.* [HLR17] proposed an iterative absorption correction algorithm utilizing the asymmetry of the measured self-absorption sinograms. However, this approach is only viable if there is visible asymmetry in the sinograms, which may not be the case for all measurement geometries, for example for XRF data measured with an XRF detector in backscattering geometry. Furthermore, as Yang *et al.*, they assumed a trace-element approximation.

A year later, in 2018, Vigano *et al.* [VS18] established a more general description of the forward model and reconstruction algorithm. However, they did not deal with the problem of the unknown XRF absorption.

Recently, in 2020, Gao *et al.* [GLD⁺20] improved the forward model by introducing experimental parameters and sped up the algorithm by implementing it on a GPU. In contrast to the algorithms described before, this allows them to correct for self-absorption in full 3D instead of relying on approximations that only consider 2D geometries.

4.2 Self-Absorption Correction Algorithm

Compared to the algorithms mentioned above, this MLEM-based algorithm tries to improve the self-absorption corrected reconstruction of XRF tomographic datasets in multiple ways. For one, the algorithm is fully calculated in 3D, taking into account both the sample and XRF detector geometry. Additionally, it does not use scaling laws to calculate the energy dependent absorption of measured elements, but uses tabulated values. A scaling law is only used to describe the energy dependency of the background consisting of unmeasured elements and only if its composition cannot be approximated sufficiently. This is done to be able to correctly describe cases where the absorption edge of one element lies between the absorption edge and fluorescence line of another. As a consequence, however, the elements cannot be reconstructed sequentially, but have to be reconstructed simultaneously, which increases the number of parameters for the algorithm and may complicate the reconstruction.

Corrections for higher order effects are not included in the algorithm for computational reasons but the scattering of X-rays inside the sample is approximated by using the angle-independent total attenuation cross section σ_{att} instead of the photoabsorption cross section σ_{abs} to calculate absorption from density data. Furthermore, the algorithm assumes that the amount of emitted XRF for a constant incident X-ray flux scales linear with elemental densities inside a voxel, thus ignoring any subvoxel or nonlinear absorption effects.

The algorithm itself consists of four main parts: The initial calculations at the beginning of the reconstruction, which are only performed once, the self-absorption Radon transform, which defines the self-absorption model, the self-absorption MLEM algorithm, which deals with the qualitative aspects of the reconstructions by ensuring their consistency to the measured sinograms, and the consistency refinement loop, which deals with the quantitative aspects of the reconstructions including the data calibration and ensuring their consistency to the measured absorption tomogram. A schematic overview of the algorithm is given in figure 4.2.

4.2.1 Initial Calculations

The initial calculations are performed once at the beginning of the algorithm and include steps like the processing of the primary energy absorption volume, the calculation of detector directions, initial reconstruction of the elemental tomograms and, if necessary, the calculation of background factors.

Absorption Volume

The measured absorption tomogram τ_0^{meas} at primary beam energy E_0 is reconstructed separately from the self-absorption correction algorithm. While the method of reconstruction may vary, it should have similar resolution and artifact characteristics as MLEM to make it easier to compare the XRF and absorption tomography datasets.

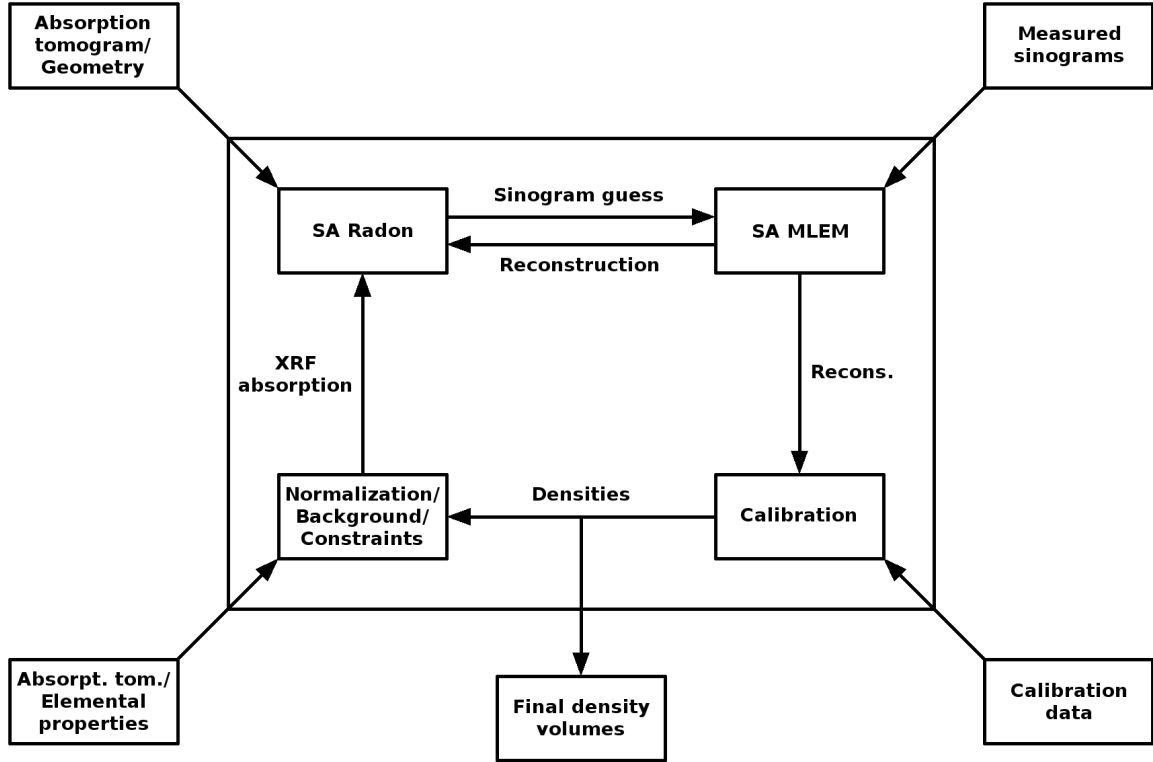


Figure 4.2: Schematic overview of the tomographic self-absorption correction algorithm.

After the absorption tomogram is loaded by the algorithm, its minimum value is set to zero to assure non-negativity. This is done by cutting off all negative values and setting them to zero. If *a priori* knowledge about the shape of the sample is available, it may be possible to define a support for the absorption volume and separate non-empty from empty regions. Thus, the overall influence of noise and/or reconstruction artifacts inside empty regions on the algorithm could be reduced. The most simple method of defining a support is using an attenuation threshold T_{att} below which the values of the absorption volume are set to zero:

$$\tau_0^{meas} \leftarrow \begin{cases} \tau_0^{meas}, & \tau_0^{meas} \geq T_{att} \\ 0, & \tau_0^{meas} < T_{att} \end{cases} \quad (4.1)$$

It is important to note that the support is only applied to the absorption volume, and not the elemental volumes, to prevent accidentally setting trace elements not visible in the absorption volume to zero.

The initial XRF absorption volumes $\tau_L^{(0)}$ at energies E_L for all reconstructed lines L are set to τ_0^{meas} . As the absorption generally increases with decreasing energy, this usually underestimates the absorption of the XRF signal. However, this is preferable to overestimating the XRF absorption, which could lead to artifacts in the reconstruction.

Initial Reconstructions

The initial values of the elemental reconstruction $f_L^{(0)}$ for XRF emission line L is determined by calculating the backprojections of the corresponding measured sinograms g_L^{meas} :

$$f_L^{(0)} = BP(g_L^{meas}) \quad (4.2)$$

To assure non-negativity of the reconstructed data, all negative values in the measured sinograms, should they exist, are set to zero beforehand.

As the backprojections of the measured sinograms may not be ideal initial values, there is also an optional possibility to apply some iterations of conventional MLEM to the initial reconstructions. Depending on the exact nature of the measured sinograms and the chosen reconstruction parameters, this may speed-up the convergence of the algorithm and reduce artifacts.

Detector Directions

Basis for the calculation of the detector directions is a 2D detector matrix, which is loaded as binary image-file. It is assumed that the detector image x -axis is parallel to the sample z -axis and the detector image y -axis parallel to the sample xy -plane, with sample axes as defined in figure 4.1. Furthermore, it is assumed that the normal passing through the center of the detector image intersects the primary beam at the x -center of the sample volume, which is constant as the sample is scanned only in y - and z -direction. Thus, the detector is placed on a circle in the plane of the primary beam with the sample-detector distance $s_{det} > 0$ as radius and an angle δ_{det} from the x -axis (fig. 4.3).

Assuming the distance from the center of the detector $(c_{det,x}, c_{det,y})$ to a detector pixel j is defined by a vector \vec{w}_j in the detector image plane:

$$\vec{w}_j = \begin{bmatrix} w_{j,x} \\ w_{j,y} \end{bmatrix} = \begin{bmatrix} d_{det}(x_{det,j} - c_{det,x}) \\ d_{det}(y_{det,j} - c_{det,y}) \end{bmatrix} \quad (4.3)$$

where $x_{det,j}$ and $y_{det,j}$ are the pixel coordinates of detector element j and d_{det} is pixel size of the detector image.

Then the distance s_j between the x -center of sample volume and the y -component of detector pixel \vec{w}_j can be calculated as:

$$s_j = \sqrt{w_{j,y}^2 + s_{det}^2} \quad (4.4)$$

The angle α_j between s_{det} and s_j is defined as:

$$\alpha_j = \angle DCE_j = \arctan\left(\frac{w_{j,y}}{s_{det}}\right) \quad (4.5)$$

where point D is the center of the detector and point C the x -center of the sample volume. Point E_j is defined by the detector x -center and the y -component of detector pixel \vec{w}_j .

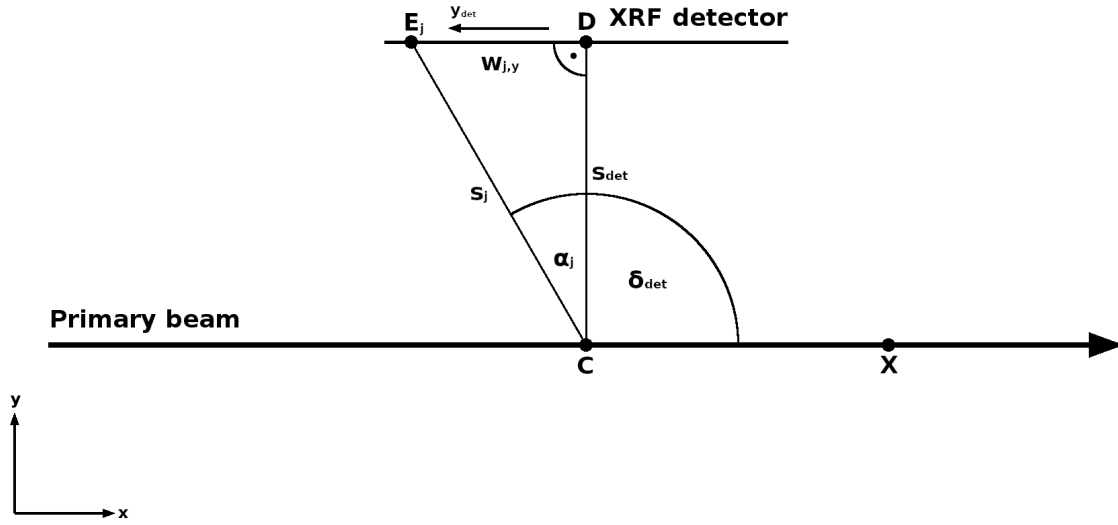


Figure 4.3: Example geometry for the calculation of the detector direction towards a single detector element using an XRF detector placed at an angle of $\delta_{det} = 90^\circ$.

The angle β_j can then be calculated as the sum of detector angle δ_{det} and angle α_j :

$$\beta_j = \angle XCE_j = \delta_{det} + \alpha_j \quad (4.6)$$

where X is an arbitrary point with identical y - and z -coordinates but a higher x -coordinate than point C .

From the above calculations it then follows that the non-normalized detector directions \vec{p}_j are defined as:

$$\vec{p}_j = \begin{bmatrix} p_{j,x} \\ p_{j,y} \\ p_{j,z} \end{bmatrix} = \begin{bmatrix} s_j \cdot \cos(\beta_j) \\ s_j \cdot \sin(\beta_j) \\ w_{j,x} \end{bmatrix} \quad (4.7)$$

As these directions are neither normalized nor account for any deviation of the voxel position from the x -center of the sample volume, they have to be further adapted during the self-absorption Radon transform.

Background Factors

If elements with absorption edges above the primary beam energy E_0 or below the energy of the lowest measured XRF line are present, a background consisting of the absorption of all those unmeasured elements has to be included into the algorithm and its energy dependent scaling factors have to be calculated. One common example would be the low- Z element background in biological samples. If the composition of the background is known or approximation is possible, the energy dependent background scaling factors B_L can be calculated as the ratio of

the attenuation cross sections $\sigma_{att,BG}$ of the background material at the XRF line energy E_L and at the primary beam energy E_0 :

$$B_L = \frac{\sigma_{att,BG}(E_L)}{\sigma_{att,BG}(E_0)} \quad (4.8)$$

Alternatively, as the elements making up the background per definition have no absorption edges inside the for the absorption correction relevant energy range, the energy dependence of the background can also be calculated using the scaling law defined in equation 2.11:

$$B_L = \left(\frac{E_L}{E_0} \right)^\gamma \quad (4.9)$$

with the empirical scaling parameter γ , which usually has a value of $-3 \leq \gamma \leq -2.7$.

Utilizing the background scaling factor B_L , the background absorption volume at an XRF line energy $\tau_{BG,L}$ can then be calculated from the background absorption volume at the primary beam energy $\tau_{BG,0}$:

$$\tau_{BG,L} = B_L \cdot \tau_{BG,0} \quad (4.10)$$

4.2.2 Self-Absorption Radon Transform

The self-absorption Radon transform calculates self-absorption sinograms for a given volume and self-absorption model. In the current implementation it consists of three steps: The calculation of the primary beam transmission volumes at every angle, the calculation of the XRF radiation transmission volumes at every angle and, using the results of the first two steps, the calculation of the self-absorption sinogram.

Primary Beam Transmission

In the first step of the primary beam transmission calculation, the optical depth absorption volume τ_0^{meas} at primary energy E_0 is rotated around the z -axis by an angle φ_i into $\tau_{0,\varphi_i}^{meas}$. Assuming that the x -axis is the primary beam direction, the following step is the calculation of the sum of optical depths s_{0,φ_i} along the x -axis starting from the edge of the rotated absorption volume ($x = 0$) to every voxel:

$$s_{0,\varphi_i}(x, y, z) = \sum_{x'=0}^x \tau_{0,\varphi_i}^{meas}(x', y, z) \quad (4.11)$$

After that, the Beer-Lambert law (eq. 2.7) can be used to calculate the primary beam transmission volume t_{0,φ_i} for angle φ_i :

$$t_{0,\varphi_i}(x, y, z) = e^{-s_{0,\varphi_i}(x, y, z)} \quad (4.12)$$

A pseudo-code implementation of the primary beam transmission calculation is shown in algo-

rithm 4.1. Equation 4.11 can easily be implemented as cumulative sum to reduce the amount of necessary computational steps.

Algorithm 4.1: Primary Beam Transmission

Data: Rotated primary beam absorption volume $\tau_{0,\varphi_i}^{meas}$

Result: Primary beam transmission volume t_{0,φ_i}

Calculation at an angle φ_i ;

Define x -axis as primary beam direction and $\tau = \tau_{0,\varphi_i}^{meas}$;

for all voxel $\vec{v} = (0, v_y \in \mathbb{N}_0, v_z \in \mathbb{N}_0)$ in volume τ **do**

 Define start position: $\vec{u} = \vec{v}$;

 Initialize cumulative absorption sum: $s_0 = 0$;

while position \vec{u} exists in volume τ **do**

 Increase cumulative absorption sum: $s_0 \leftarrow s_0 + (\tau)_{\vec{u}}$;

 Calculate transmission to current position: $(t)_{\vec{u}} = e^{-s_0}$;

 Advance x -component of position: $u_x \leftarrow u_x + 1$;

end while

end for

return $t_{0,\varphi_i} \leftarrow t$

A simulated example slice of a primary beam transmission volume is shown in figure 4.4 b). The corresponding elemental slice is shown in figure 4.4 a) and is itself part of a 3D Fe-phantom (see fig. 4.8 a). It can be seen that the fraction of the primary beam reaching each voxel decreases along the x -axis as the primary beam is absorbed by the sample.

As the primary beam transmission volumes only depend on the measured absorption volume, they, in theory, have to be calculated just once at the beginning of the self-absorption correction algorithm. However, storing a full volume for every angle of the tomogram may cause memory issues during real-world applications and necessitate different solutions.

XRF Radiation Transmission

The XRF transmission volume $t_{L,\varphi_i}^{(k)}$ at iteration k for an XRF line L under an angle φ_i is calculated by determining the average transmission at energy E_L along all detector directions for every voxel $\vec{v} = (x, y, z)$ of the rotated XRF absorption volume. For the following description, it is assumed that the optical depth absorption volume $\tau_L^{(k)}$ at the XRF line energy and subsequently its rotated versions $\tau_{L,\varphi_i}^{(k)}$ are known.

As the original detector directions p_j are calculated from the x -center c_x of the sample volume, they first have to be modified to account for the location of the considered voxel. To this end, the x -components of the detector directions $p_{j,x}$ are modified using the x -component of the voxel position v_x in relation to the x -center of the sample volume:

$$\vec{p}_j^{\vec{v}} = \begin{bmatrix} p_{j,x} - d(v_x - c_x) \\ p_{j,y} \\ p_{j,z} \end{bmatrix} \quad (4.13)$$

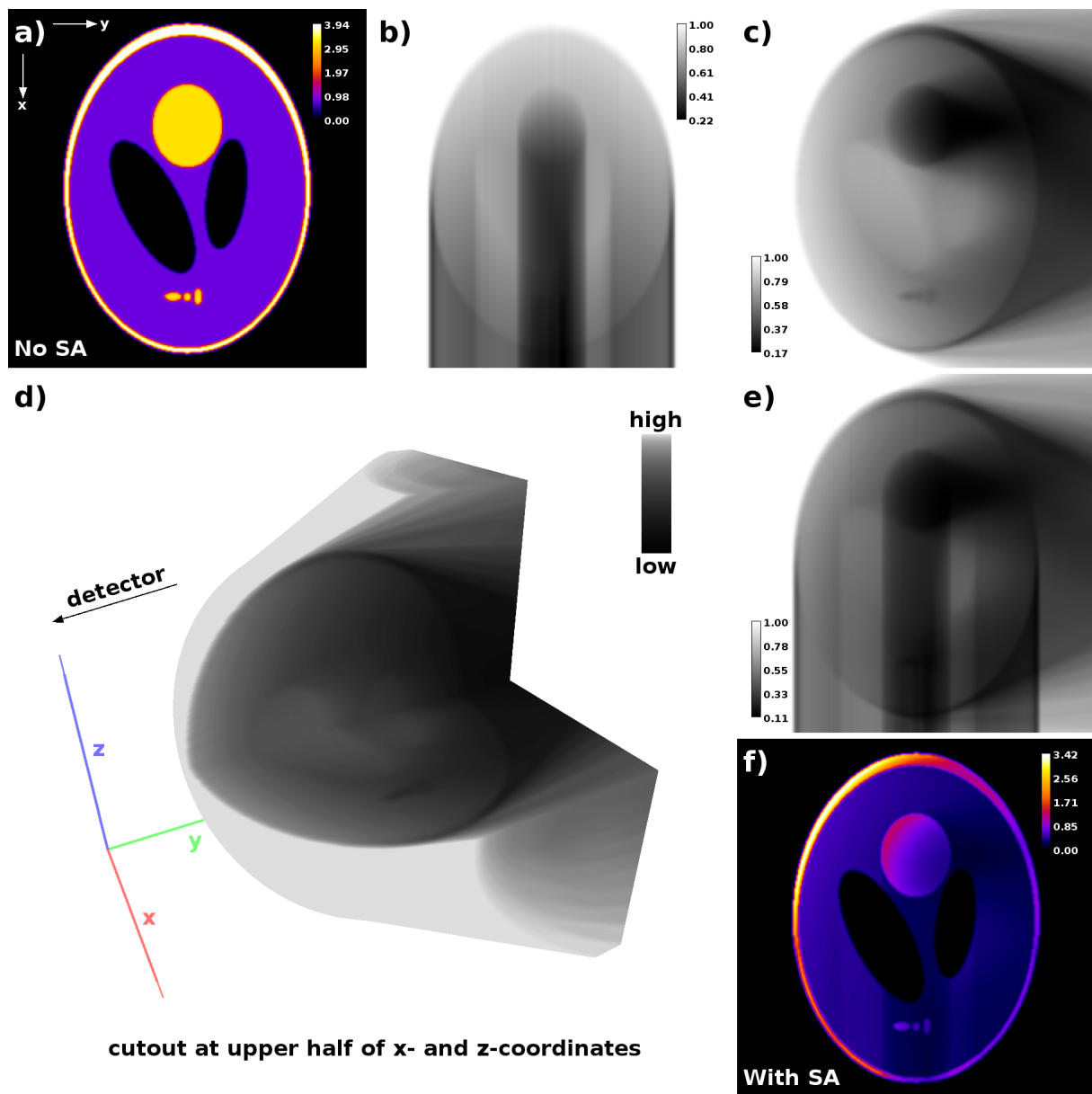


Figure 4.4: Self absorption effects at a single angle. a) shows the density of a central slice of an Fe-phantom in g/cm^3 , with the x -direction being the X-ray beam direction and the detector being placed in negative y -direction. b) shows the fraction of the primary beam reaching each voxel of the central slice and c) the fraction of the emitted XRF signal per voxel leaving the sample. d) shows a 3D rendering of the full volume corresponding to c), minus a cutout at high x - and z -coordinates for visualization. e) is the product of b) and c) and illustrates the combined effect of primary beam and XRF absorption. f), the product of a) and e), is a measure for the effectively detected density and used to construct a line of the sinogram. The 3D rendering was created in Drishti [Lim12].

with d being the voxel size of the sample volume. Thus, the x -components of the detector directions are decreased if the x -component of the voxel position is larger than the x -center of the sample volume and increased if it is smaller. The y - and z -components of the detector directions stay unchanged, as only the sample is scanned along those directions, while the position of the primary beam and detector are fixed.

The length of the detector direction $\vec{p}_j^{\vec{v}}$ as calculated in equation 4.13 is equal to the distance between the x -component of the voxel position placed on the primary beam and the detector pixel j . To be able to calculate the sum along the detector directions on the scale of the sample volume, they have to be normalized to unit vector length:

$$\hat{p}_j^{\vec{v}} = \frac{\vec{p}_j^{\vec{v}}}{\|\vec{p}_j^{\vec{v}}\|} \quad (4.14)$$

The sums of optical depths along the direction to detector element j are then calculated starting with half the value of the initial voxel \vec{v} followed by values from different coordinates, which are calculated by adding steps of $\hat{p}_j^{\vec{v}}$ to \vec{v} until the edge the the volume is reached:

$$s_{L,\varphi_i,j}(x,y,z) = \frac{1}{2} \tau_{L,\varphi_i}^{(k)}(x,y,z) + \sum_{n=0}^{n_{max}} \tau_{L,\varphi_i}^{(k)}(NN(\vec{v} + n\hat{p}_j^{\vec{v}})) \quad (4.15)$$

where n_{max} is the amount of steps $\hat{p}_j^{\vec{v}}$ from starting voxel \vec{v} necessary to reach the edge of the volume and $NN(\vec{u})$ is the 3D nearest-neighbor interpolation, which is used for efficiency and simplicity:

$$NN(\vec{u}) = (\lfloor u_x + 0.5 \rfloor, \lfloor u_y + 0.5 \rfloor, \lfloor u_z + 0.5 \rfloor) \quad (4.16)$$

Following that, the Beer-Lambert law (eq. 2.7) is used to calculate the transmission volume corresponding to the detector direction:

$$t_{L,\varphi_i,j}(x,y,z) = e^{-s_{L,\varphi_i,j}(x,y,z)} \quad (4.17)$$

Finally, the average of the transmission volumes for all detector directions has to be calculated:

$$t_{L,\varphi_i}(x,y,z) = \frac{1}{n_j} \sum_j t_{L,\varphi_i,j}(x,y,z) \quad (4.18)$$

Algorithm 4.2 shows a pseudo-code implementation of the XRF transmission calculation. Figure 4.4 c) shows a simulated example slice of an XRF transmission volume calculated with an XRF detector placed at an angle of 270° . Its values display the fraction of emitted XRF radiation that reaches the detector for each voxel. Compared to the slice of the primary beam transmission shown in figure 4.4 b), it can be seen that the shadowing effect caused by the XRF absorption in the sample is not limited to a single direction, which is a consequence of the XRF detector being a 2D object. This effect can be seen more clearly in the 3D rendering of the XRF transmission volume shown in figure 4.4 d), as even slices above and below the sample

Algorithm 4.2: XRF Radiation Transmission

Data: Rotated XRF absorption volume $\tau_{L,\varphi_i}^{(k)}$, n_j detector directions \vec{p}_j , voxel size d

Result: XRF transmission volume $t_{L,\varphi_i}^{(k)}$

Calculation at iteration k for XRF line L under an angle φ_i ;

Define x -axis as primary beam direction and $\tau = \tau_{L,\varphi_i}^{(k)}$;

Calculate center of volume with n_x voxel in x -direction: $c_x = \lfloor n_x/2 \rfloor$;

for all voxel $\vec{v} = (v_x \in \mathbb{N}_0, v_y \in \mathbb{N}_0, v_z \in \mathbb{N}_0)$ **in volume** τ **do**

 Modify x -components of detector directions: $p_{j,x} \leftarrow p_{j,x} - d(v_x - c_x)$;

 Normalize detector directions: $\hat{p}_j = \vec{p}_j / \|\vec{p}_j\|$;

for all detector directions \hat{p}_j **do**

 Define start position: $\vec{u} = \vec{v}$;

 Initialize absorption sum: $s_L = (\tau)_{\vec{u}}/2$;

 Update position: $\vec{u} \leftarrow \vec{u} + \hat{p}_j$;

while position \vec{u} **exists in volume** τ **do**

 Find nearest-neighbor: $NN(\vec{u}) = (\lfloor u_x + 0.5 \rfloor, \lfloor u_y + 0.5 \rfloor, \lfloor u_z + 0.5 \rfloor)$;

 Add nearest-neighbor value to absorption sum: $s_L \leftarrow s_L + (\tau)_{NN(\vec{u})}$;

 Update position: $\vec{u} \leftarrow \vec{u} + \hat{p}_j$;

end while

 Calculate transmission for detector direction: $(t)_{\vec{v},j} = e^{-s_L}$;

end for

 Average transmission of all detector directions: $(t)_{\vec{v}} = \frac{1}{n_j} \sum_j (t)_{\vec{v},j}$;

end for

return $t_{L,\varphi_i}^{(k)} \leftarrow t$

are influenced by the self-absorption effect.

There are two special cases of XRF transmission calculation that should be mentioned. The first one is the small-sample approximation, which can be applied if the sample is small compared to the XRF detector. Mathematically, this condition is fulfilled if the maximum change to the x -component of the detector direction as calculated in equation 4.13 is much smaller than the maximum y -component for the detector pixel as calculated in equation 4.3: $d(v_{x,max} - c_x) \ll d_{det}(y_{det,max} - c_{det,y})$. In this case it is sufficient to use the detector directions as determined during the initial calculations and to skip the voxel-dependent modification of their x -components. As a consequence, the detector directions can be fully calculated and normalized in advance, which reduces the number of operations that have to be performed during the XRF transmission calculation.

The second case is the single-slice approximation, which has to be used if only a single slice instead of a full volume is measured. In this case it is assumed that the sample is homogeneous in z -direction. To maintain the correct path length of the emitted XRF signal through the sample, the z -components of the detector directions are set to zero after normalization (eq. 4.14). Otherwise, the single-slice approximation follows the conventional XRF transmission calculation algorithm.

Sinogram Calculation

After the primary beam transmission and XRF transmission volumes for XRF emission line L have been determined, the sinogram calculation has to be modified to account for the self-absorption effects. This is done by first calculating the product of primary beam and XRF transmission for every voxel at an specific angle (fig. 4.4 e) and then applying these factors to the rotated image function $f_{L,\varphi_i}(x, y, z)$ (fig. 4.4 f). The values of the modified image functions are then a measure for the part of the original values effectively detected by the XRF detector. Finally, the values of the modified rotated image functions are projected along the x -axis to create the sinograms:

$$g_L(y, i, z) = \sum_x t_{0,\varphi_i}(x, y, z) \cdot t_{L,\varphi_i}(x, y, z) \cdot f_{L,\varphi_i}(x, y, z) \quad (4.19)$$

The pseudo-code implementation of the modified sinogram calculation is shown in algorithm 4.3. Its general structure follows the one of the Radon transform as defined in algorithm 3.1, but it additionally accounts for the change of the tomographic model in the self-absorption case by incorporating the primary beam and XRF absorption volumes.

Algorithm 4.3: Sinogram Calculation

Data: Intensity volume $f_L^{(k)}$, primary beam absorption volume τ_0^{meas} , XRF absorption volume $\tau_L^{(k)}$, list of angles φ_i

Result: Simulated sinograms $g_L^{(k)}$

Calculation at iteration k for XRF line L ;

Assume projection along x -axis with a length of n_x elements;

Assume rotation around z -axis;

Define $f = f_L^{(k)}$, $\tau_0 = \tau_0^{meas}$ and $\tau_L = \tau_L^{(k)}$;

for all angles φ_i do

 Rotate f , τ_0 and τ_L by an angle φ_i into f_{φ_i} , τ_{0,φ_i} and τ_{L,φ_i} ;

 Alg. 4.1: Calculate primary beam transmission volume t_{0,φ_i} ;

 Alg. 4.2: Calculate XRF transmission volume t_{L,φ_i} ;

 Multiply intensity and transmission volumes: $f_{SA,\varphi_i} = t_{0,\varphi_i} \odot t_{L,\varphi_i} \odot f_{\varphi_i}$;

for all voxel $\vec{v} = (0, v_y \in \mathbb{N}_0, v_z \in \mathbb{N}_0)$ in volume f_{SA,φ_i} do

 Fill the sinogram with sum along x : $(g)_{v_y, i, v_z} = \sum_{x=0}^{n_x-1} (f_{SA,\varphi_i})_{x, v_y, v_z}$;

end for

end for

return $g_L^{(k)} \leftarrow g$

Figure 4.5 shows the sinograms resulting from calculating the conventional and the self-absorption Radon transform of the phantom and with the measurement geometry as defined in figure 4.4. There are two main differences between conventional and self-absorption sinogram. First, the self-absorption sinogram is lacking the symmetry of the conventional sinogram, as its values show the tendency to decrease the more they are shadowed by the parts of the sample facing the detector. In performing self-absorption influenced XRF tomography

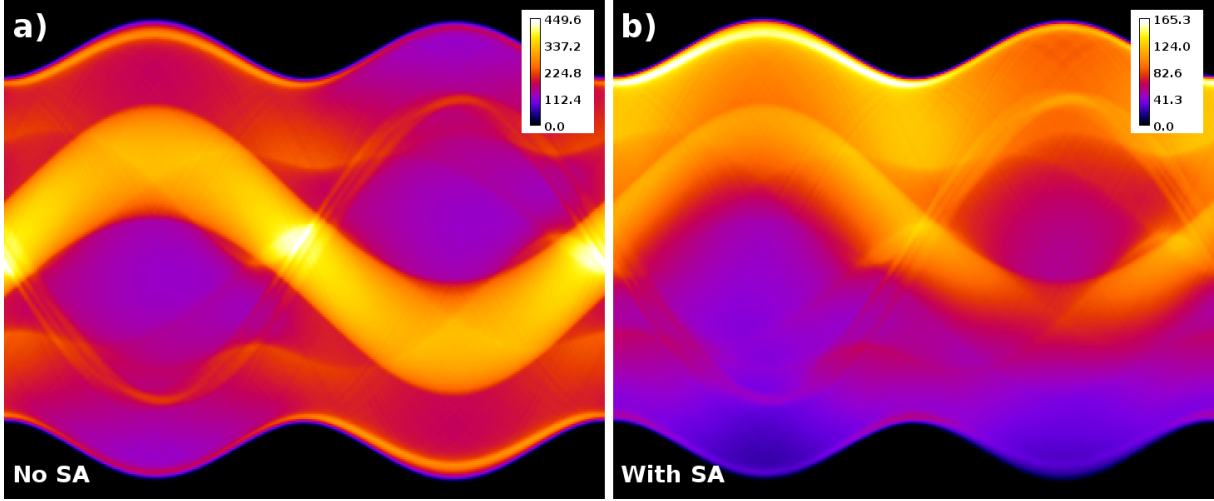


Figure 4.5: a) Conventional Radon transform and b) self-absorption Radon transform of the central slice of the Fe-phantom using the density values and geometry shown in figure 4.4. The values are given as integral density.

experiments it is therefore advisable to measure the full 360° angular range instead of just the 180° angular range that would be sufficient for symmetric sinograms. Second, the values of the self-absorption sinogram are always lower than those of the conventional sinogram. This is especially important to note as it is sometimes tried to correct self-absorption effects by combining the measurements from multiple XRF detectors placed at different angles, which may mitigate some of their qualitative and quantitative consequences but cannot replace performing a dedicated self-absorption correction.

4.2.3 Self-Absorption MLEM Algorithm

The self-absorption MLEM algorithm uses the self-absorption Radon transform and, in extension, the given self-absorption model to find the most likely reconstruction to a measured sinogram by ensuring that reconstruction and sinogram are consistent. As this section focuses on the derivation of the self-absorption MLEM algorithm, it is assumed that the primary beam absorption volume τ_0^{meas} as well as the XRF absorption volume $\tau_L^{(k)}$ are known *a priori*. For most real-world cases however, the XRF absorption volume is unknown and has to be calculated separately at the beginning of every iteration of the MLEM algorithm.

As shown in the previous section covering the self-absorption radon transform, especially in equation 4.19, the mean number of events including self-absorption effects $\bar{f}_{SA,ij}$ in pixel j depending on a related bin i can be described as:

$$\bar{f}_{SA,ij} = t_{0,ij} \cdot t_{L,ij} \cdot \bar{f}_j \quad (4.20)$$

where $t_{0,ij}$ is the fraction of the primary beam reaching the pixel, $t_{L,ij}$ the fraction of the emitted XRF photons leaving the sample and \bar{f}_j the mean number of events without self-absorption effects.

Inserted into equation 3.20, the mean number of events $\bar{g}_{SA,i}$ detected in bin i can then be calculated as:

$$\bar{g}_{SA,i} = \sum_{j=1}^m a_{ij} \bar{f}_{SA,ij} \quad (4.21)$$

with a_{ij} being the probability that an event in pixel j gets detected in bin i .

Assuming there are no additional effects breaking the Poisson characteristic of the measurement, for example higher-order XRF effects, the further derivation of the self-absorption MLEM algorithm follows the derivation of the conventional MLEM algorithm as described in equation 3.21 to equation 3.26. Consistent with [LYQ⁺15], the iterative equation for the self-absorption MLEM algorithm then results in:

$$\bar{f}_j^{(k+1)} = \frac{\bar{f}_j^{(k)}}{\sum_{i=1}^n a_{ij}} \sum_{i=1}^n \frac{g_{SA,i}}{\sum_{j'=1}^m a_{ij'} \bar{f}_{SA,ij'}^{(k)}} a_{ij} \quad (4.22)$$

with the corresponding pseudo-code implementation shown in algorithm 4.4.

Algorithm 4.4: Tomographic Self-Absorption MLEM

Data: Measured sinogram g_L^{meas} , number of iterations n_k

Result: Self-absorption corrected reconstructed slice $f_L^{(n_k)}$

Calculation for XRF line L ;

Assume τ_0^{meas} and $\tau_L^{(k)}$ are known;

Initialize the slice with a first guess, e.g. with a backprojection: $f_L^{(0)} = BP(g_L^{meas})$;

$k = 0$;

while $k < n_k$ **do**

Alg. 4.3: Simulate self-absorption sinogram $g_L^{(k)}$;

Divide measured and simulated sinograms: $r_g = g_L^{meas} \oslash g_L^{(k)}$;

Backproject into a slice: $f_{ratio} = BP(r_g)$;

Update by multiplication: $f_L^{(k+1)} = f_L^{(k)} \odot f_{ratio}$;

$k \leftarrow k + 1$;

end while

return $f_L^{(n_k)}$

The same logical description that applies to the conventional MLEM algorithm also applies to the self-absorption MLEM algorithm. If the values of the simulated sinograms are too low, then update will increase the values of the reconstructed slices and *vice versa*. However, it is important to note that, if the XRF absorption volume is unknown and has to be recalculated every iteration, the model to calculate the simulated sinograms will also change every iteration. Therefore, the change in the simulated sinograms is not only dependent on the change of the reconstructed slices anymore, but also on the change of the model. This increases the complexity of the algorithm and may slow its convergence.

Figure 4.6 shows MLEM reconstructions of the central slice of the Fe-phantom for different

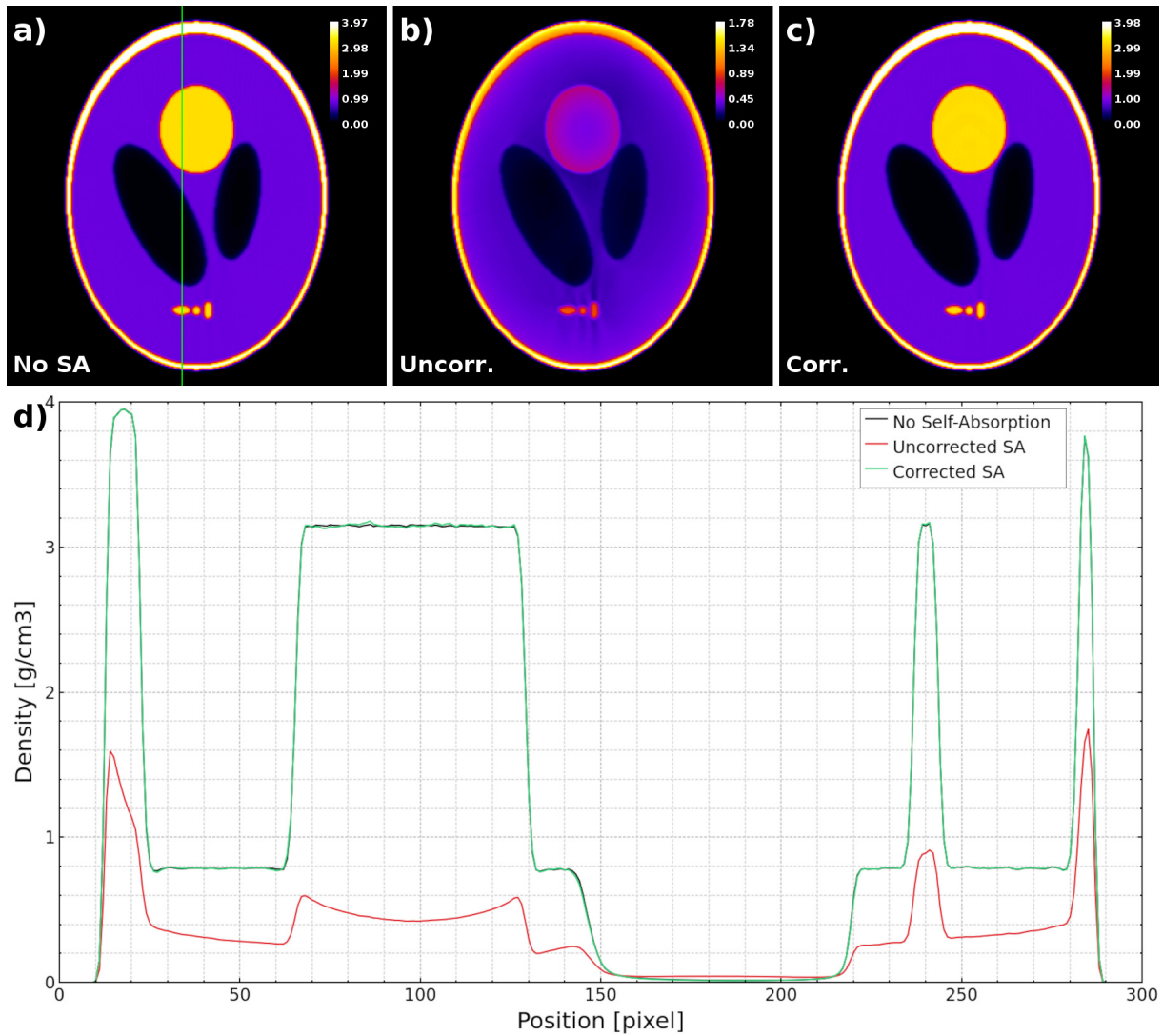


Figure 4.6: Tomographic reconstructions of the central slice of the Fe-phantom a) without self-absorption effects, b) with uncorrected self-absorption effects and c) with corrected self-absorption effects. The values at the color bars are given as densities in g/cm^3 and all reconstruction were performed using an initial 100 iterations of MLEM-FMH with $\beta = 0.3$ followed by 200 iterations of MLEM. The vertical green line in a) marks the position of the line profiles plotted in d).

cases as well as a line profile through every reconstruction. a) is the MLEM reconstruction of the sinogram shown in figure 4.5 a) and illustrates the case of no self-absorption effects for comparison. b) and c) are reconstructions of the self-absorption sinogram shown in figure 4.5 b) with conventional and self-absorption MLEM, respectively. As can be seen, the uncorrected reconstruction suffers from a generally lower reconstructed density as well as from shadowing of inner parts of the sample. In contrast, the corrected reconstruction does not suffer from these effects. Except for a slight increase in noise, as visible in the plot of the line profiles, its density levels are consistently similar to those of the reconstruction without self-absorption effect.

4.2.4 Consistency Refinement Loop

The consistency refinement loop serves three important purposes: Given an experimental calibration, it ensures that the reconstructed XRF volumes are consistent with the measured absorption volume. Furthermore, it calculates and updates the background absorption, if applicable. Finally, it updates the XRF absorption volumes, which are input into the self-absorption model.

Density Calibration

Before the reconstructed XRF volumes can be used to simulate an absorption tomogram their values have to be converted from intensities given in counts to area mass densities given in g/cm^2 . To calculate the area mass density distribution $\rho_{2D,L}^{(k)}$ for an XRF line L from the k -th iteration intensity volume $f_L^{(k)}$ the calibration factor $P_{cal,L}$ is used:

$$\rho_{2D,L}^{(k)} = P_{cal,L} \cdot f_L^{(k)} \quad (4.23)$$

These calibration factors are either directly measured at the experiment using calibration foils or theoretically calculated using experimental parameters (e.g. eq. 6.7).

If there are multiple reconstructed lines for an element Z , the final area mass density distribution of this element is calculated by averaging the individual density distributions of all lines belonging to this element:

$$\rho_{2D,Z}^{(k)} = \frac{1}{n_Z} \sum_{L=1}^{n_Z} \rho_{2D,L}^{(k)} \quad (4.24)$$

where n_Z is the amount of reconstructed lines for the element Z .

Assuming that all reconstruction and calibration parameters are correct, the density calibration for all lines of an element should lead to a singular elemental area mass density distribution. Thus, the error between the reconstruction of a single line calculated against the average of all lines, $NMAE(\rho_{2D,L}, \rho_{2D,Z})$ as defined in equation 3.33, can be used to monitor the process and quality of the reconstruction. However, this calculation will be less accurate in presence of noise, as the increase in noise with higher iterations will invariably increase the calculated error. The subsequent calculations of the consistency refinement loop assume the densities of all elements are given as area mass density distributions $\rho_{2D,Z}$. For the final results however, these area mass densities may be converted into volume mass density distributions $\rho_{3D,Z}$ to better represent the 3-dimensional nature of tomography by dividing them by the voxel size in the direction parallel to the beam direction d_{\parallel} :

$$\rho_{3D,Z} = \frac{\rho_{2D,Z}}{d_{\parallel}} \quad (4.25)$$

In contrast to the actual voxel sizes in the plane intersected by beam, $d_{\rightarrow,x}$ and $d_{\rightarrow,y}$, which are defined by the beam size, d_{\parallel} is only defined by the step size of the measurement and therefore accessible without further experiments.

Density Constraints

In some cases, especially if the self-absorption correction algorithm is used with background, it may be beneficial for the reconstruction to include *a priori* information about the elemental distribution inside the sample, for example by applying a support.

If a low absorption region of the sample is known to contain background but none of the reconstructed elements, an absorption threshold T_L can be used to define a support for the elemental density distributions:

$$\rho_{2D,Z}^{(k)} \leftarrow \begin{cases} \rho_{2D,Z}^{(k)}, & \tau_{att}^{meas} \geq T_L \\ \lambda_L \cdot \rho_{2D,Z}^{(k)}, & \tau_{att}^{meas} < T_L \end{cases} \quad (4.26)$$

The limiting factor λ_L is used to prevent the elemental densities from being limiting too strongly which may cause the background to grow too fast and cause artifacts in the reconstruction.

Absorption Normalization

Following the density calculations, the XRF tomography data is adjusted to the absorption tomography data to improve the consistency of both datasets.

In the first step, assuming the absence of any background, the elemental area mass density distributions $\rho_{2D,Z}^{(k)}$ are used to simulate the absorption volume $\tau_0^{(k)}$ at the primary beam energy. From equation 2.10 it follows that:

$$\tau_0^{(k)} = \sum_Z \frac{N_A}{M_Z} \rho_{2D,Z}^{(k)} \sigma_{att,Z}(E_0) \quad (4.27)$$

where k is the number of the current iteration, N_A the Avogadro constant, M_Z the molar mass and $\sigma_{att,Z}(E_0)$ the attenuation cross section of element Z at the primary beam energy E_0 .

After that, the ratio volume $r_0^{(k)}$ between the measured absorption volume τ_0^{meas} and the simulated absorption volume is calculated:

$$r_0^{(k)} = \tau_0^{meas} \oslash \tau_0^{(k)} \quad (4.28)$$

The ratio is then multiplied with the elemental area density distributions to calculate scaled elemental area density distributions $\hat{\rho}_{2D,Z}^{(k)}$:

$$\hat{\rho}_{2D,Z}^{(k)} = \rho_{2D,Z}^{(k)} \odot r_0^{(k)} \quad (4.29)$$

so that the scaled elemental area density distributions are consistent with the measured absorption volume and equation 4.30 is fulfilled:

$$\tau_0^{meas} = \sum_Z \frac{N_A}{M_Z} \hat{\rho}_{2D,Z}^{(k)} \sigma_{att,Z}(E_0) \quad (4.30)$$

It has to be noted that the normalization to the measured absorption values is only performed

on the calculated elemental area mass density distributions for the purpose of updating the absorption volumes at the XRF emission line energies and therefore to update the self-absorption Radon model. The intensity volumes of the MLEM algorithm itself are not scaled to isolate the tomographic reconstructions and prevent elemental cross-talk.

Background Calculation

If an absorption background is used, its initial values are calculated by taking the difference between the measured and the simulated absorption volumes, as long as the simulated absorption is smaller than the measured one:

$$\tau_{BG,0}^{(0)} = \begin{cases} \tau_0^{meas} - \tau_0^{(0)}, & \tau_0^{meas} - \tau_0^{(0)} > 0 \\ \varepsilon, & \tau_0^{meas} - \tau_0^{(0)} \leq 0 \end{cases} \quad (4.31)$$

where $\varepsilon > 0$ is a small positive real number close to zero. The usage of ε is required to prevent parts of the background absorption volume being stuck at zero-values, as the method of updating the background follows a multiplicative *ansatz*. Furthermore, as the background now accounts for situations where the simulated absorption is smaller than the measured one, the ratio volume used to scale the density distributions (eq. 4.28) has to be adjusted accordingly:

$$r_0^{(0)} = \begin{cases} 1, & \tau_0^{meas} - \tau_0^{(0)} \geq 0 \\ \tau_0^{meas} \oslash \tau_0^{(0)}, & \tau_0^{meas} - \tau_0^{(0)} < 0 \end{cases} \quad (4.32)$$

meaning that the elemental density distributions will be limited to be consistent with the measured absorption if their simulated absorption exceeds the measured one and be kept constant otherwise. It has to be noted that this change to the absorption volume ratio is only performed during the first iteration the background is calculated in but not during following iterations.

As the recalculation of the background every iteration could lead to strong changes in the self-absorption model and thus possibly to oscillating behavior of the self-absorption correction algorithm, the background is kept persistent and treated equally to the density distributions during subsequent iterations. To this mean, equation 4.27 is modified to include the background of the previous iteration:

$$\tau_0^{(k)} = \sum_Z \frac{N_A}{M_Z} \rho_{2D,Z}^{(k)} \sigma_{att,Z}(E_0) + \tau_{BG,0}^{(k-1)} \quad (4.33)$$

After calculating the ratio of the measured and simulated absorption volumes, the background absorption volume is then updated using a variation of equation 4.29:

$$\tau_{BG,0}^{(k)} = \tau_{BG,0}^{(k-1)} \odot r_0^{(k)} \quad (4.34)$$

This background refining is slower to act to changes in the self-absorption model compared to complete recalculation of the background and thus stabilizes the algorithm.

Background Constraints

In general, it can be assumed that the background is limited by the self-consistency of the algorithm. As the background, per definition, lacks absorption edges in the relevant energy range, its absorption increase in the direction of lower energies can be fully approximated using a scaling law (eq. 4.9). In contrast, the absorption increase of all relevant elements in the direction of lower energies is reduced by crossing their absorption edges. An overestimated background therefore leads to comparatively increased simulated absorption of the emitted XRF signals and thus to less intensity in the simulated sinograms. Low-intensity simulated sinograms inserted into the MLEM algorithm then lead to an increase in the intensity volumes and density distributions, which in turn reduces the background.

However, this explanation does not consider the artifacts that can be caused by an overestimated or incorrectly distributed background. For example, if the background is overestimated but the increase in the intensity volumes is not large enough to cause a sufficient reduction of the background, the values of the intensity volumes continue to increase. However, because of the influence of the self-absorption effects on the symmetry of the sinograms, this increase is not uniform but mostly located towards the edge of the reconstructed sample. Meanwhile, the intensity values towards the center of the sample increase less or even decrease. This may lead to the accumulation of background signal in the center of the sample, worsening the reconstruction artifacts in a positive feedback loop. In the worst case, this creates a “black hole artifact” where the reconstructed intensity volumes only consist of a bright, high-value halo at the edge of the reconstructed sample area, while the entire inner part of the sample is assumed to be background. It is therefore important to constrain the background in those cases in which it may be overestimated too strongly.

One method of constraining the background is to introduce a background slope for early iterations. This method is especially useful if low elemental density distributions during the early steps of the algorithm are causing a temporarily overestimated background. To apply the slope, all values of the background are multiplied with a sloping factor:

$$\tau_{BG,0}^{(k)} \leftarrow \tau_{BG,0}^{(k)} \frac{k}{\lambda_{slp}}, \text{ as long as } k \leq \lambda_{slp} \quad (4.35)$$

where $\lambda_{slp} \in \mathbb{N}_1$ defines the sloping strength.

Alternatively, if the background problems are of a more permanent nature, for example caused by an incorrect calibration, it may be beneficial to analyze the reconstruction artifacts caused by the overestimated background and to continuously limit the background based on how the artifacts develop during the reconstruction process. As a strongly overestimated background causes strong, localized increases of values in the simulated sinograms and thus also in the backprojection of the simulated sinograms, a simple way of limiting the background can be based on the comparison of the higher values of both the backprojection of the simulated and the measured sinogram. In the current implementation this is done by determining the slice-wise averages of all values higher than 90% of the slice maximum value and calculating the

ratios $\lambda_{L,z}^{(k)}$ of these values for the backprojection of the measured and simulated sinograms. The ratios are then weighted to the sum of counts in the corresponding measured sinograms and averaged for all slices to reduce the influence of noise:

$$\lambda_L^{(k)} = \frac{\sum_{x,y,z} \lambda_{L,z}^{(k)} \cdot g_L^{meas}(x,y,z)}{\sum_{x,y,z} g_L^{meas}(x,y,z)} \quad (4.36)$$

A smaller $\lambda_L^{(k)}$ may be an indication that background artifacts are present in the reconstructed volume of line L . To calculate the background limiting factor $\lambda_{BG}^{(k)}$, the minimum of all $\lambda_L^{(k)}$ is used:

$$\lambda_{BG}^{(k)} = \frac{\min_L(\lambda_L^{(k)})}{\lambda_{trg}} \quad (4.37)$$

where λ_{trg} is a target value close to 1 that determines the sensitivity of the background limiting. The limiting factor is then used to modify the ratio volume for the update of the background in equation 4.34 to have a maximum value of 1 as long as the background limiting factor is smaller than 1:

$$r_0^{(k)} \leftarrow \begin{cases} 1, & \lambda_{BG}^{(k)} < 1 \text{ and } r_0^{(k)} > 1 \\ r_0^{(k)}, & \text{else} \end{cases}, \text{ only for eq. 4.34} \quad (4.38)$$

This modification to the update step ensures that the background does not grow if there are indications of background artifacts.

Additionally, this form of background constraint allows the implementation of an adaptive calibration for the elemental data. If the limiting factor is consistently smaller than λ_{trg} and the majority of the values of the ratio volume are larger than 1, there is a high possibility of inconsistencies in the elemental calibration. In this case, a persistent adaptive calibration factor $C_{adpt}^{(k)}$ with an initial value of $C_{ada}^{(0)} = 1$ may be introduced. The calibration factor is updated using the average of all nonzero values of the unlimited ratio volume:

$$C_{ada}^{(k)} \leftarrow C_{ada}^{(k-1)} \frac{\sum_{x,y,z} r_0^{(k)}}{n_{r \neq 0}} \quad (4.39)$$

where $n_{r \neq 0}$ is the amount of nonzero elements of $r_0^{(k)}$ and with the additional limitation that the adaptive calibration factor is not allowed to increase if $\lambda_{BG}^{(k)} > \lambda_{trg}$ and not allowed to decrease if $\lambda_{BG}^{(k)} < \lambda_{trg}$. The limitation ensures that the adaptive calibration will not prevent the background from growing as long as the possibility of background artifacts is low. In the subsequent iteration, the updated adaptive calibration factor is used to modify the elemental calibration factors as used in equation 4.23:

$$\rho_{2D,L}^{(k)} = C_{ada}^{(k-1)} \cdot P_{cal,L} \cdot f_L^{(k)} \quad (4.40)$$

As the combination of scaled elemental area density distributions and constrained background volumes is not consistent with the measured primary beam absorption tomogram anymore, the elemental area density distributions have to be rescaled to account for the lower background:

$$\hat{\rho}_{2D,Z}^{(k)} \leftarrow \hat{\rho}_{2D,Z}^{(k)} \odot \left(\left(\tau_0^{meas} - \tau_{BG,0}^{(k)} \right) \oslash \tau_0^{(k)} \right) \quad (4.41)$$

These methods of constraining the background mitigate or prevent background artifacts, lead to qualitative improvement of the reconstructions and, in most cases, assure that the algorithm reaches a stable equilibrium. However, as the constraining of the background interferes with the main part of the self-absorption correction algorithm and potentially also with the elemental calibration, it has to be noted that the quantitativity of the reconstructions may suffer, even if an equilibrium is reached.

Absorption Estimation

After assuring that the calculated density distributions are consistent with the measured absorption volume, they are used to calculate the XRF absorption volumes for every emission line:

$$\tau_L^{(k)} = \sum_Z \frac{N_A}{M_Z} \hat{\rho}_{2D,Z}^{(k)} \sigma_{att,Z}(E_L) \quad (4.42)$$

or alternatively, if an additional background is used:

$$\tau_L^{(k)} = \sum_Z \frac{N_A}{M_Z} \hat{\rho}_{2D,Z}^{(k)} \sigma_{att,Z}(E_L) + \tau_{BG,L}^{(k)} \quad (4.43)$$

where the background absorption volume at the XRF line energy $\tau_{BG,L}^{(k)}$ is calculated as defined in equation 4.10.

The XRF absorption volumes are then used as updated inputs for the self-absorption Radon transform inside of the self-absorption MLEM algorithm 4.4.

4.3 Technical Implementation

The tomographic self-absorption correction algorithm is implemented in C++ with the most critical and time-consuming functions also implemented in *CUDA*. Most of the custom functions of the algorithm are written with a focus on parallelization, either on CPU or GPU. This leads to an increase in computational speed and allows to correct for self-absorption using the full 3D measurement geometry. To decrease the dependency on third-party code, the algorithm only relies on a small amount of external packages. As it would be inconvenient to have to recompile the code for every change of parameters, a config-file based approach using an additional text-file was chosen. The most recent version of the self-absorption correction algorithm code can be found in the DESY Gitlab under: <https://gitlab.desy.de/fs-petra/software/mlemsa> (access restrictions may apply).

4.3.1 Dependencies

Most of the self-absorption correction algorithm code is implemented using the C++ standard library. Additional third-party code dependencies are *OpenCV* to be able to load and save .tif image files, *xraylib* [SBG⁺11] which includes tabulated values for the energies of XRF emission lines and attenuation cross sections, among others, as well as *OpenMP* and *CUDA* for the parallelization of CPU and GPU calculations, respectively.

4.3.2 Arrays

All 3D volumes and sinogram stacks utilized during the self-absorption correction algorithm are implemented as 1D dynamic arrays with their values depending on x -, y - and z -coordinates being accessed by using custom indexing. For one, this assures that all values of an array are saved close together in memory, increasing the chance that subsequent requested variables during loops are located in the cache of the processor and speeding up the calculation time. Furthermore, functions working on 1D arrays are easily translated into *CUDA* kernels, which simplifies the change from CPU to GPU parallelized code. Using 1D dynamic arrays in C++ also requires to manually control the memory management, which has advantages especially for memory expensive algorithm, but also creates the danger of memory leaks.

Regarding the arrays in the self-absorption correction algorithm, it is also important to specifically mention the topic of the primary beam transmission volumes t_{0,φ_i} . While it theoretically would be sufficient to calculate them just once at the beginning of the algorithm, saving a full volume for every angle of the tomographic measurement can quickly lead to memory problems. This is especially the case for limited GPU VRAM and even more so if the transfer rates between system RAM and VRAM are slow. For this reason, the current implementation only allocates one volume for the primary beam transmission, which is overwritten when the volume for the next angle is calculated. As the amount of operations necessary to calculate the primary beam transmission volumes is low compared to the amount needed to calculate the XRF trans-

mission volumes, this only slightly slows down the algorithm while it at the same time allows for full calculation on the GPU without memory problems.

4.3.3 Downscaling

The computationally most expensive part of the self-absorption correction algorithm is the calculation of the XRF transmission volumes (alg. 4.2), caused by the amount of sums that have to be calculated along the detector directions.

For example, using realistic values, a sample with a volume of 300^3 voxel, 361 recorded tomography angles and 64 detector directions would require the calculation of about $6.24 \cdot 10^{11}$ sums. Assuming that 6 XRF lines are reconstructed using 300 iterations of the self-absorption correction algorithm, the amount of sums that have to be calculated increases to about $1.12 \cdot 10^{15}$. Even on modern computational architecture and with parallelization, these calculations can take up to multiple weeks. This is a significant amount of time, especially if shared computational resources are used.

As it would be difficult and expensive to upscale the computational resources, the most simple way to speed up the calculation is to downscale the problem. For this reason, there is the possibility to downscale the XRF absorption volumes τ by a factor $n \in \mathbb{N}_1$ into τ_{DSn} before calculating the XRF transmission volumes. The downscaling is performed by calculating the averages of $n \times n$ regions inside the full volume:

$$\tau_{DSn}(x, y, z) = \frac{1}{n^2} \sum_{z'=0}^{n-1} \sum_{y'=0}^{n-1} \sum_{x'=0}^{n-1} \tau(nx + x', ny + y', nz + z') \quad (4.44)$$

Here, the sums are only divided by n^2 instead of n^3 to account for the effective elongation of the normalized detector direction vectors \hat{p} by a factor n in the downscaled coordinate system. For edge cases in which the amount of remaining voxel in one or more directions is smaller than n , the upper limits of the sums as well as the normalization factor are modified accordingly.

After rotation, the downscaled absorption volumes are used as input for algorithm 4.2 which results in downscaled versions of the XRF transmission volumes t_{DSn} . These volumes are then upscaled again to the full size using trilinear interpolation, so that they can be used in the subsequent steps of the algorithm.

The influence of downscaling on the transmission volume is illustrated in figure 4.7, using the sample and slice previously shown in figure 4.4. Comparing the slices for different downscale factors, it can be seen that, while the quantitative values stay on a similar level, the resolution decreases with increased downscaling. This behavior is a consequence of the averaging nature of the downscaling and has to be considered, especially for strongly inhomogeneous samples, as it may introduce additional inconsistencies into the self-absorption correction algorithm and decrease computational accuracy. For this reason, downscaling should only be used during the earlier iterations of the algorithm, while the final iterations should be performed without.

In theory, the maximum speedup due to downscaling approaches a factor of n^4 . The reduced

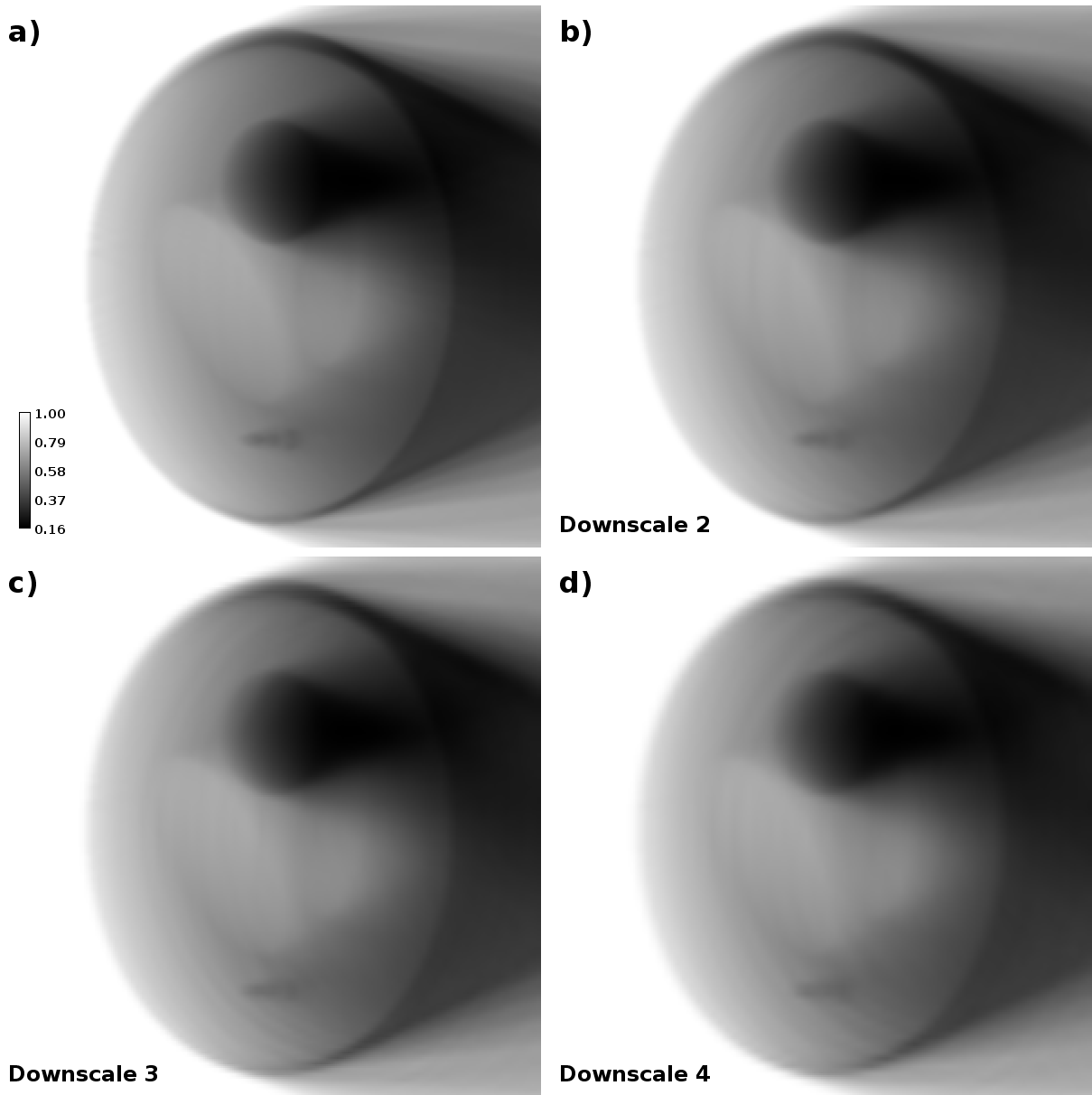


Figure 4.7: Central slice of the transmission volume of the Fe-phantom under one angle for multiple downscale factors.

number of voxel accounts for a factor of n^3 , while the reduced number of additions per detector direction accounts for up to an additional factor of n , depending on the number of addition operations compared to the number of operations for the calculation of the final exponential function. However, the final speedup per iteration is further limited by the overhead of all standard operations of the self-absorption correction algorithm as well as the additional overhead caused by the scaling operations. The exact speedup is also dependent on reconstruction parameters like the dimensions of the volume or the number of angles as well as computational parameters like the transfer rate from system to GPU memory.

Table 4.1 includes example speedup values per iteration for a dataset consisting of six 300^3 voxel tomographic volumes measured from 361 angles and using 64 detector directions. The reconstructions were calculated on a machine with an Intel Xeon Silver 4114 CPU, an

NVIDIA Tesla P100 GPU and 768 GB of RAM.

Table 4.1: Performance speedup achieved by downscaling

Downscale Factor n	Time per Iteration t_n [s]	Relative Speedup t_n/t_1	$\log_n(t_n/t_1)$
1	7418.1	1.0	-
2	534.8	13.87	3.79
3	152.2	48.72	3.54
4	86.3	85.96	3.21

It can be seen that downscaling significantly reduces the required computation time per iteration, from over 2 h without downscaling down to under 1.5 min using a downscale factor of $n = 4$. However, by calculating the logarithm of the relative speedup t_n/t_1 to base n , which would be equal to the exponent x when describing the speedup as n^x , it can also be seen that increased downscale factors lead to diminishing gains as the influence of overhead caused by the other operations of the algorithm increases. Therefore, it has to be noted that downscaling is only feasible up to a certain point, after which the decreased gain in speedup does not justify the decrease in computational accuracy anymore.

Finally, an additional advantage of downscaling is that faster earlier iterations make it easier to detect and solve problems that occur during the reconstruction.

4.3.4 Config-File

The config-file is a text file that defines parameters and flags for the self-absorption correction algorithm. Its purpose is to reduce the use of hard-coded values and thus the necessity for recompilation in case algorithm parameters have to be changed.

At the start of the algorithm, custom reader functions scan the given config-file for the necessary values and throw errors if they are not found or of the wrong type. If no config-file is given the algorithm creates an example config-file before exiting, which can then be adapted to the current tomographic problem.

A more detailed description of the parameters and flags defined in the config-file is given in the supplement.

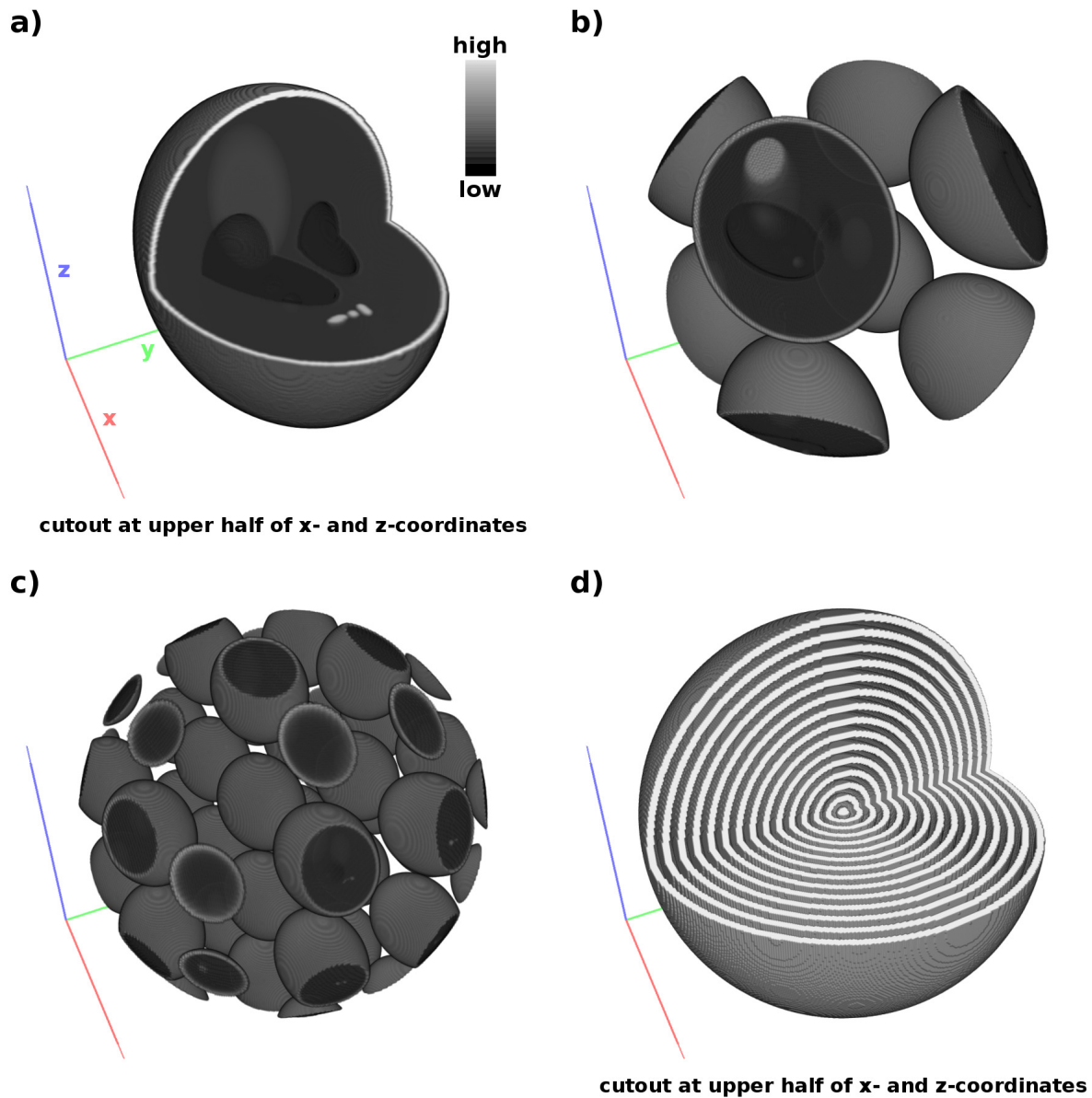


Figure 4.8: 3D renderings of the different phantoms used for the numerical simulations. Assigned elements are a) Fe, b) Ti, c) Zn and d) SiO_2 background. There are cutouts at high x - and z -coordinates in the renderings of a) and d) for visualization. The 3D renderings were created in Drishti [Lim12].

of SiO_2 of their corresponding compound, at room temperature for the single element cases and equal to a quarter for the multi-element cases.

The resulting self-absorption sinograms for Fe, Ti and Zn were simulated for both the $K\alpha$ and the $K\beta$ line and created in two batches: First, a noiseless version to simulate the ideal case performance, to monitor the reconstruction progress without the interference of noise and to be sensitive to small reconstruction problems and artifacts. Furthermore, noiseless sinograms are useful to check for unexpected behavior of the algorithm caused by zero-values, which rarely occur in noisy data.

The second batch of the simulated self-absorption sinograms was additionally modified to in-

clude Poisson noise to be able to simulate real-world performance. Each stack of sinograms was modified separately to include a unique noise distribution, with the Poisson noise applied assuming that the maximum value in the entire sinogram stack is equivalent to 10000 counts. For both batches, the simulated primary beam absorption volumes were kept free of noise. However, to stay consistent with the further treatment of the elemental data, the simulated primary beam absorption volumes were first Radon transformed into sinograms followed by 300 iterations of tomographic reconstruction using the conventional MLEM algorithm, of which the first 100 iterations were modified to include a FMH Bayesian prior (eq. 3.31) with a weight of $\beta = 0.3$.

4.4.3 Tomographic Reconstruction

The tomographic reconstructions of the simulated self-absorption sinograms utilize the reconstructed primary beam absorption volumes and the parameters as defined in the simulation step. No *a priori* information about the XRF absorption volumes or the spatial distribution of the background was used.

The reconstructions of all datasets were performed using 300 iterations of the tomographic self-absorption correction algorithm. To analyze the influence of downscaling on the accuracy of the reconstructions, the XRF transmission volumes were calculated using a downscale factor of 4 for the first 160 iterations, followed by 90 iterations using a downscale factor of 3, 40 iterations using a downscale factor of 2 and finally 10 iterations without downscaling. Furthermore, during the first 100 iterations the MLEM part of the algorithm was modified to include a FMH Bayesian prior (eq. 3.31) with a weight of $\beta = 0.3$ to determine the influence of OSL methods on the self-absorption correction.

As reconstruction artifacts inside the primary beam absorption volumes caused problems for the single-element cases simulated with background, those were additionally reconstructed with density limiting as implemented in equation 4.26 using a limiting factor of $\lambda_L = 0.5$.

Single Element (+Background)

The single-element cases include the simulations for the Fe-phantom without and with background, without and with noise and for the background cases also without and with density constraints. For each case, the full self-absorption corrected reconstructions required about 11.4 hours in computation time.

Figure 4.9 shows the logarithmic percentual normalized mean absolute errors (eq. 3.33) calculated for the mass density volume of the Fe- $K\alpha$ line against the average of the mass density volumes of Fe- $K\alpha$ and $-K\beta$ line depending on the iteration of the algorithm. Lower values indicate smaller errors between $K\alpha$ and $K\beta$ reconstruction and thus improved self-absorption correction.

For the “no background, no noise” case (light blue), the effects of downscaling on the error of the reconstruction are clearly visible. It can be seen that the NMAE decreases with the amount

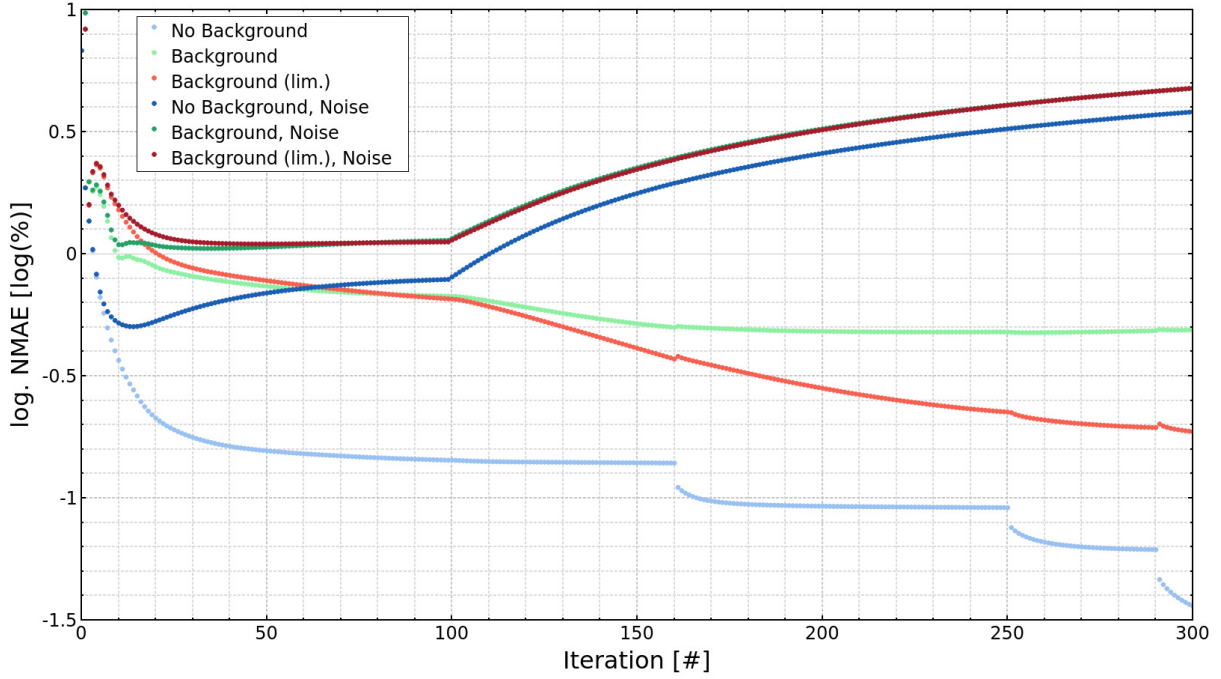


Figure 4.9: Logarithmic (\log_{10}) percentual normalized mean absolute errors (eq. 3.33) at different iterations for the single-element Fe simulations. Calculated is the error of the $K\alpha$ line reconstruction compared against the average of all line reconstructions.

of iterations, with the decrease eventually tapering off. Following the reduction of the down-scale factor at iterations 160, 250 and 290, it is possible to observe immediate improvements in the self-absorption correction as indicated by drops in the NMAE. This confirms the importance of performing the final iterations of the self-absorption correction algorithm without any downscaling. On the other hand, the FMH prior used during the first 100 iterations does not seem to have a big influence on the error of the reconstruction for this case, most likely because the Fe-phantom is homogeneous for big parts of the volume.

The error for the “background, no noise” case (light green) differs significantly from the “no background” case. As the background represents an additional unknown parameter during the reconstruction, the error in general is larger. Additionally, the FMH prior now has a visible influence on the error, indicated by a flattening curve before iteration 100. This is most likely caused by the averaging effect of FMH, which prevents the background from fully developing. After iteration 100, the error improves for a few iterations before it increases again. This increase in error is significant enough to overshadow the effects of reduced downscaling and caused by reconstruction artifacts in the absorption tomograms. These artifacts manifest themselves as excess intensity in otherwise empty regions inside the sample, which is incorrectly attributed to the Fe absorption instead of the background during the self-absorption correction algorithm. Defining and using a limiting constraint for the Fe density volumes during the reconstruction (orange line) mitigates this problem, as evident by a significant improvement of the NMAE.

All “noise” cases show similar behavior in their error development, mainly influenced by the

noise amplifying characteristics of the MLEM algorithm for increased numbers of iteration. As before, the error for the “no background” case (dark blue) is overall lower than those for the “background” cases (dark green, dark red). During the first 100 iterations of the reconstruction, the FMH prior limits the increase of noise and causes the error to approach an equilibrium. However, as soon as the FMH prior is deactivated, the noise, and with it the error, starts to grow continuously and strongly enough to mask the effects of all other changes applied during the reconstruction. Thus, the “noise” cases are not suited to analyze the finer changes in the self-absorption correction.

Figure 4.10 illustrates the results of the self-absorption correction reconstruction for the “background, noise” cases using the central slice of the tomographic volume. Reconstructions for the “no background, noise” case can be found in supplementary figure S1. Comparing the values of the Fe ground truth as shown in a) with the corrected reconstructions in c) and d) and also considering the uncorrected reconstruction in b), it becomes evident that, although the influence of noise significantly increases the error of the reconstruction, the self-absorption correction still improves the qualitative and quantitative properties of the reconstruction.

Furthermore, comparing the corrected reconstructions of the Fe without and with density limiting in c) and d) as well as the results for the background in f) and g) illustrates the nature of the reconstruction artifacts responsible for the increase in error in the “background” cases without limited constraints. Absorption signal supposed to be allocated to the background is instead allocated to the Fe reconstruction during earlier iterations of the algorithm and causes persistent artifacts. This effect can be mitigated using *a priori* knowledge of the sample and limiting the Fe density volumes in regions where no Fe is present.

The result for the background with density constraints itself is in good agreement with the ground truth in regions where no Fe is present or where the Fe densities are constrained. However, as the reconstruction of background is not supported by a measured sinogram, inconsistencies in the Fe density volume are transferred into the background where they manifest themselves as “imprint artifacts”. This is most likely one of the causes of the higher NMAE for “background” cases in general.

Table 4.2 shows the final normalized mean absolute errors of the reconstructed Fe density and background volumes calculated against their noiseless ground truths.

Table 4.2: Normalized mean absolute errors (eq. 3.33) of the reconstructed single-element simulations calculated against their noiseless ground truths.

NMAE(recon., truth)	Fe	Background
No Background	0.0027	-
Background	0.0313	0.2977
Background (lim.)	0.0115	0.1996
No Background, Noise	0.0357	-
Background, Noise	0.0531	0.5485
Background (lim.), Noise	0.0540	0.5355

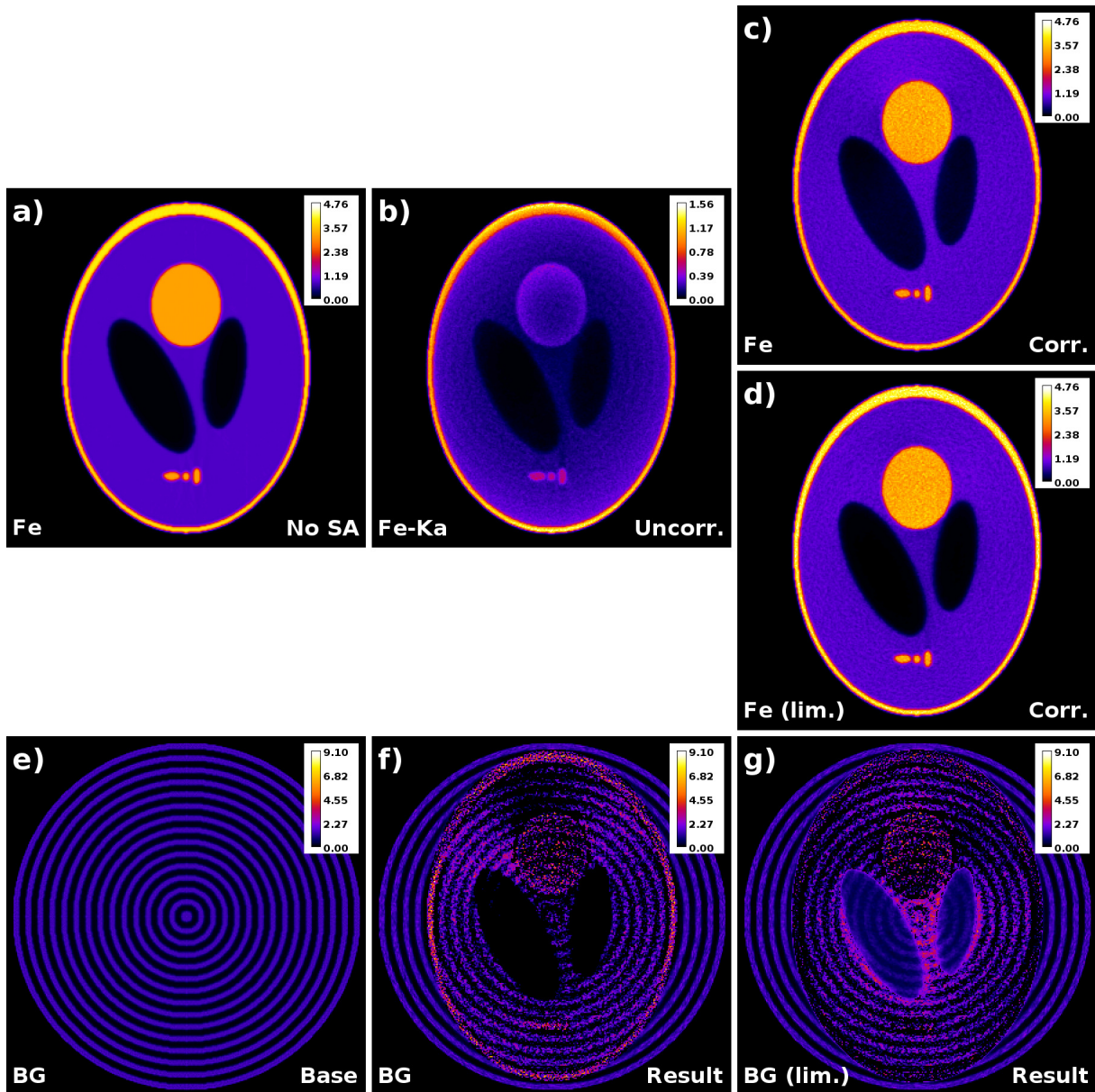


Figure 4.10: a) Ground truth and b) uncorrected ($K\alpha$) reconstruction for the noisy single-element Fe simulation with background. c) and d) are the corrected reconstructions without and with density constraints, respectively. For comparability reasons ground truth and corrected reconstruction are on an identical scale, while the uncorrected reconstruction is scaled separately for visibility. The e) ground truth, f) result without and g) result with density constraints for the background are on an identical scale as well. All values given in g/cm^3 .

As it was the case for the NMAE during the reconstruction, the final NMAE for the “no background, no noise” case is the lowest one of all cases. The errors for the “background, no noise” cases are comparatively higher, but can be improved by using density constraints. As inconsistencies in the Fe reconstruction are transferred into the background, the NMAE for the background results are higher than for the Fe density volumes. For the “noise” cases the NMAE is dominated by the noise, masking the influence of the density constraints and background inconsistencies on the error.

Multiple Elements (+Background)

The multi-element cases include the simulations for the combination of Ti-, Fe- and Zn-phantom without and with background as well as without and with noise. In contrast to the reconstruction of the single-element cases, no density constraints were needed for the multi-element reconstructions, as the increased spatial coverage of elements decreased the effective size of empty regions inside the sample and thus the influence of reconstruction artifacts in the primary beam absorption volumes. For each case, the full self-absorption corrected reconstructions required about 34.2 hours in computation time.

Figure 4.11 shows the development of the logarithmic percentual normalized mean absolute errors depending on the iteration calculated for the mass density volumes of the Ti-, Fe- and Zn- $K\alpha$ lines against the average mass density volumes of all lines belonging to each respective element. As the error curves for the multi-element “noise” cases follow an identical pattern as those for the single-element cases, approaching an equilibrium while the FMH prior is active and steadily increasing after, they are not shown to improve the clarity of the plot (see supp. fig. S2).

As it was the case for the single-element reconstructions, the reduction in downscaling factor at iteration 160, 250 and 290 causes a drop in the error corresponding to an improvement in self-absorption correction, while the FMH prior applied up to iteration 100 mainly has an influence on the “background” cases.

There are two properties of the error plot that have to be considered especially: The general difference in error between elements as well as the difference in error between the “no background” and “background” cases. Towards the later iterations, it can be seen that the error for the Zn reconstruction is larger than the error for the Ti reconstruction, which in turn is larger than the error for the Fe reconstruction. This is most likely caused by the choice of phantoms. The Fe-phantom consist of relatively coarse structures and homogeneous areas with less possibilities for inconsistencies to develop, while the Ti- and even more so the Zn-phantom show finer structures and more variation, allowing for increased differences and error between the $K\alpha$ - and $K\beta$ -reconstructions.

The difference in error between the “no background” and “background” cases depending on the element can be explained by considering the influence of inconsistencies in the background on the self-absorption correction of the element. As the absorption of the background approximately scales with a scaling law (eq. 4.9), lower energy XRF emission lines are influenced stronger by the background than higher energy XRF emission lines. Inconsistencies in the background therefore lead to a large difference in error between the “no background” and “background” case for the Ti reconstruction, which is reduced for the Fe reconstruction and even more for the Zn reconstruction, which is the least influenced by the background.

Figure 4.12 shows the results of the self-absorption correction reconstruction for the “background, noise” case for all elements and the background. Reconstructions for the “no background, noise” case can be found in supplementary figure S3. Strong self-absorption artifacts

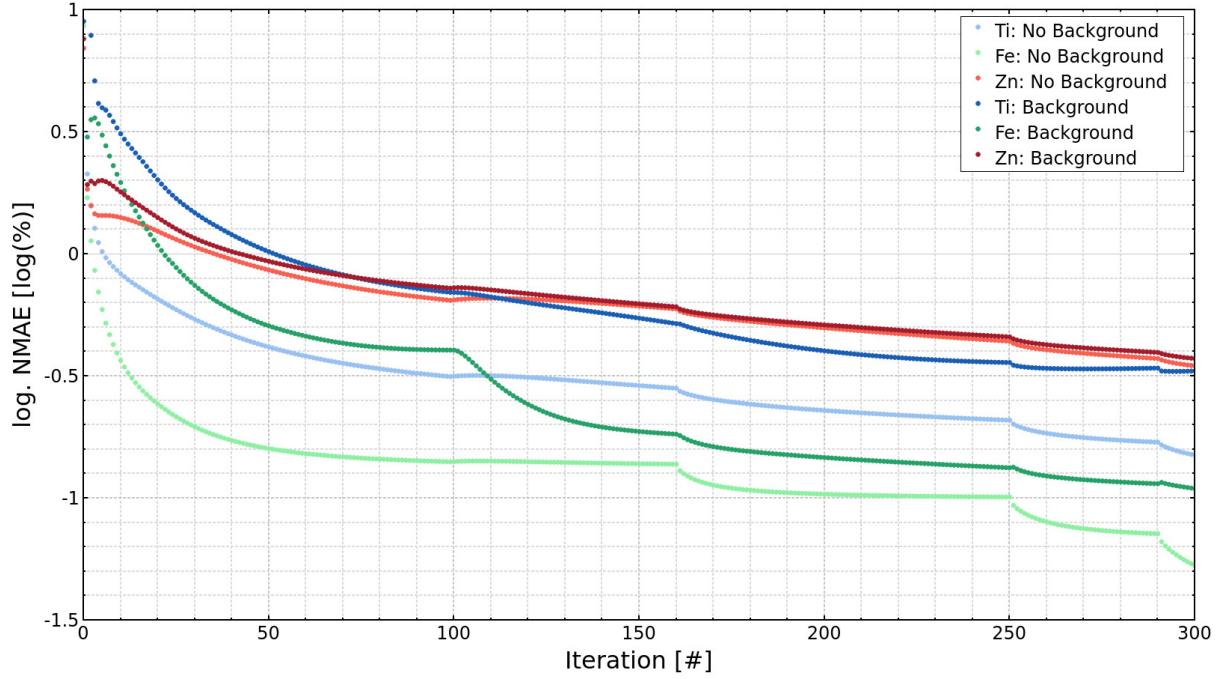


Figure 4.11: Logarithmic (\log_{10}) percentual normalized mean absolute errors (eq. 3.33) at different iterations for the noiseless multi-element simulations. Calculated is the error of the $K\alpha$ line reconstruction of an element compared against the average of all line reconstructions of the element.

are visible in the uncorrected elemental reconstructions, manifesting themselves as decreased densities towards the center of the reconstructions, “imprints” of other elements in regions of high self-absorption as well as intensity outside of the sample area, especially for the Zn reconstruction. These artifacts, qualitative and quantitative, are almost completely mitigated in the corrected reconstructions. The remaining main cause of differences between corrected reconstructions and ground truths is the applied Poisson noise.

As it was the case for the single-element reconstruction, the background shows “imprint artifacts” caused by inconsistencies as well as noise in the elemental reconstructions and leading to further inconsistencies in the algorithm.

In Table 4.3 the final normalized mean absolute errors of the reconstructed elemental density distributions and background volumes calculated against their noiseless ground truths are shown.

Table 4.3: Normalized mean absolute errors (eq. 3.33) of the reconstructed multi-element simulations calculated against their noiseless ground truths.

NMAE(recon., truth)	Ti	Fe	Zn	Background
No Background	0.0109	0.0051	0.0210	-
Background	0.0187	0.0075	0.0218	0.4795
No Background, Noise	0.0605	0.0438	0.0618	-
Background, Noise	0.0982	0.0547	0.0660	0.9616

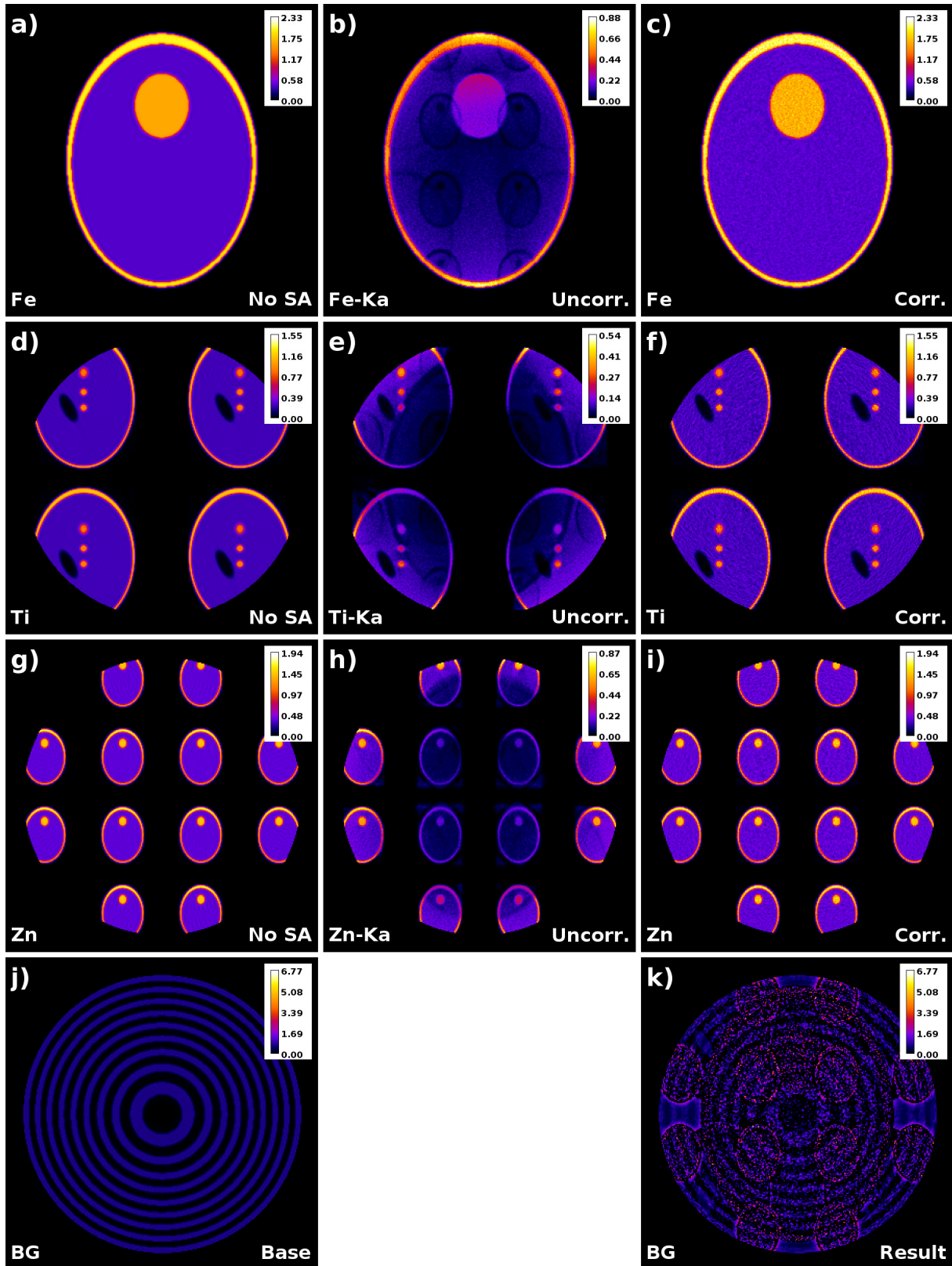


Figure 4.12: Ground truth, uncorrected ($K\alpha$) and corrected reconstruction of a-c) Fe, d-f) Ti and g-i) Zn for the noisy multi-element simulation with background. For comparability reasons ground truth and corrected reconstruction are on an identical scale, while the uncorrected reconstruction is scaled separately for visibility. The j) ground truth and k) result for the background are on an identical scale as well. All values given in g/cm^3 .

For the noiseless cases, the overall error of the Fe reconstruction is the lowest, followed by the error of the Ti and then the error of the Zn reconstruction. This is consistent with the general behavior of the NMAE during the iterations. It has to be mentioned that the complexity of the self-absorption correction increases as more elements are considered for the multi-element cases, leading to larger errors in the Fe reconstruction compared to the single-element cases (see tab. 4.2).

For the cases with added noise, the NMAE increase significantly as the errors caused by the noise exceed any errors caused by other inconsistencies in the self-absorption correction algorithm. Furthermore, the NMAE of the Ti reconstruction increases relative to the NMAE of the Zn reconstruction and even surpasses it in the “background, noise” case. This is caused by the higher influence of inconsistencies caused by the noise and inconsistencies in the background on the self-absorption calculations for the lower energy Ti-K α emission line.

The NMAE of the resulting background volumes for the “background” cases are higher than the NMAE of the elemental reconstructions as the background volumes are not additionally constrained by measured sinograms and therefore accumulate inconsistencies in the elemental reconstructions.

Chapter 5

Synchrotron Experiments

5.1 Setup

All experiments were performed at beamline P06 of the PETRA III synchrotron storage ring at DESY in Hamburg, Germany. P06 is a hard X-ray beamline specialized for X-ray microscopy and imaging techniques, like for example X-ray fluorescence (XRF) microscopy, scanning transmission X-ray microscopy (STXM) and X-ray ptychography. To facilitate high resolution measurements, the beamline provides focus sizes in the range from micro- to nanometers.

5.1.1 PETRA III Beamline P06

Beamline P06 (fig 5.1 a) consists of three main parts: An undulator that acts as insertion device, an optics hutch to modify the X-ray beam and an experimental hutch, in which the experiments are performed. The experimental hutch is further divided into a Micro- and a Nanoprobe. In addition, a part of the beamline close to the experimental hutch is reserved for experimental control. At different positions along the entire length of the beamline, multiple beam position monitors and retractable screens are used to observe the X-ray beam and monitor its quality while it is modified by different optical elements. Starting from the insertion device up to the experimental hutch, the beam path is in vacuum to reduce attenuation by air molecules.

Insertion Device

The insertion device located at the beginning of P06 is a 2 m U32 spectroscopy undulator with a magnet period of $\lambda_U = 31.4$ mm and a maximum undulator parameter of $K_{max} = 2.7$ [SBF⁺10]. It generates linearly polarized X-rays and has its first harmonic at an energy of 2.4 keV. The source size and the beam divergence of the undulator at 12 keV are about $36 \times 6 \mu\text{m}^2 \sigma$ and $28 \times 4 \mu\text{rad}^2 \sigma$, respectively.

To narrow down and shape the size of the X-ray beam before it enters the optics hutch, a vertical high-power slit (PS1) and one in both vertical and horizontal direction (PS2) are placed downstream of the undulator [SBD⁺16].

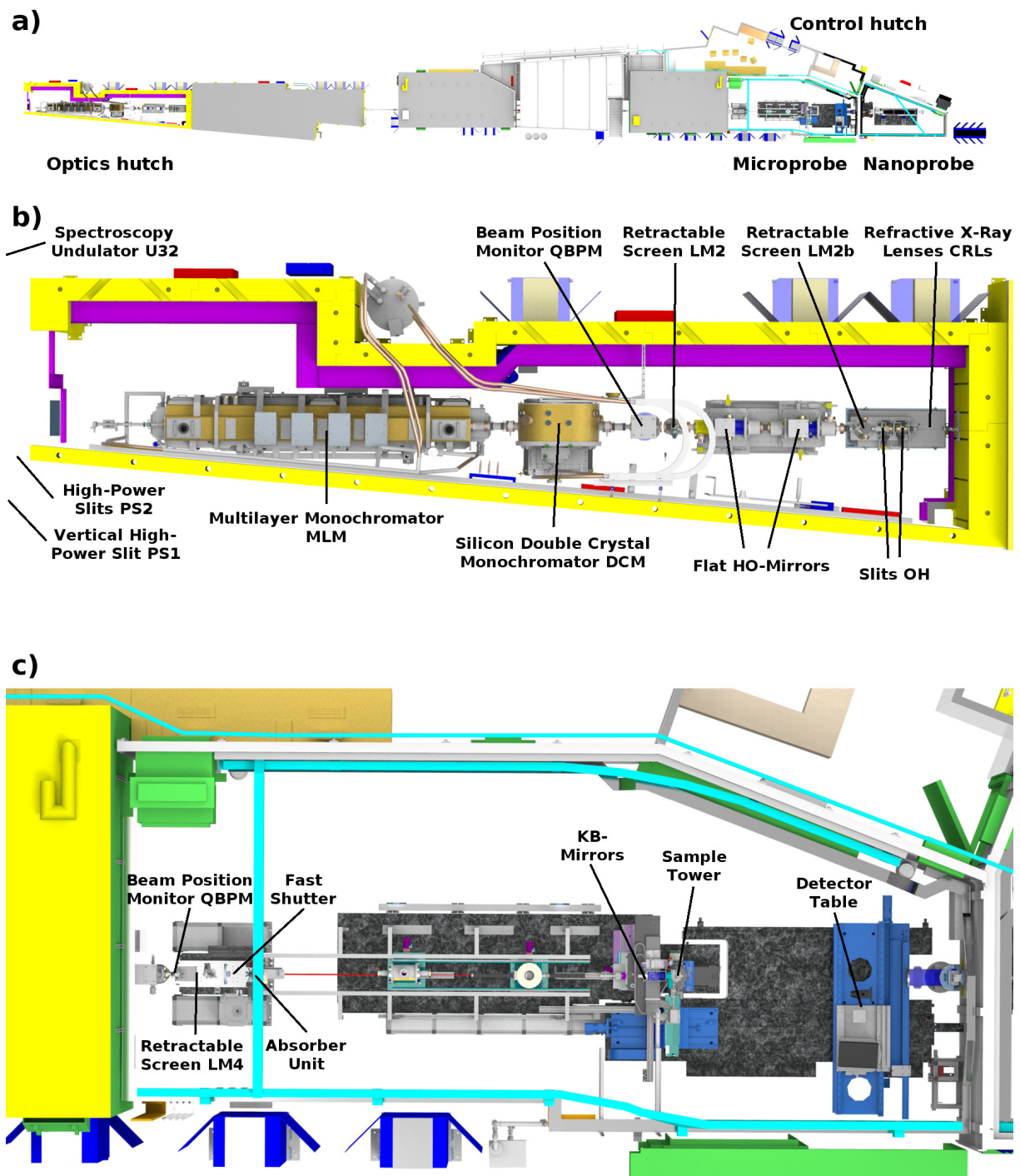


Figure 5.1: Schematic overview of a) the beamline P06 without insertion device, b) the P06 optics hutch and c) the P06 Microprobe. Rendered images courtesy of Hendrik Lindemann.

Optics Hutch

The entrance of the optics hutch is located 31.5 m downstream of the insertion device and its length measures 11.8 m. It contains multiple optical elements to modify the X-ray beam parameters to the specifications required by the experiment. A schematic plan of the optics hutch is shown in figure 5.1 b).

Two different types of monochromators are available to monochromatize the X-ray beam: A multilayer monochromator (MLM) and a silicon double crystal monochromator (DCM). The DCM is further divided into two parts, with the first being a pair of Si 111 crystals usable in the energy range from 3 keV to 50 keV and the second being a high-stability Si 111 channel-cut crystal usable in the range from 6 keV to 18 keV. To ensure a constant 22 mm vertical offset and a less complicated alignment of the beamline, the Si 111 crystals are placed in a fixed-exit geometry.

On the other hand, the MLM consists of two flat mirrors, with one coated with PdB₄ and the other with NiC. It is usable in the energy range from 10 keV to 100 keV and offers increased photon flux in exchange for a worse energy bandwidth.

Downstream of the monochromators, two flat HO-mirrors can be used for higher-harmonics rejection. To enable a variety of cut-off energies with multiple incidence angles, different areas of the mirrors are coated with one of the three materials platinum, chromium or silicon. For example, assuming an incidence angle of 2.5 mrad, the cut-off energies of the HO-mirrors are 30 keV for the platinum, 20 keV for the chromium and 12 keV for the silicon.

Placed close to the exit of the optics hutch are horizontal and vertical slits to further confine the beam as well as profocusing sections containing 1D nanofocusing lenses (NFLs) and 2D compound refractive lenses (CRLs). These lenses may either be used to prefocus the beam and increase the photon flux at the experiment or, for methods that require high coherence, to defocus the beam.

Microprobe

The Microprobe is the first of the two parts of the experimental hutch and shown in 5.1 c). Its entrance is located 86 m downstream of the insertion device.

Placed at the beginning of the Microprobe is a beam diagnostics section consisting of a quadrant beam position monitor (QBPM) and a retractable screen. Located a small distance downstream of the beam diagnostics is a fast shutter as well as an absorber unit. The absorber unit contains sheets of Al and Si in varying thickness to attenuate the X-ray beam if necessary. An evacuated flight tube assures minimal air absorption of the beam up to the experiment.

One of the possible optical elements of P06 used to focus the X-ray beam is a KB-mirror system. A slit system at the entrance of the KB-system assures an ideal beam size for the aperture of the KB-mirrors, while an ion chamber measures the incident flux for normalization purposes. The KB-mirrors themselves are a pair of Rh-coated Si mirrors with fixed elliptical shapes. They are placed inside a containment box flushed with N₂ to prevent degradation caused by the X-ray

beam, for example carbon deposition. With an incident angle of 2.5 mrad, the KB-mirrors have a working distance of 200 mm and a cut-off energy of 23 keV [Fal15]. To use other focusing optics, for example CRLs, the KB-mirror system can be moved to the side and out of the beam. Downstream of the KB-mirror system is an open space to assemble the sample tower consisting of scanning stages and sample mounts as required for the experiments. A movable table provides room to mount multiple different detector systems.

Finally, the Microprobe exits into the Nanoprobe, which contains a nanofocusing X-ray microscope used to measure samples too small for the larger foci of the Microprobe optics.

5.1.2 P06 Tomography Setup

One of the possible configurations of the sample tower is the P06 tomography setup as shown in figure 5.2. For stability reasons and to dampen vibrations, the entire setup is placed on top of a heavy granite block.

A sample hexapod (Newport HXP200S-MECA) with a minimum incremental motion of 0.15 μm acts as base of the setup and allows for coarse translation and tilting of the sample. On top, an air-bearing rotation stage (PiMicos UPR-270 Air) rotates the sample, which is essential for tomography experiments. The rotation stage has an angular accuracy of 0.97 arcsec, which is equivalent to about 4.7 μrad . Centering stages (Huber 5101.07 Linear Stage) in x - and y -direction and with an accuracy of 6 μm are used to align the sample to the center-of-rotation. Finally, piezo scanners in x - and y -direction (Aerotech QNP60XY-500) as well as in z -direction (Aerotech QNP60Z-500) allow for fine translation of the sample with resolutions <1 nm and fast scanning. Depending on the size and shape of the sample, special sample mounts may be required for the sample to reach the height of the X-ray beam.

5.1.3 Detectors

For STXM and XRF tomography experiments, two types of detectors are essential: A detector downstream of the sample to measure the transmission of the primary beam through the sample as well as spectrally resolved detectors to detect the emitted XRF signal.

At P06, STXM measurements are usually performed using a Canberra PD300-500CB Passivated Implanted Planar Silicon (PIPS) diode. The X-rays hitting the diode are absorbed and excite electron-hole pairs in the diode material. As the diode is connected to a voltage, this causes an electric current to flow. On the condition that the diode is used in its linear range, this current is proportional to the amount of excited electron-hole pairs, which is itself proportional to the X-ray intensity. Connected to the PIPS diode is a Keithley picoammeter to accurately measure the electric current at the diode. Variable gain settings allow to cover a large range of electric currents and thus X-ray intensities. As STXM is a relative measurement mode, it is not necessary to quantitatively determine the intensity of the X-ray beam and thus the exact calibration of the diode is of less importance than it would be, for example, for XRF detectors.

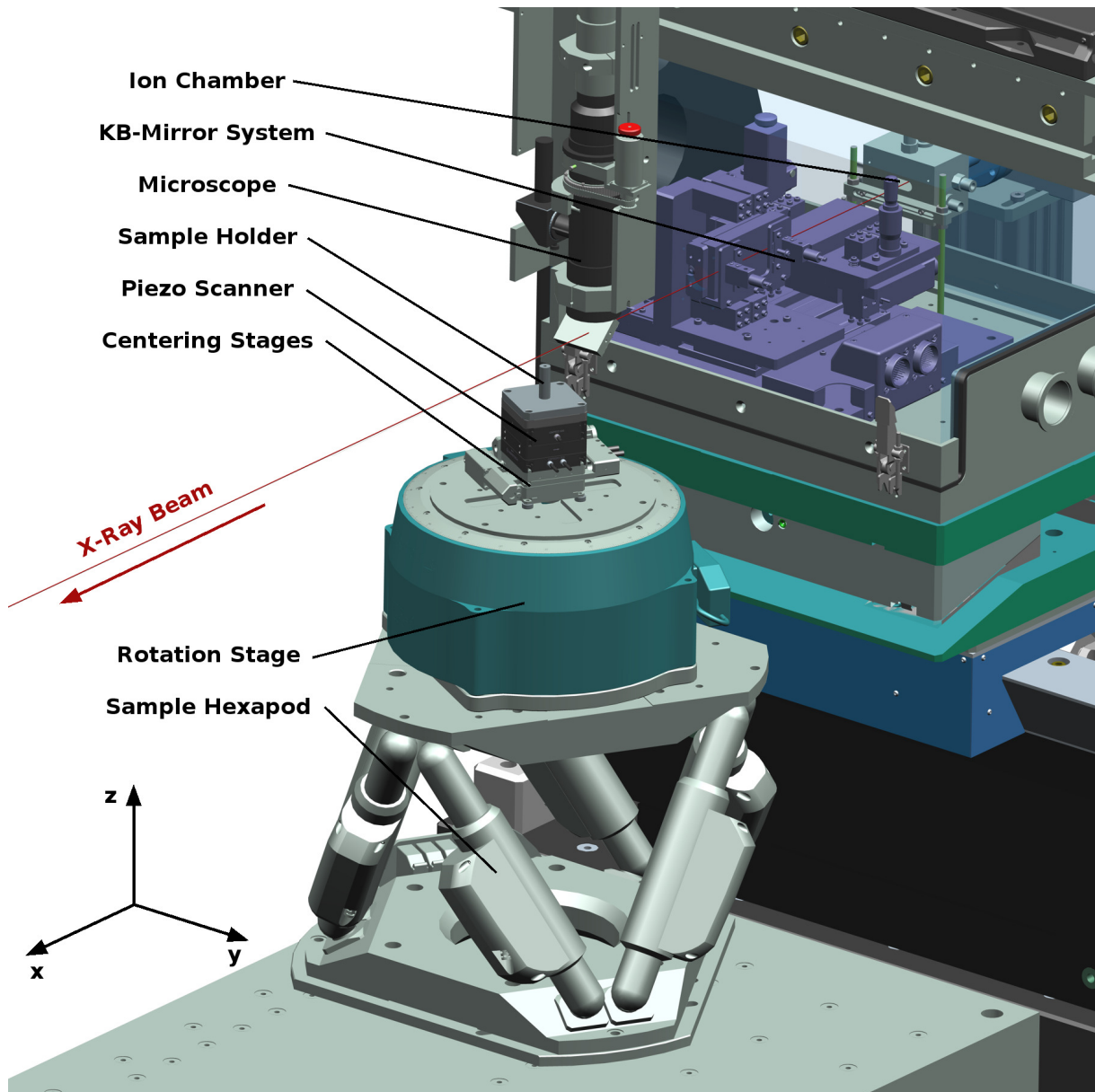


Figure 5.2: Rendering of the P06 tomography setup, including KB-mirror system. Rendered image courtesy of Vanessa Galbierz.

Among others, the XRF detectors used at P06 include two Hitachi Vortex-EM silicon drift detectors (SDD). For both Vortex detectors, the detector material is a silicon crystal with a nominal active area of 50 mm^2 and a nominal thickness of $350 \mu\text{m}$. Beryllium windows with a thickness of $12.5 \mu\text{m}$ secure the vacuum inside the detectors and protect the silicon crystals from environmental influences. An SDD consists of concentric rings of p+ silicon and a small central n+ signal anode on an n-type silicon chip, designed to generate an electric field gradient [PPK⁺14]. This electric field causes the electrons created by X-rays to drift to the anode, where the resulting electric current is converted into a voltage signal using field-effect transistors. The increase in voltage signal is proportional to the energy of the X-rays.

To analyze the voltage signal of an SDD and create energy dependent XRF spectra, pulse processors are used. At P06, these are Xspress3 pulse processors developed by Quantum Detectors.

The Xspress3 pulse processor features output rates of more than 3.4 Mcps and deadtimes below 100 ns per event. Furthermore, the system automatically optimizes internal parameters like the shaping or peaking times depending on the measured sample. However, as the exact method of optimization is a company secret, this also complicates the correction of deadtime and pile-up effects by preventing the use of an accurate model.

5.2 Experiment

The performed experiment consists of tomographic STXM and XRF measurements of a micrometeorite sample as well as XRF measurements of elemental calibration foils. The measurements were conducted by Dennis Brückner, with the aid of Dr. Stijn Van Malderen (formerly Ghent University) and Dr. Ir. Jan Garrevoet (DESY).

5.2.1 Samples

Each year, around 30000 tons of extraterrestrial material enter Earth's atmosphere, with about 5% of it reaching the surface of the planet, while the remaining mass is lost due to processes like melting and evaporation [PRdAK18]. Most of this material comes in form of micrometeorites, extraterrestrial dust particles with sizes reaching from about 10 μm up to 2 mm [FC15]. The properties of a micrometeorite, like shape and elemental composition, are dependent on the nature of its parent body, the type of process leading to its creation as well as the conditions during its deceleration in Earth's atmosphere. Investigating the properties of micrometeorites can thus lead to information about the physics and chemistry of extraterrestrial objects.

Found in a sedimentary record from the Atacama Desert and provided by Dr. Jenny Feige (TU Berlin), the micrometeorite examined during this experiment is approximately spherical in shape and has a size of about 150 μm . Using the system established by Genge *et al.* [GEGT08], it can be classified as a melted micrometeorite, specifically as a silicate-type cosmic spherule with the barred olivine subtype. Barred olivine micrometeorites are defined by parallel growths of skeletal olivine, $(\text{Mg}^{+2}, \text{Fe}^{+2})_2\text{SiO}_4$, inside a glassy mesostasis. Other elements of interest may include, for example, Al, Ca, Ti, Cr, Mn, Ni as well as Sr [PRdAK18].

During XRF tomography, the high elemental concentrations in micrometeorites can lead to strong self-absorption effects. Furthermore, the part of the absorption caused by the low-Z glassy background is large enough to not be negligible for the purpose of self-absorption correction, yet small enough that it would not be feasible to assume a trace-element approximation for all other elements. This increases the necessity for accurate experimental calibration to be able to correctly separate elemental signal from background. Therefore, micrometeorites can be considered as challenging samples for any XRF tomography experiment and self-absorption correction algorithm.

5.2.2 Measurements

All measurements were performed at a primary beam energy of 18 keV with the DCM as monochromator. Edge measurements using a gold cross determined the full width at half maximum (FWHM) size of the KB focus to be ca. 400 nm in horizontal and ca. 350 nm in vertical direction. An ion chamber located upstream of the KB mirrors was used to detect intensity fluctuations in the primary beam. XRF detection was performed using a dual Vortex setup, with one detector placed at 90° relative to the primary beam direction and the other at 270°

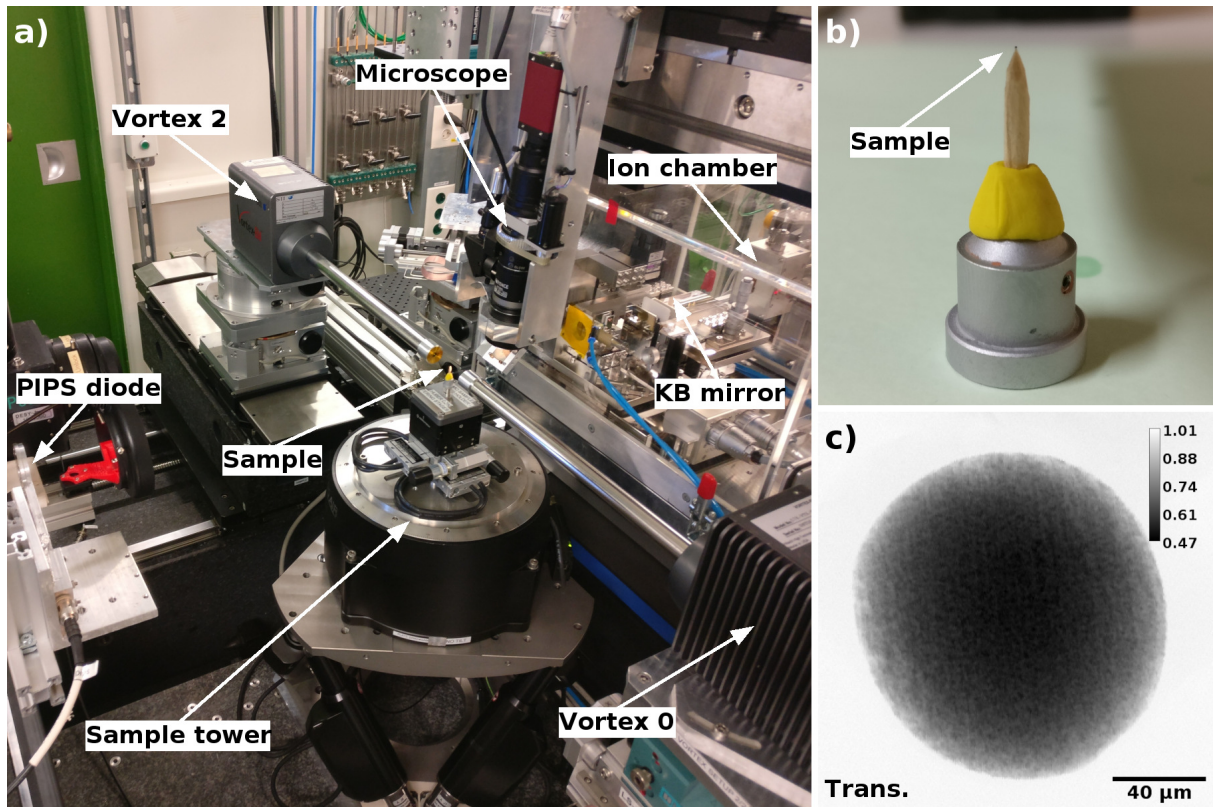


Figure 5.3: a) Overview image of the experiment at P06. b) Closer view of the sample mount with the micrometeorite sample. c) Normalized transmission image of the micrometeorite measured under an angle of 0° and cropped to a size of 340×340 pixel ($z \times y$).

(fig. 5.3 a). Both detectors were covered with a $13 \mu\text{m}$ polyimide window glued onto a 6 mm diameter collimator and the air paths between sample and detectors measured 30 mm. The sample was mounted economically and sustainably on a toothpick stabilized with clay, using nail polish remover as glue (fig. 5.3 b). A PIPS diode was placed 450 mm downstream of the sample to measure transmission data (fig. 5.3 c).

The tomographic sample measurement was performed in fly-scanning mode using an initial grid of 340×380 ($z \times y$) positions per projection with 500 nm effective step size and 2.75 ms effective dwell time per scan point. For the tomogram, 362 angles were recorded in two 181 angle batches, with the first batch covering the angular range from 0° to 180° and the second batch from 180.5° to 360.5° , using 1° angular steps for both batches. In total, the required time to measure the complete tomogram amounted to about 39.1 hours. To limit the amount of XRF photons to be consistent with the specifications of the Vortex detector and Xspress3 pulse processor, the incident primary beam was attenuated to 50% of its initial flux.

The elemental calibration of the experiment was determined by measuring Fe, Ni, Cr and Cu calibration foils. To stay consistent with the tomographic measurement, the foils were measured in fly-scanning mode and the dwell time of the calibration measurements was kept at 2.75 ms. However, the step size was increased to $1 \mu\text{m}$ to cover a larger foil area and to be able to obtain an improved average value for the calibration factor. All foils were measured under two angles, $\pm 45^\circ$ from normal incidence, with each angle being rotated towards one of the Vortex detectors.

Chapter 6

Experimental Results

6.1 Data Processing

The data processing preceding the tomographic reconstruction can be divided into three steps: First the fitting of the XRF spectra, followed by the deadtime and pile-up correction and finally the sorting of the data into an image. Furthermore, it is necessary to calculate the calibration factors from the measurements of the calibration foils.

6.1.1 XRF Fitting

The fitting of the XRF spectra was performed using the PyMca toolkit developed at the European Synchrotron Radiation Facility [SPC⁺07]. First, the graphical interface of the toolkit was used to identify the main elements of the sample in the sum spectrum of an entire projection. Following that, fit parameters, for example the detector energy calibration and resolution, were determined from a subset of these spectra. This allows for an improved description of the characteristics of the single spectra. Finally, each single spectrum was individually fitted using a custom script based on the PyMca fitting methods, which was developed by Dr. Stijn Van Malderen and is maintained by Dr. Ir. Jan Garrevoet. As the counting statistics in the single spectra were low, it was not possible to fit $K\alpha$ and $K\beta$ lines separately without introducing strong noise into the data. Therefore, the single spectra were fitted assuming a fixed $K\alpha:K\beta$ intensity ratio.

Figure 6.1 shows the logarithmic sum spectrum of the first tomographic projection for detector 0 up to an energy of 25 keV. Written above the peaks are the possible elements or combinations of elements they could be made up of. It can be seen that the spectrum is mainly dominated by the high intensity Fe-signal with smaller contributions from the Mn- and Ni-signals. These high intensity signals cause an extended pile-up area in the region around 13 keV, thus complicating the creation of a suitable fit by possibly masking other lower intensity elemental signals. This is especially the case because the description of pile-up in PyMca is lacking, as the formation of pile-up is highly dependent on the utilized detector and detector electronics.

Another important feature of the spectrum are the escape peaks. They are caused by exciting

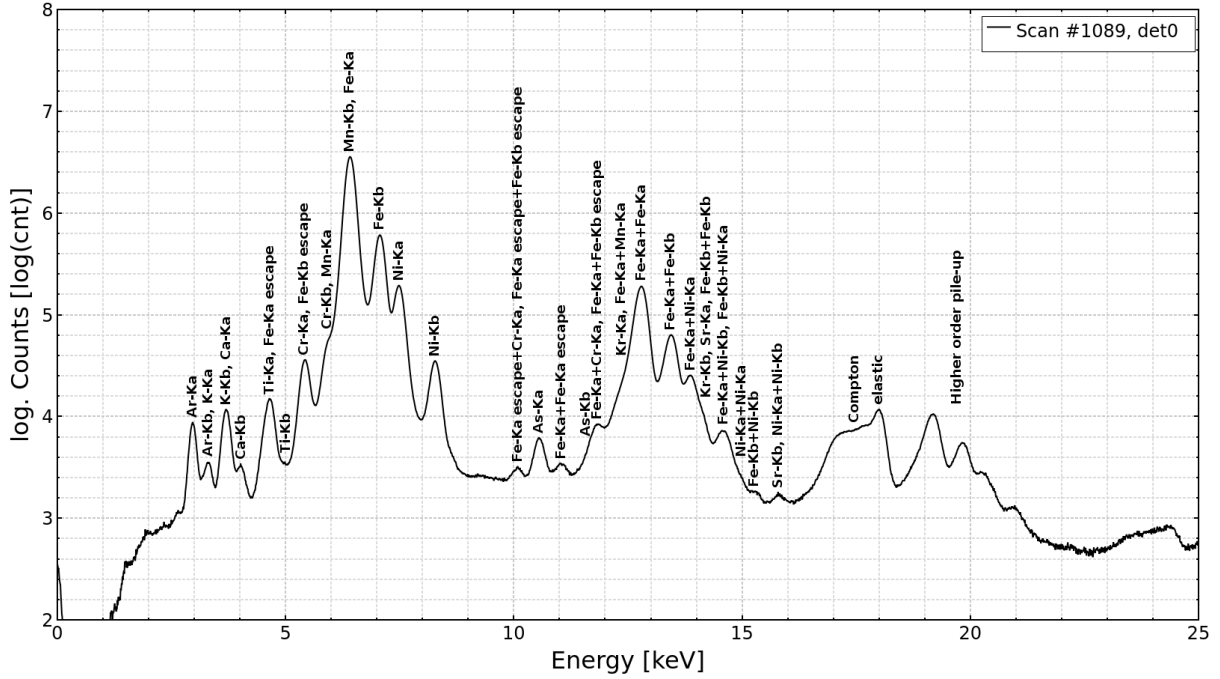


Figure 6.1: Sum spectrum of the first tomographic projection for detector 0 with possible elements or elemental combinations written above their corresponding peaks. The counts are given as \log_{10} to improve the visibility of the low intensity peaks.

X-ray fluorescence of the detector material, which may then escape the detector. This leads to peaks with a measured energy which is effectively lowered by the energy of the escaped XRF photon. For silicon $K\alpha$ XRF this energy amounts to about 1.74 keV. In contrast to the correction of the deadtime losses and pile-up peaks, which may require sophisticated models, escape peaks are accounted for by adding their integral density to their corresponding main XRF emission peak.

6.1.2 Deadtime and Pile-Up Correction

To calculate the parameters for the deadtime and pile-up corrections, a Mn-foil was measured. The measurements, conducted by Dennis Brückner and Dr. Gerald Falkenberg (DESY), were performed at a primary beam energy of 7 keV by scanning the slits upstream of the sample and varying the detector-sample distance. Three example spectra of these measurements are plotted in figure 3.1. An ion chamber between slits and sample was used to quantify the photon flux of the incident beam I_0 and data points falling inside the non-linear regions of the ion chamber were discarded.

After integration of the spectra, the measurements for the different detector distances were combined by rescaling their respective I_0 -values to a common scale to define the relation between the detected count rate and the incident photon flux $\text{OCR}(I_0)$. Fitting the low-intensity region of this dataset, in which the relation between OCR and ICR should be close to linear, with a linear function then allows to recalibrate the I_0 -axis into an ICR-axis to define the relation between input and output count rates $\text{OCR}(\text{ICR})$.

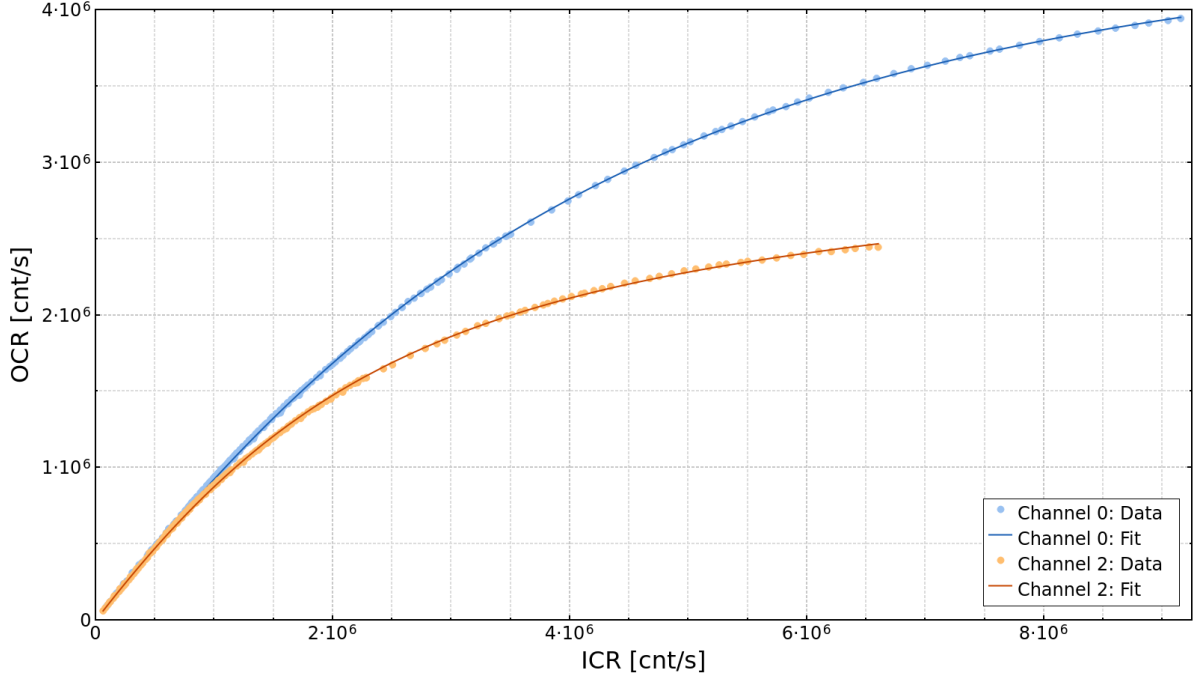


Figure 6.2: Plot and fit (eq. 3.8) of the OCR over ICR data that was recorded using Mn-foils. The fit parameters for both detectors can be found in supplementary table S1.

Figure 6.2 shows the resulting OCR over ICR plots for both detectors fitted with the deadtime and pile-up model described in equation 3.8. It can be seen that the fit is consistent with the data. However, as the model only considers 2-event pile-up but the experimental data shows even higher order pile-up (compare fig. 6.1), the exact physical meanings of the fit parameters are lost. The fit parameters are then used to create a lookup table correlating OCR to ICR.

There are two different methods to correct for deadtime effects: The first one is to apply the correction factor calculated from the lookup table to every bin of the unfitted spectra. Alternatively, as the correction is multiplicative, it is also possible to first fit the spectra and then apply the correction factor to the fitted value of each peak. This second method requires less computational operations as well as memory space and was therefore used for the data processing.

To correct the effects of the pile-up, the inverse pile-up loss $\lambda_{pu} \geq 1$ depending on the ICR was calculated by comparing the sum of the areas of the different n -event pile-up regions $I_{pu,n}$ in the Mn-spectra to the area of the single-event region $I_{pu,1}$:

$$\lambda_{pu}(ICR) = \frac{\sum_n n I_{pu,n}(ICR)}{I_{pu,1}(ICR)} \quad (6.1)$$

The resulting inverse pile-up loss shows approximately a linear dependency on the ICR (see supp. fig. S4) with a slope of m_{pu} :

$$\lambda_{pu} = m_{pu} \cdot ICR + 1 \quad (6.2)$$

After determining the slope describing the linear dependency (see supp. tab. S1), the pile-up correction was applied to the fitted value of each peak similar to the deadtime correction.

6.1.3 Sorting

As the experimental X-ray fluorescence data was recorded in fly-scanning mode, it had to be sorted into an image grid using the encoder positions of the scanning stages. This sorting was performed using a custom script developed by Dr. Stijn Van Malderen and maintained by Dr. Ir. Jan Garrevoet. Interpolation was performed using the nearest-neighbor scheme, to be able to detect and correct missing points for the rare cases in which the XRF fitting failed because of low counting statistics.

The normalization to the incident photon flux I_0 was performed by dividing the sorted XRF images with the values measured by the ion chamber upstream of the KB-mirror system. To maintain consistency between the XRF and the I_0 dataset, the ion chamber data was sorted into images utilizing the same parameters that were used for the sorting of the X-ray fluorescence data beforehand.

Figure 6.3 shows images of the normalized count rate for different elemental $K\alpha$ lines measured using Vortex detector 0. Self-absorption effects are visible as shadowing towards lower y -coordinates, which is consistent with the placement of detector 0 at high y -coordinates.

6.1.4 Calibration

To quantify the measured data and correct for self-absorption effects, accurate elemental calibration is required. There are three parts that have to be considered to calculate the calibration: The amount of emitted XRF photons from the sample including self-absorption effects, the attenuation of the XRF photons along the path to the detector as well as the fraction of XRF photons that are absorbed in the detector material.

Figure 6.4 shows the energy-dependent efficiency of an XRF detector system:

$$\text{Efficiency} = \frac{\text{Photons absorbed in the detector}}{\text{Photons emitted by the sample}} \quad (6.3)$$

calculated using the parameters for the Vortex detector and experimental geometry as described in the experimental chapter. The plotted efficiency does not include any deadtime effects. It can be seen that the transmitted fraction of XRF photons along the path to the detector is small at low energies, but increases at higher energies as the absorption decreases. Conversely, the fraction of XRF photons absorbed in the detector material is high at low energies, but decreases at higher energies as some photons begin to pass through the detector without being absorbed. In total, both of these effects result in an efficiency function with a maximum around an energy of 8.3 keV, falling off towards lower as well as higher energies.

While the efficiency of the detectors was calculated analytically, the amount of emitted XRF photons from the sample was determined by measuring elemental calibration foils (supp. tab. S2). It was assumed that the foils are thin enough that any self-absorption effects are negligible. After the foil measurements, the calibration data was fitted, corrected for deadtime and pile-up as well as sorted into images in the same way as the micrometeorite data.

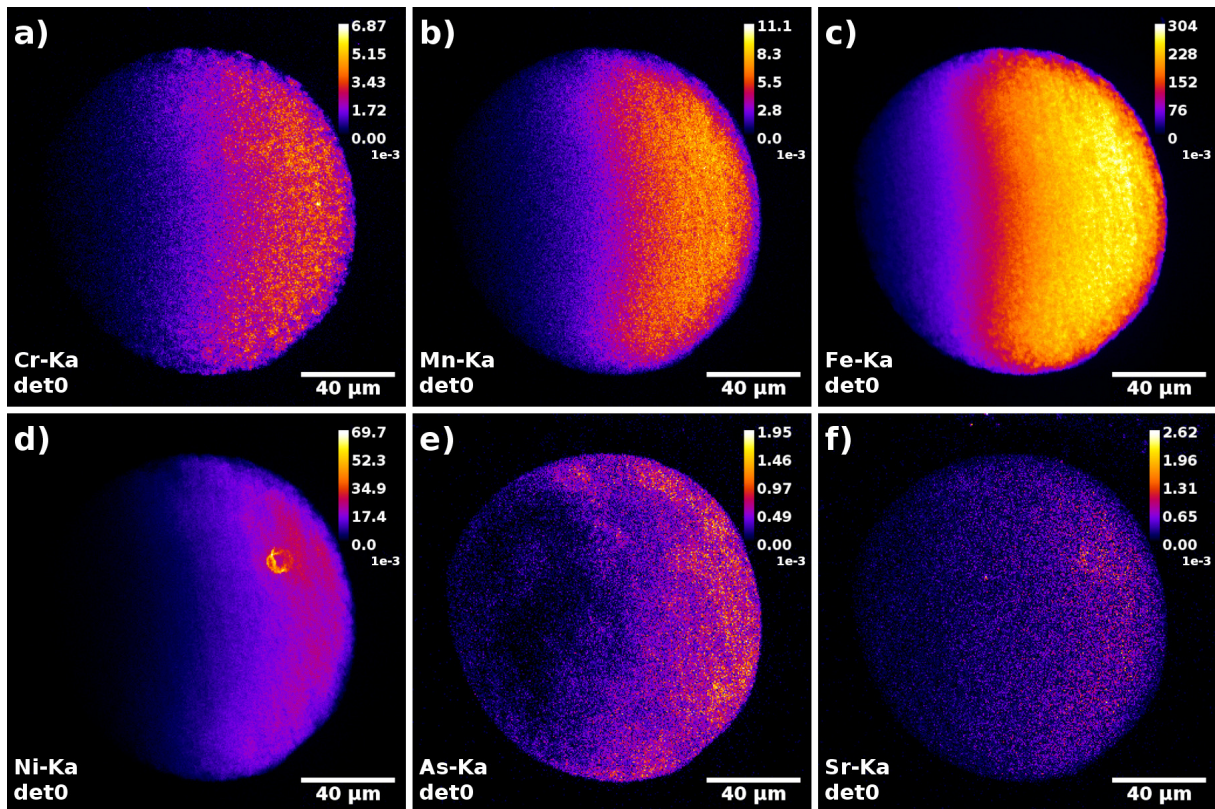


Figure 6.3: XRF projection for a) Cr, b) Mn, c) Fe, d) Ni, e) As as well as f) Sr using Vortex detector 0 and recorded under 0° . The given values are the corrected measured counts normalized to the incident photon flux (note the factor of 10^{-3}).

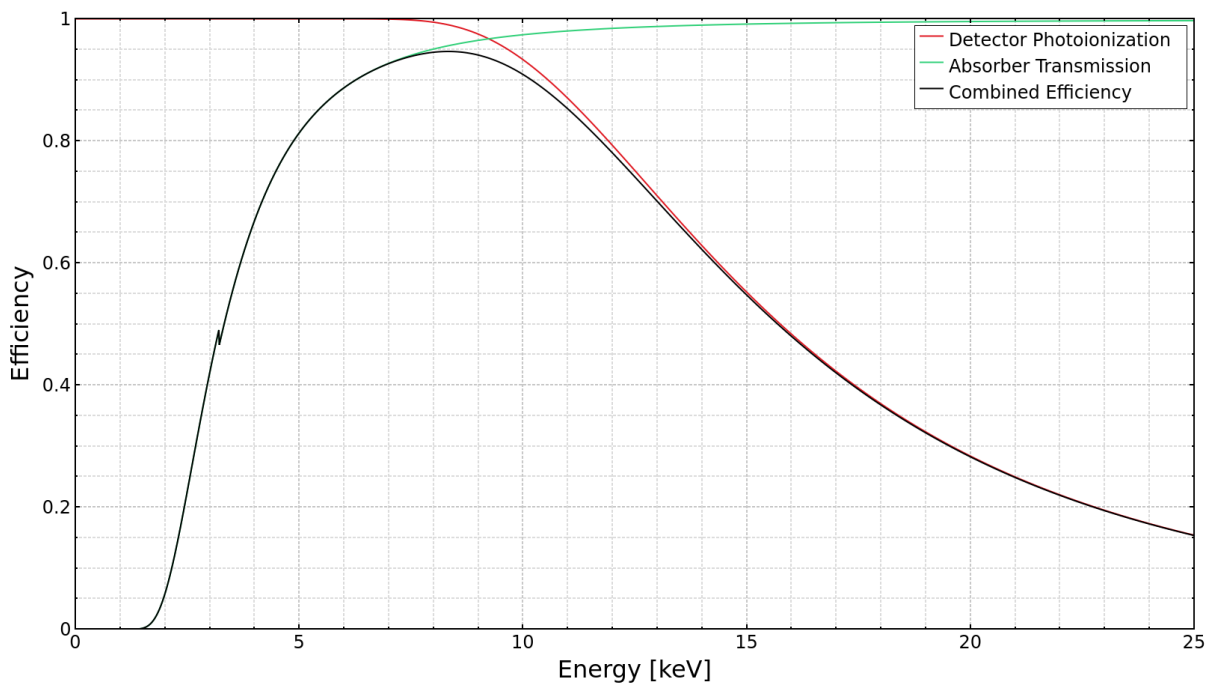


Figure 6.4: Energy-dependent detection efficiency of a 350 μm Si Vortex-EM XRF detector. The red line shows the efficiency of the photoionization in the detector material, while the green line shows the transmission through the absorber material between detector and sample (12 μm Be, 13 μm Kapton and 30 mm air). The black line shows the resulting combined efficiency.

The normalized count rate $\hat{R}_{L,d}$ of XRF line L measured at the detector can be calculated as the ratio of the count rate $R_{L,d}$ measured at the detector and the incident count rate R_0 measured at ion chamber:

$$\hat{R}_{L,d} = \frac{R_{L,d}}{R_0} = \frac{I_{L,d}}{I_0} \quad (6.4)$$

or alternatively, with the dwell time being constant between the two datasets, as the ratio of the intensity $I_{L,d}$ measured at the detector and the intensity I_0 measured at the ion chamber.

Using the transmission values T_m for the different materials m along the path to the detector as well as the value for the photoionization attenuation A_d inside the detector material, all at line energy E_L , the normalized count rate $\hat{R}_{L,s}$ at the sample position can be calculated as:

$$\hat{R}_{L,s} = \frac{\hat{R}_{L,d}}{\prod_m T_m(E_L) \cdot A_d(E_L)} \quad (6.5)$$

In cases in which L consists of the sum of multiple lines, for example if the $K\alpha$ line cannot be energetically resolved into the $K\alpha_1$ and $K\alpha_2$ line, the energy for the most intense line is used in the calculations.

Following that, the normalized count rates at the sample position are divided by the given area mass densities $\rho_{2D,Z}$ of their corresponding elemental calibration foils, where Z indicates the element. It is important to mention that the tilt of $\pm 45^\circ$, under which the calibration foils were measured, leads to an increase of the projected area mass densities by a factor of $\sqrt{2}$. This ratio is then proportional to the X-ray fluorescence production cross-section $\sigma_{xrf,L}$ for line L at the primary beam energy E_0 :

$$\frac{\hat{R}_{L,s}}{\rho_{2D,Z}} = C_{cal} \cdot \frac{N_A}{M_L} \sigma_{xrf,L}(E_0) \quad (6.6)$$

with C_{cal} being an experiment specific calibration constant, N_A the Avogadro constant and M_L the molar mass of the element that emits line L .

Performing linear fits using the values calculated from the calibration foil measurements (supp. tab. S3) allows to determine the calibration constants as $C_{cal}^{det0} \approx 5.753$ for detector 0 and $C_{cal}^{det2} \approx 5.423$ for detector 2.

Using this calibration constant, the calibration factor $P_{cal,L}$ for any XRF line L can then be determined by calculating the ratio of the normalized count rate at the sample position and the area mass density for the line, propagating the ratio back to the detector and inverting it:

$$P_{cal,L} = \frac{\rho_{2D,Z}}{\hat{R}_{L,d}} = \left(C_{cal} \cdot \frac{N_A}{M_L} \sigma_{xrf,L}(E_0) \cdot \prod_m T_m(E_L) \cdot A_d(E_L) \right)^{-1} \quad (6.7)$$

Finally, these calibration factors are used in equation 4.23 of the tomographic self-absorption correction algorithm.

6.2 Tomographic Reconstruction

Reconstructing the tomographic dataset consists of two subsequent steps: First, the data has to be aligned to correct for any motion artifacts during the experimental measurements. Second, the tomographic reconstruction has to be performed considering the experimental parameters determined before.

6.2.1 Data Alignment

Before the tomograms were reconstructed, the projections had to be aligned and the rotation axis had to be defined. The absorption signal was used for the data alignment, as it usually has a superior signal-to-noise ratio compared to the XRF signals, is mostly independent from specific elemental distributions and does not suffer from self-absorption effects. After that, all determined correction factors were applied to the remaining XRF datasets.

To allow for sub-pixel correction, the projections were scaled up by a factor of two before the alignment procedure. Bilinear interpolation was used to avoid negative values. After the alignment and before the tomographic reconstruction, the projections were downscaled again to their initial size.

The first alignment step is the vertical alignment in z -direction. This was done by calculating the sums in horizontal y -direction for every projection and then minimizing the cross-correlation between the resulting line profiles. Figure 6.5 a) shows the line profiles for every projection before and after aligning by cross-correlation. While the maximum vertical difference for the unaligned case amounts to about 20 scaled pixel or 5 μm , this difference is reduced to a low single-digit pixel value after the alignment.

The second, and more complicated, alignment step is the horizontal alignment in y -direction. There are different methods for horizontal alignment, for example by calculating and aligning the center-of-mass of all projections [GSDH⁺11] or by assuring that the angular trajectory of different markers in the projections follow sine-functions [CCC⁺14]. Here, the horizontal alignment was performed using the concept of tomographic consistency. This concept is based on the idea that the Radon transform of a reconstructed tomographic slice should be identical to the initial sinogram. First, one of the measured absorption sinograms was reconstructed into a tomographic slice using filtered backprojection and after that immediately projected back into a simulated sinogram. Following that, the different angular projections of the measured sinogram were aligned to those of the simulated sinogram by minimizing their cross-correlation. These two steps were performed iteratively, until convergence. The results of the horizontal alignment are shown in figure 6.5 b). It can be seen that the unaligned reconstruction suffers from misalignment artifacts in form of blurry structures, which is not the case for the aligned reconstruction. While tomographic consistency is a logical concept and the data from a single, well aligned sinogram is sufficient to correct all other sinograms of the tomogram, there are also disadvantages. For one, shifting the sinogram may also move the rotation axis in the

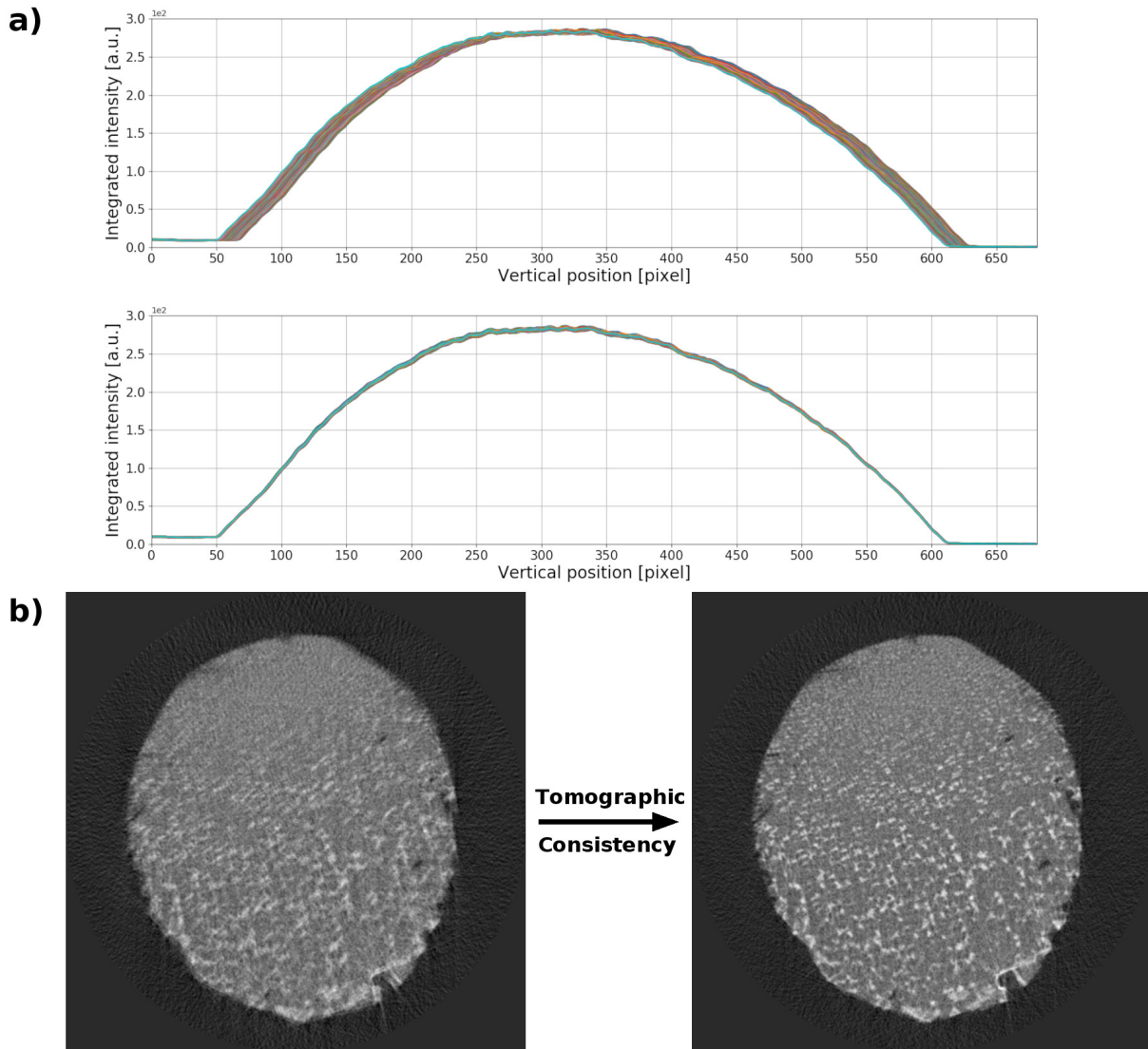


Figure 6.5: a) Vertical alignment: Horizontal integrals of the absorption projections before (top) and after (bottom) alignment. b) Horizontal alignment: FBP reconstruction of an absorption sinogram before (left) and after (right) alignment.

reconstruction, which may be undesirable if the measurements were performed using a specific experimental geometry. It is therefore important that the center-of-rotation for the tomographic consistency alignment is chosen to be as close as possible to the center-of-rotation of the measured sinograms. Furthermore, reconstruction artifacts and noise may negatively influence the alignment process, meaning it is important that the sinograms and slices used for alignment should be as free from artifacts and noise as possible.

After the projections were aligned in vertical as well as horizontal direction, absorption sinograms at different horizontal positions were reconstructed to check for a tilted rotation axis. Especially for bigger samples and small pixel sizes, the influence of a tilted rotation axis has to be considered. Fitting the height-dependent center-of-rotation using a linear or quadratic function allows to approximate a correction for a slightly tilted rotation axis.

Finally, all correction parameters determined by the alignment of the absorption signal were also applied to the datasets of the different XRF signals, resulting in aligned XRF sinograms.

6.2.2 MLEM Reconstruction

All tomographic reconstructions of the micrometeorite data were performed using the MLEM algorithm. While the conventional MLEM algorithm was sufficient for the reconstruction of the absorption tomogram, the XRF tomograms had to be reconstructed using the self-absorption corrected MLEM algorithm.

The absorption tomogram was reconstructed using 300 iterations of the conventional MLEM algorithm. During the first 100 iterations, a FMH prior (eq. 3.31) with a weight of $\beta = 0.3$ was applied to the reconstruction. While not required, considering the high signal-to-noise ratio of the absorption signal, the prior was applied to keep the reconstruction parameters of the absorption tomogram as consistent as possible with the reconstruction parameters of the XRF tomograms. Of the 362 recorded angles, 360 angles were used for the tomographic reconstructions, with the last angle of each of the two batches removed to avoid duplicate angular directions. The final reconstructed volume has a size of $360 \times 360 \times 341$ voxel in x -, y - and z -direction, respectively. Figure 6.6 shows two example slices of the reconstructed absorption volume as well as a 3D rendering. Although not elementally resolved, the characteristic parallel growths of the barred olivine micrometeorite are clearly visible. Using line profile analysis the resolution of the absorption volume was determined to be at least $2.56 \mu\text{m}$ FWHM or better (see supp. fig. S5).

The $K\alpha$ line XRF tomograms of Cr, Mn, Fe, Ni, As and Sr were reconstructed using 300 iterations of the self-absorption corrected MLEM algorithm. All elemental calibration factors are listed in supplementary table S4. A downscaling factor of 4 was used for the first 160 iterations, followed by 90 iterations with a downscaling factor of 3, 40 iterations with a downscaling factor of 2 and the final 10 iterations without downscaling. Furthermore, a FMH prior with a weight of $\beta = 0.3$ was applied during the first 100 iterations to mitigate the influence of noise in the XRF data. The primary beam energy was set to be 18 keV, in accordance with the experimental parameter, and the absorption threshold (eq. 4.1) was set to $T_{att} = 2 \cdot 10^{-4}$ to define a support for the reconstruction. Geometrically, the detector angle was defined as 90° for detector 0 and 270° for detector 2, with a sample-detector distance of 3 cm for both detectors. The shape of both Vortex detectors, including the 6 mm diameter collimators, was approximated using a 9×9 detector matrix with a detector pixel size of 0.75 mm:

$$\text{Detector Matrix} = \begin{pmatrix} 0 & 0 & 1 & 1 & 1 & 1 & 1 & 1 & 0 & 0 \\ 0 & 1 & 1 & 1 & 1 & 1 & 1 & 1 & 1 & 0 \\ 1 & 1 & 1 & 1 & 1 & 1 & 1 & 1 & 1 & 1 \\ 1 & 1 & 1 & 1 & 1 & 1 & 1 & 1 & 1 & 1 \\ 1 & 1 & 1 & 1 & 1 & 1 & 1 & 1 & 1 & 1 \\ 1 & 1 & 1 & 1 & 1 & 1 & 1 & 1 & 1 & 1 \\ 1 & 1 & 1 & 1 & 1 & 1 & 1 & 1 & 1 & 1 \\ 0 & 1 & 1 & 1 & 1 & 1 & 1 & 1 & 0 \\ 0 & 0 & 1 & 1 & 1 & 1 & 1 & 0 & 0 \end{pmatrix} \quad (6.8)$$

resulting in a total of 69 detector directions that had to be considered during the reconstruction.

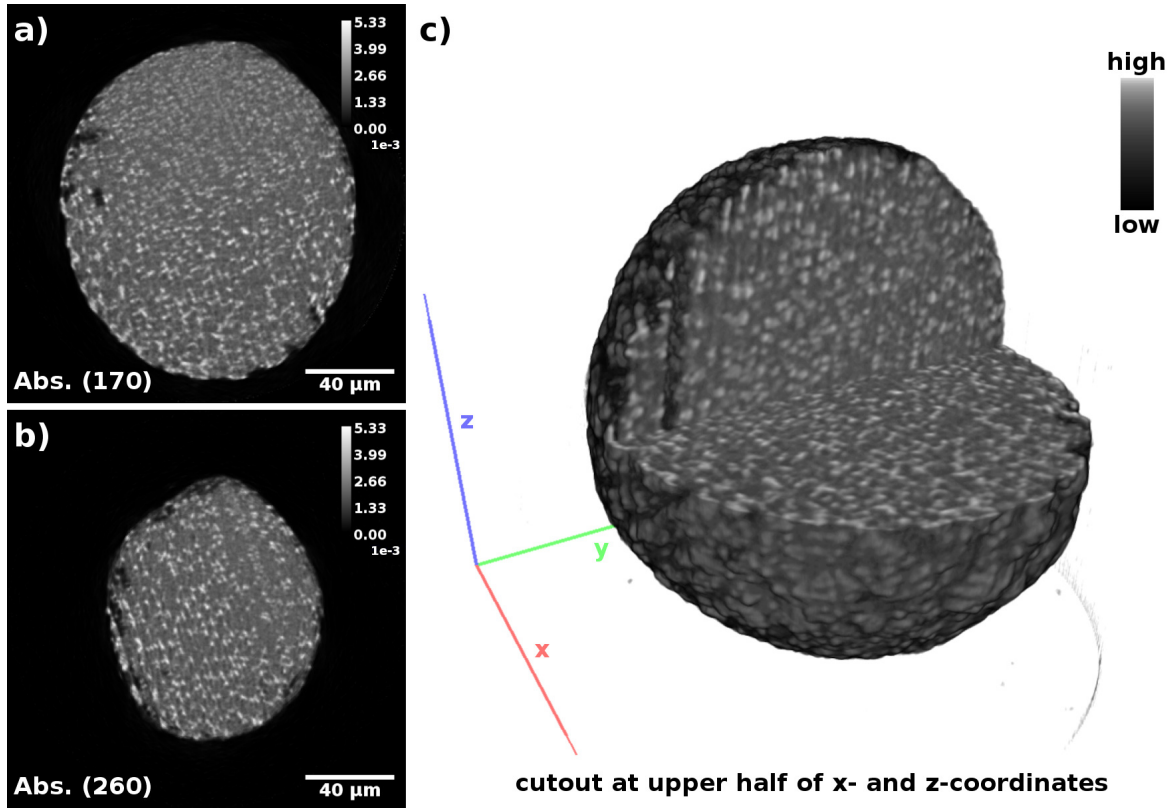


Figure 6.6: MLEM reconstruction of the primary beam absorption tomogram for slices a) $z = 170$ and b) $z = 170$, with the values given as dimensionless optical depth (note the factor of 10^{-3}). c) 3D rendering of the primary beam absorption volume with a cutout at high x - and z -coordinates for visualization. The 3D rendering was created in Drishti [Lim12].

Considering that the micrometeorite partially consists of low- Z elements, which are not covered by the reconstructed elements, it was necessary to perform the reconstruction using a background. To simulate the glassy mesostasis of the barred olivine micrometeorite, the compound of the background was defined as SiO_2 . The olivine may also contain a considerable amount of Mg. However, as Mg is close to Si in the periodic table, the difference between the energy dependent behaviors of their absorption coefficients is negligible.

Performing the reconstructions with an unconstrained background led to strong background artifacts in the elemental distributions, especially the Cr distribution. Even an activated background sloping for the first 5 iterations did not prevent the artifacts from occurring, implying a deeper problem with the calibration of the XRF data. For this reason, the background was limited using an empirical target value of $\lambda_{\text{rg}} = 1.025$ (eq. 4.37). In combination with adaptive calibration (eq. 4.40), this caused the reconstruction algorithm to converge into a stable solution. The final adaptive calibration factors were $C_{\text{ada}}^{\text{det}0} \approx 1.396$ for detector 0 and $C_{\text{ada}}^{\text{det}2} \approx 1.340$ for detector 2. There are three obvious possible causes that could explain these large adaptive calibration factors. For one, the elemental calibration determined using the calibration foils could be incorrect. However, as the elemental calibration was measured during the same experiment as the micrometeorite data, it is unlikely that it would cause such big inconsistencies. A more likely cause would be incorrect deadtime and pile-up corrections. As a consequence of the high

elemental concentrations in the micrometeorite, especially of the Fe, the measurements show strong deadtime and pile-up effects (see fig. 6.1). In this high count rate regime, even small inconsistencies in the correction model can have significant influence on the corrected count values. Considering that the deadtime and pile-up characterization of the Vortex detectors was performed as a separate experiment weeks after the micrometeorite experiment, it cannot be excluded that minor changes to the setup in the time between could have introduced such inconsistencies. Additionally, during the experiment the sensitivity of the ion chamber made it challenging to measure at very low count rates. However, the data points at low count rates are important for the linear fit that correlates OCR to ICR. If the linear fit is performed on data points already suffering from deadtime as well as pile-up effects, the calculated slope will be smaller than expected and OCR values will be correlated to too low ICR values, leading to only a partial correction. Furthermore, it is unknown what kind of influence the difference in primary beam energy or the choice of a Mn-foil as test sample may have had on the black-box optimizations performed by the Xspress3 pulse processors. Finally, as a consequence of the attempt to correct the first two possible causes, the adaptive calibration factors could have also been increased by an overaggressive background limiting. This shows the importance of correct detector characterization and elemental calibration, as the results of the self-absorption corrected tomographic reconstruction algorithm will only be as quantitative as the calibration of the input data.

For detector 0, the calculations were performed on a machine with an Intel Xeon E5-2640 v4 CPU, an NVIDIA Tesla P100 GPU and 512 GB of RAM and for detector 2 on a machine with an Intel Xeon Silver 4114 CPU, an NVIDIA Tesla P100 GPU and 768 GB of RAM. The average computation time for the entire self-absorption corrected reconstruction process was approximately 72.9 hours per detector. About 44.5 hours of that time ($\approx 61\%$) was spent to calculate the last 10 iterations without downscaling.

As a comparison, the XRF tomograms were also reconstructed without self-absorption correction. The parameters were identical to those used for the reconstruction of the absorption tomogram.

6.3 Volume Analysis

There are different methods to analyze the qualitative and quantitative properties of the self-absorption correction algorithm.

Table 6.1 shows the total elemental masses in the uncorrected and corrected reconstructed volumes for both detectors. For the calculation of the total mass, it was assumed that the voxel are cubic with a side length of 500 nm. Furthermore, the uncorrected values were calculated using only the basic elemental calibration, while the calculation of the corrected values also includes the adaptive calibration.

Table 6.1: Total elemental mass in the reconstructed volumes.

Element	$m_{\text{Uncorr.,det0}}$ [ng]	$m_{\text{Uncorr.,det2}}$ [ng]	$m_{\text{Corr.,det0}}$ [ng]	$m_{\text{Corr.,det2}}$ [ng]
Cr	6.814	8.305	35.40	41.71
Mn	10.41	11.29	42.69	43.38
Fe	395.9	402.4	1504	1486
Ni	15.17	15.93	112.5	111.4
As	0.3194	0.2859	0.8876	0.7598
Sr	0.2066	0.2105	0.4888	0.4583

It can be seen that the relative increase in total mass caused by the self-absorption correction has a tendency to increase with lower emission line energy. This is due to the increased self-absorption of the XRF radiation at lower energies, especially in the low-Z background. The exception to this tendency is the Ni reconstruction, with an average increase in total mass by a factor of 7.2. As a considerable fraction of the micrometeorite sample consists of Fe and the Ni-K α emission line is located only slightly above the Fe-K absorption edge in energy, the Ni-K α line is strongly absorbed by the Fe. In fact, the self-absorption of the Ni-K α line caused by the Fe even surpasses the self-absorption of the Cr-K α line, which is the lowest energy emission line reconstructed and only shows an average increase in total mass by a factor of 5.1.

The relative mass differences between the corrected reconstructions for both detectors can be used to judge the quantitative properties of the self-absorption correction algorithm and possible inconsistencies in the XRF data calibration. An average relative percent difference (RPD) of 16.4% for the corrected Cr volumes indicates inconsistencies in the background calculation. For the Mn, Fe and Ni volumes, the average RPD values are all below 2.0%, which is small enough to be considered consistent. However, the average RPD values for the As and Sr volumes are 15.5% and 6.4%, respectively. On one hand, as the As and Sr XRF radiation is less influenced by the self-absorption effects compared to the other elements, this could be an indication for general inconsistencies in the data calibration. These inconsistencies were already suspected to be present because of the large adaptive calibration factors. On the other hand, the As and Sr XRF signals are smaller than those of the other reconstructed elements by at least an order of magnitude, making it more challenging to extract quantitative results. On average, the RPD for all reconstructed elements is about 7.0%.

Four of the six reconstructed elements were chosen for the qualitative and quantitative analysis of their tomographic slices. Cr was chosen as the element with the lowest energy reconstructed emission line, making it suited to analyze the effects of background errors. Fe was chosen as one of the main elements in the micrometeorite. Ni was chosen as the element suffering the most from self-absorption effects. Finally, As was chosen as an element suffering less from self-absorption effects, but still having a structured distribution. On the other hand, the Mn-distribution very closely follows the Fe-distribution, making a separate analysis unnecessary. Sr is mostly located on the outside of the micrometeorite and even in the toothpick sample mount, creating the notion that it may be a terrestrial contamination. Lacking any structured distribution inside the micrometeorite, it was also excluded from the slice analysis. As it was the case for the calculation of the total masses, the density values in the uncorrected slices are based only on the basic elemental calibration, while density values in the corrected slices also factor in the results of the adaptive calibration.

Figure 6.7 shows tomographic slices of Cr, Fe, Ni and As for the uncorrected $K\alpha$ reconstruction of detector 0 as well as for the corrected reconstructions of both detectors. The slices correlate to a height of $z = 170$, which is equivalent to the center of the reconstructed volume and approximately to the center of the micrometeorite (compare fig. 6.6 a). They are therefore examples of the high self-absorption case.

The Cr and especially the Ni reconstruction suffer most from self-absorption, as is indicated by the strong shadowing effects towards the center of the sample in the uncorrected reconstructions. For the Cr the XRF signal originating in the center is difficult to distinguish from noise and for the Ni it is essentially fully absorbed. This causes problems with the self-absorption correction, as the algorithm does not create new data but only enhances the data that is already existing. As a consequence, the self-absorption correction amplifies the noise in the center of the sample for Cr and Ni, which introduces additional inconsistencies. The effect of these inconsistencies is especially apparent for the Ni in the finer structures on the edge of the sample. While they are clearly visible and defined in the uncorrected reconstruction, they are obscured by artifacts in the corrected reconstructions. It is therefore important to consider the limitations of self-absorption correction before deciding to measure a sample.

Another noticeable feature of the corrected reconstructions, especially for detector 0, is the increased elemental density in the center of the sample compared to the edge. This strongly indicates inconsistencies in the deadtime and pile-up correction. Considering that the relative influence of these corrections increases with the measured count rate, insufficient corrections on data suffering from self-absorption effects could create the notion of a weaker self-absorption than it is in reality. Basically, the high count areas of the measurements are insufficiently corrected, while the low count areas mostly stay the same. As a consequence, the measured values in regions suffering from high self-absorption are too large relative to those in regions with less self-absorption. In combination with the fact that the self-absorption algorithm scales the elemental density distributions to be consistent with the primary beam absorption volume for the purpose of determining the XRF absorption volumes (eq. 4.29) and the usage of adaptive cali-

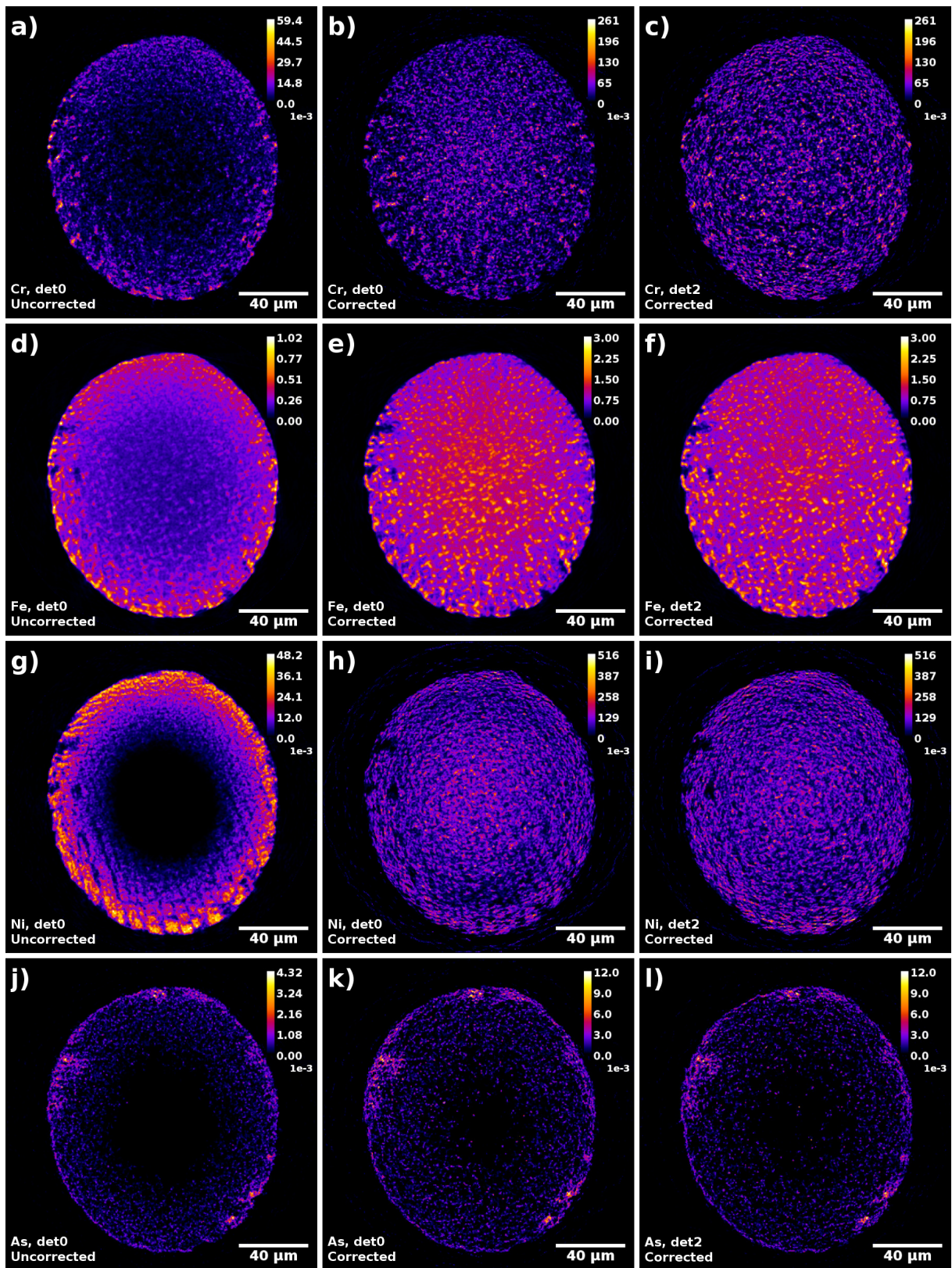


Figure 6.7: Uncorrected ($K\alpha$) reconstruction for detector 0 and corrected reconstructions for detector 0 and 2 for a)-c) Cr, d)-f) Fe, g)-i) Ni as well as j)-l) As. The height of the slice is $z = 170$ and all values are given in g/cm^3 (note the factor of 10^{-3} for Cr, Ni and As). For better comparability, the corrected slices of both detectors are displayed on an identical scale.

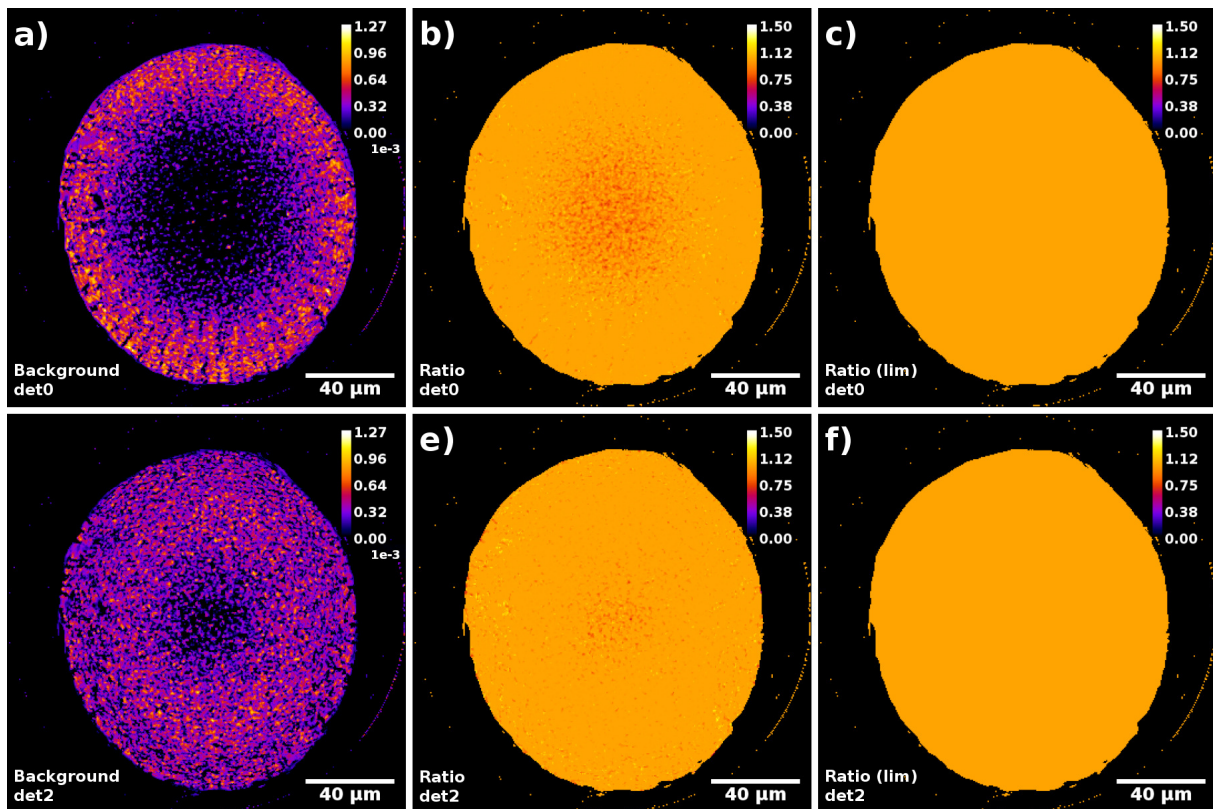


Figure 6.8: Background, ratio applied to the density volumes (see eq. 4.29) and ratio applied to the density volumes after background limiting (see eq. 4.41) for a)-c) detector 0 as well as d)-e) detector 2. The height of the slice is $z = 170$ and the values of the background are given as dimensionless optical depth (note the factor of 10^{-3}). For better comparability, the backgrounds as well as the ratios of both detectors are displayed on identical scales.

bration, this leads to a relative overcorrection of the densities in the center of the sample. It also leads to artifacts in the background, as can be seen in figure 6.8 a) and d). As the background is defined as the part of the primary beam absorption not covered by the simulated absorption of the reconstructed elements, an overcorrection of elemental densities automatically leads to an underestimated background. Figure 6.8 b) and e) show the ratios applied to the elemental density distributions (eq. 4.29) and backgrounds (eq. 4.34) during the final iteration. It can be seen that the densities in the center of the elemental data is strongly overestimated, consistently reducing the background in those regions and causing artifacts. The reason that this effect is stronger for detector 0 is most likely a consequence of its weaker deadtime correction (see fig. 6.2).

Figure 6.9 shows the tomographic slices correlating to a height of $z = 260$. This height is equivalent to the upper region of the micrometeorite, where the diameter of the sample is smaller than in the center (compare fig. 6.6 b). These slices are therefore examples of the medium to low self-absorption case.

Compared to the high self-absorption case discussed above, the shadowing effects towards the center of the sample are weaker. XRF signal originating in the center can reach the XRF detectors without being fully absorbed, which mitigates the problem of the algorithm just amplifying

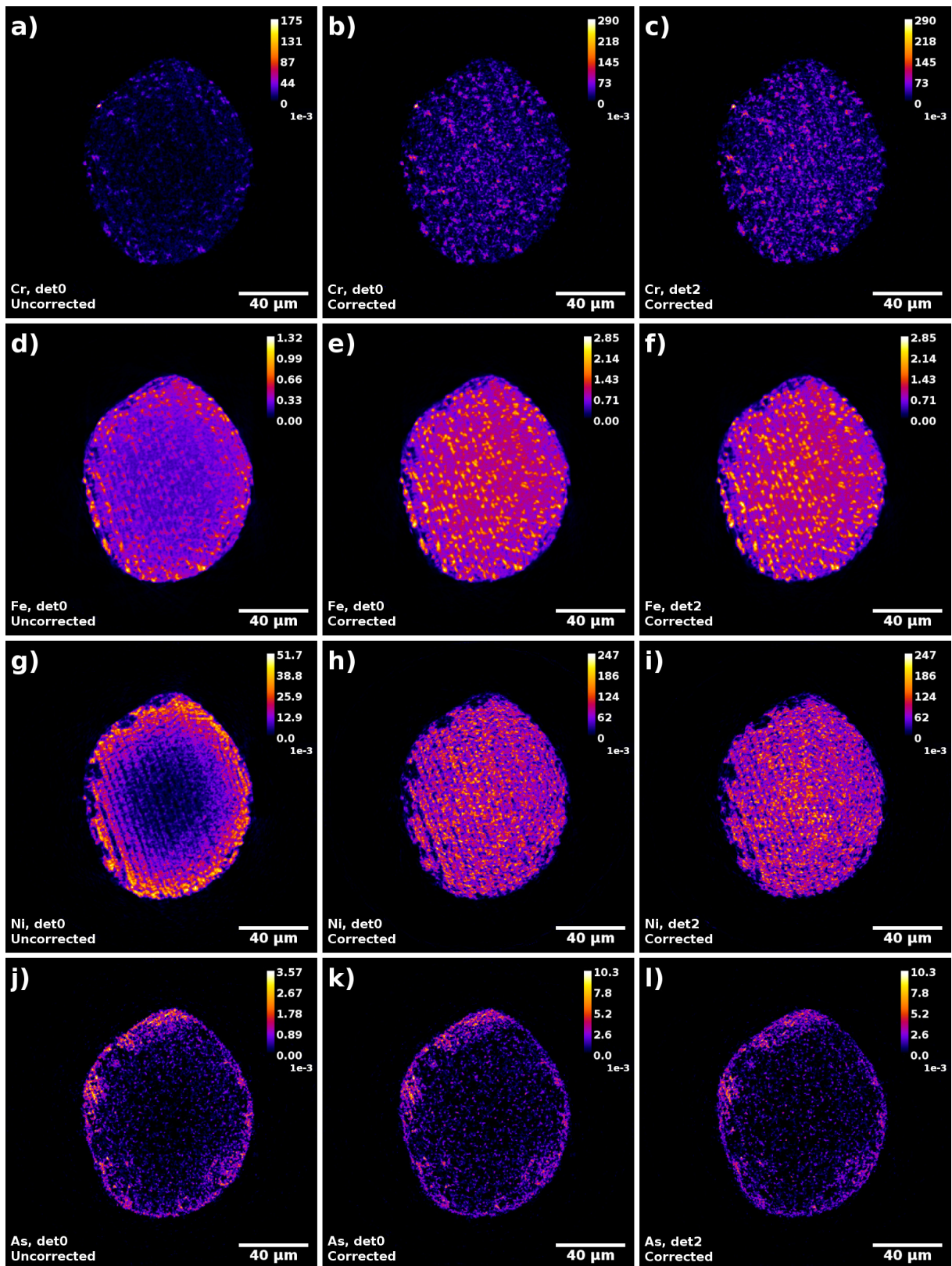


Figure 6.9: Uncorrected ($K\alpha$) reconstruction for detector 0 and corrected reconstructions for detector 0 and 2 for a)-c) Cr, d)-f) Fe, g)-i) Ni as well as j)-l) As. The height of the slice is $z = 260$ and all values are given in g/cm^3 (note the factor of 10^{-3} for Cr, Ni and As). For better comparability, the corrected slices of both detectors are displayed on an identical scale.

noise. In the center of both the corrected Cr and the corrected Ni reconstructions, structures are visible that are identical for both detectors and therefore most likely real. As the amount of inconsistencies caused by falsely intensified noise is decreased, there are also less reconstruction artifacts overall.

Furthermore, the reduced self-absorption is beneficial in regards to the overcorrection of elemental densities in the center of the sample caused by incorrect deadtime and pile-up corrections. With less self-absorption, the relative differences in measured count rates are on average smaller, meaning that the relative inconsistencies caused by the deadtime and pile-up corrections will also be smaller.

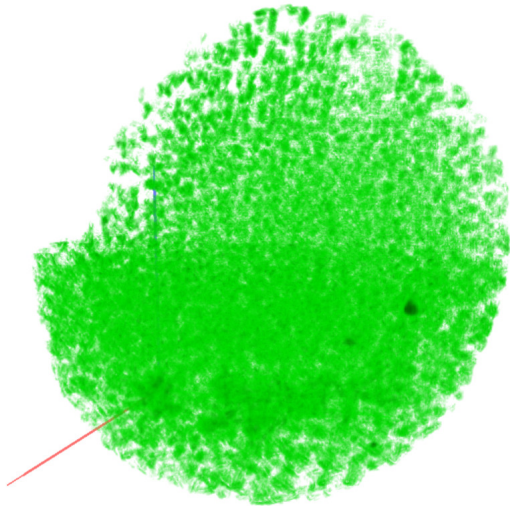
Apart from the problems caused by low XRF signals and incorrect calibrations, the self-absorption correction worked as expected. It increased the overall density values, reduced self-absorption artifacts, especially the shadowing towards the center of the sample, and corrected the elemental XRF data to be mostly consistent with the STXM data.

Figure 6.10 shows 3D renderings of the Cr, Fe, Ni and As density distributions using the results from detector 2. As already discussed above, for Cr and Ni the values in the center of the sample are defined by amplified noise. Further towards the edge of the sample, the influence of this noise is reduced, leading to more truthful elemental distributions. The Fe and As distributions are mostly unaffected by these problems.

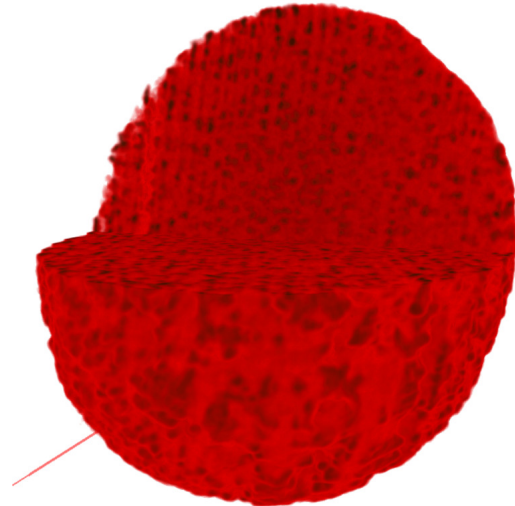
As a main element in the micrometeorite, the Fe distribution is closely correlated to the structures visible in the absorption tomogram (compare fig. 6.6), exhibiting the characteristic parallel growths of olivine. There also seems to be a large quantity of Fe, most likely in form of magnetite crystals (Fe_3O_4), in the glassy mesostasis [FC15]. The hot-spots in the Cr distribution are mainly correlated to the magnetite crystals, possibly in the form of chromite (FeCr_2O_4). Conversely, the Ni distribution seems to be anticorrelated to the regions including magnetite crystals, indicating that it is incorporated into the olivine. A special feature of the Ni distribution is a region of high Ni density, depicted in the lower right of the Ni distribution shown in figure 6.10. This region is most likely the remnant of an FeNi metal bead, which occasionally form in micrometeorites [GEGT08]. These beads are sometimes ejected during the deceleration of the micrometeorite in Earth's atmosphere. It has to be mentioned, however, that an exact analysis of the Cr and Ni distributions is not possible due to the noise and artifacts introduced by uncorrectable self-absorption effects and inconsistencies in the experimental calibration. As is mainly located at the edge of the sample. Assuming the micrometeorite was spinning while entering the atmosphere, this may possibly be a consequence of centrifugal forces separating the heavy As atoms from the other, lighter atoms and moving them towards the outer parts of the micrometeorite.

The exact interpretation of the elemental distributions in the micrometeorite will be left to the learned astrophysicist.

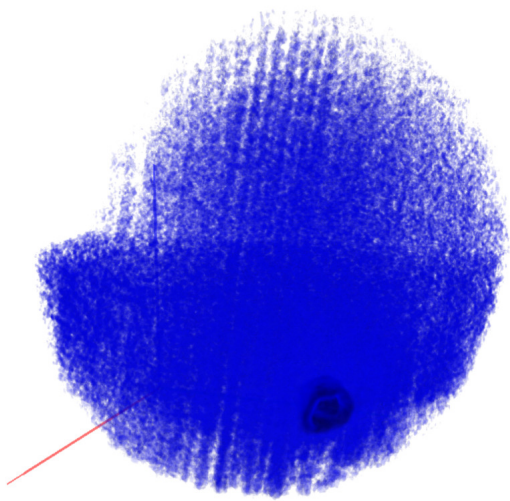
Cr



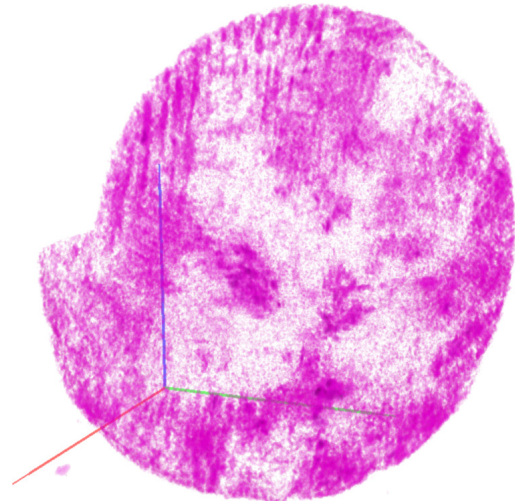
Fe



Ni



As



cutout at upper half of x- and z-coordinates

Figure 6.10: 3D renderings of the self-absorption corrected micrometeorite reconstructions for Cr, Fe, Ni and As, measured by detector 2. Darker colors equal higher mass densities. A cutout at high x- and z-coordinates was applied for visualization. Created in Drishti [Lim12].

Chapter 7

Conclusion & Outlook

In conclusion, the 3D self-absorption corrected algorithm for the MLEM reconstruction of XRF tomograms fulfills its purpose. The numerical simulations show that it corrects self-absorption artifacts qualitatively as well as quantitatively for single and multiple elements, even in the presence of Poisson noise and an unmeasured low- Z element absorption background. However, synchrotron measurements of a barred olivine micrometeorite sample also show that the results of the self-absorption correction algorithm are highly dependent on the experimental calibration of the data. Especially inconsistencies in the deadtime and pile-up corrections limit the quality of the reconstructions, as they cannot be corrected by the adaptive calibration of the algorithm. Future experiments therefore have to be performed in such a way to reduce deadtime and pile-up losses as much as possible. This can be achieved, for example, by limiting the overall flux of the X-ray beam, if the elemental concentrations in the sample allow it, or by using large solid angle, multi-element XRF detectors in place of the small, single-element Vortex detectors.

There are multiple possible improvements to consider for the self-absorption correction algorithm. The most important one would be an improved description of the XRF detector, the absorption effects between sample and detector as well as the elemental calibration factors. In the current implementation, the elemental calibration factors are calculated using the direct path from the center of the sample volume to the center of the detector. This, however, does not take into account possible path length differences for non-center positions either in the sample volume or the plane of the detector. In case of small detectors the direct path approximation is sufficient. For example, using the sample and detector geometry of the micrometeorite experiment, the maximum path length difference compared to the 30 mm direct path would be about 0.16 mm or 0.53%. Larger detectors, however, would require elemental calibration factors dependent on the location of the voxel in the sample volume and dependent on the position on the XRF detector, complicating and slowing down the self-absorption correction calculations. Another possible improvement would be the usage of trilinear instead of nearest-neighbor interpolation in the calculation of the XRF transmission volumes (eq. 4.15). This could potentially increase the accuracy, but also decrease the performance of the algorithm. Less related to the self-absorption correction itself and more to the underlying MLEM algorithm would be the idea

to vary the amount of iterations the Bayesian prior is applied to the reconstruction for each XRF line. Elements with a high signal-to-noise ratio could be reconstructed with only a few iterations of prior applied, focusing on increased resolution, while elements suffering from noise could be reconstructed with more iterations of prior applied, benefiting from its noise reducing properties. Finally, it could be beneficial to improve the current, relatively rudimentary implementation of background limiting. For example, detecting an overestimated background should be possible using histogram analysis of the measured and simulated sinograms.

In future, the algorithm could be used for pseudo self-absorption corrected spectral tomography. Occasionally, the XRF lines of trace elements may lack the necessary statistics to be fitted correctly in the projection data, especially if the measurements suffer from strong self-absorption effects. Assuming the trace elements have a negligible influence on the total absorption inside the sample, it should be possible to use the self-absorption corrected MLEM algorithm to approximate to quantitative distribution of all other elements. These distributions could then be used to reconstruct a self-absorption corrected tomographic volume for every bin of the XRF spectra. Due to the dose fractionation effect [dJRJ14], the statistics for trace the elements should be improved in the reconstructed voxel compared to the projected pixel.

Supplement

Config Parameters

name [unit], type
description.

[example (simulated multi-element phantom with background)]

nthreads [#], int

Maximum number of CPU threads for *OpenMP* calculations.

[nthreads = 40]

inputabs [-], string

Absolute or relative path to the slices of the absorption tomogram. Naming convention for the absorption slices is '[z]_Absorption.tif'.

[inputabs = './mlem/Absorption/']

inputsin [-], string

Absolute or relative path to the elemental sinogram directories. Naming convention for the elemental directories and sinograms is '[element]/[z]_[element].tif'.

[inputabs = './sinograms/']

outputdir [-], string

Absolute or relative path to the output directory. Will be created if it does not exist already.

[outputdir = './mlemlsa/']

xydim [#], int

Number of voxel in *x*- and *y*-direction / translational positions in the sinograms. Location of the axis of rotation: $\lfloor xydim/2 \rfloor$

[xydim = 300]

zdim [#], int

Number of voxel in *z*-direction / number of slices.

[zdim = 300]

pixelsize [cm], float

Pixel/voxel size of the measured data in cm.

[pixelsize = 1e-4]

bigsample [-], bool

If false: Small-sample approximation will be used for the calculation of the XRF radiation transmission volumes.

[bigsample = true]

prelem [-], bool

If true: Enables the use of conventional MLEM iterations before the self-absorption corrected MLEM reconstruction.

[prelem = false]

preiters [#], int

Number of pre-MLEM iterations.

[preiters = 10]

nsect [#], int

Number of sections of the self-absorption corrected algorithm. Each section is defined by an amount of iterations and a downscale factor.

[nsect = 4]

iters [#], array of ints

Amount of iterations for each section of the algorithm.

[iters = (160, 90, 40, 10)]

scalefluo [-], bool

If true: Enables downscaling for the calculation of the XRF transmission volumes.

[scalefluo = true]

fluoscale [-], array of ints

Downscale factor for each section of the algorithm.

[fluoscale = (4, 3, 2, 1)]

applymrp [-], bool

If true: Enables Bayesian priors for MLEM reconstruction.

[applymrp = true]

usefmh [-], bool

If true: Uses FMH Bayesian prior. If false: Uses MRP Bayesian prior.

[usefmh = true]

mrpbeta [-], float

Weight β of the Bayesian prior (eq. 3.29).

[mrpbeta = 0.3]

mrpiter [#], int

Maximum iteration until which the Bayesian prior is applied.

[mrpiter = 100]

mrpperi [#], int

The Bayesian prior will be applied every mrpperi iterations.

[mrpperi = 1]

preenergy [keV], float

Primary beam energy in keV.

[preenergy = 18.0]

prethresh [-], float

Attenuation threshold T_{att} (eq. 4.1). Only used if $T_{att} > 0$.

[prethresh = 0.0]

nelem [#], int

Number of reconstructed elements.

[nelem = 3]

elements [-], list of strings

List of reconstructed elements.

[elements = ('Ti', 'Fe', 'Zn')]

nline [#], int

Number of reconstructed XRF lines.

[nline = 6]

lines [-], list of strings

List of reconstructed XRF lines.

[lines = ('Ti-Ka', 'Ti-Kb', 'Fe-Ka', 'Fe-Kb', 'Zn-Ka', 'Zn-Kb')]

rhos [-], list of floats

List of calibration factors $P_{cal,L}$ (eq. 6.7) in the same order as the list of lines.

[rhos = (0.331897, 2.42399, 0.11441, 0.835312, 0.0560234, 0.405986)]

denthresh [-], float

Absorption threshold T_L for density constraints (eq. 4.26). Only used if $T_L \geq T_{att}$.

[denthresh = 0.0]

denlimit [-], float

Limit λ_L for density constraints (eq. 4.26).

[denlimit = 0.0]

anglefile [-], string

Absolute or relative path to the list of tomographic angles.

[anglefile = './angles_nsort.txt']

nangles [#], int

Number of tomographic angles. Has to be consistent with the number of angles in the anglefile.

[nangles = 361]

detfile [-], string

Absolute or relative path to the binary detector image file.

[detfile = './detector.tif']

absmode [°], float

Detector angle δ_{det} from the x -axis in ° (fig. 4.3).

[absmode = 270]

detdimx [#], int

Number of detector pixel in x_{det} -direction.

[detdimx = 9]

detdimy [#], int

Number of detector pixel in y_{det} -direction.

[detdimy = 9]

detpxsize [cm], float

Detector pixel size d_{det} in cm (eq. 4.3).

[detpxsize = 1e-1]

distance [cm], float

Sample-detector distance s_{det} in cm (fig. 4.3).

[distance = 1.0]

usebackground [-], bool

If true: Uses background for self-absorption correction.

[usebackground = true]

bgcompound [-], string

Defines the compound of the background.

[bgcompound = 'SiO2']

scalinglaw [-], float

If background is used, but compound is empty (""): Defines parameter γ for the background scaling law (eq. 4.9).

[scalinglaw = -2.85]

bgslope [#], int

Strength λ_{slp} for background sloping (eq. 4.35). Only used if $\lambda_{slp} > 0$.

[bgslope = 0]

limitbg [-], bool

If true: Uses background limiting.

[limitbg = false]

limtrg [-], float

Target value λ_{trg} for background limiting (eq. 4.37).

[limtrg = 1.025]

limiter [-], int

Maximum iteration until which the background will be limited.

[limiter = 300]

adaptcal [-], bool

If true and background is limited: Use adaptive calibration.

[adaptcal = true]

savesteps [#], int

Iteration period intermediate results are saved. Deactivated if 0.

[savesteps = 10]

saveheight [-], int

z-height for the saving of intermediate results.

[saveheight = 93]

savelines [-], bool

If true: Additionally saves reconstructed lines, instead of just the elements.

[savelines = false]

savesimsins [-], bool

If true: Additionally saves simulated sinograms.

[savesimsins = false]

savefluoabs [-], bool

If true: Additionally saves XRF absorption volumes.

[savefluoabs = false]

Note about the coordinate system and loading in data: The x -axis is defined by the beam direction and the z -axis is defined by the axis of rotation as well as the direction of the rotation. Then the y -axis follows from the right-handedness of the coordinate system. Loading in slices from top to bottom, e.g. slice 0 equals high z -values, is possible, as long as x - and y -direction are correctly defined. However, in that case the detector image also has to be flipped in z -direction.

Numerical Simulations

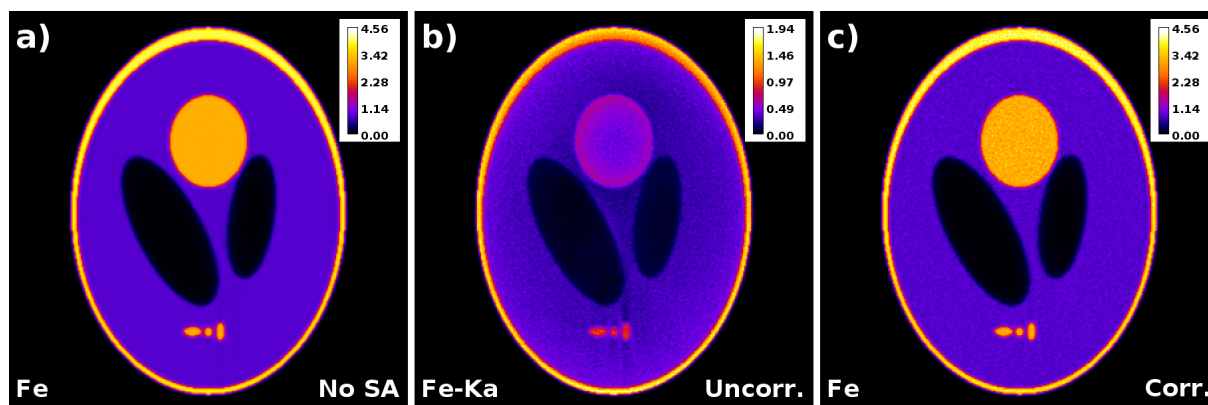


Figure S1: a) Ground truth, b) uncorrected ($K\alpha$) and c) corrected reconstruction for the noisy single-element Fe simulation without background. For comparability reasons ground truth and corrected reconstruction are on an identical scale, while the uncorrected reconstruction is scaled separately for visibility. All values given in g/cm^3 .

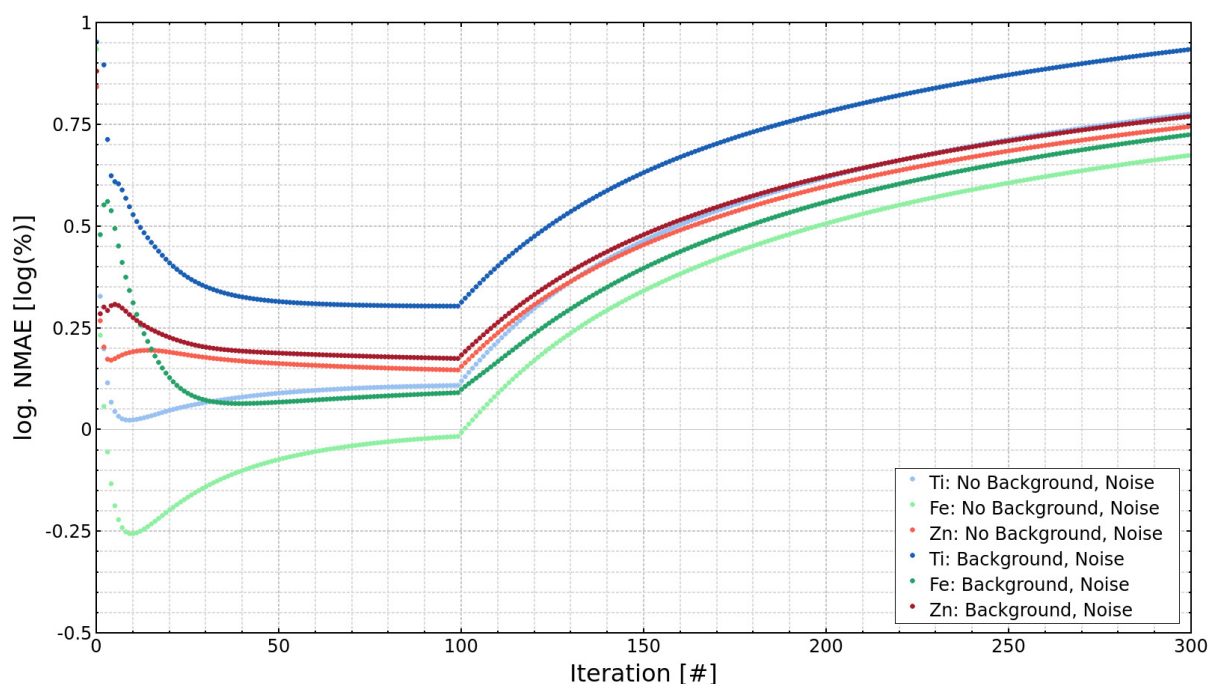


Figure S2: Logarithmic (\log_{10}) percentual normalized mean absolute errors (eq. 3.33) at different iterations for the noisy multi-element simulations. Calculated is the error of the $K\alpha$ line reconstruction of an element compared against the average of all line reconstructions of the element.

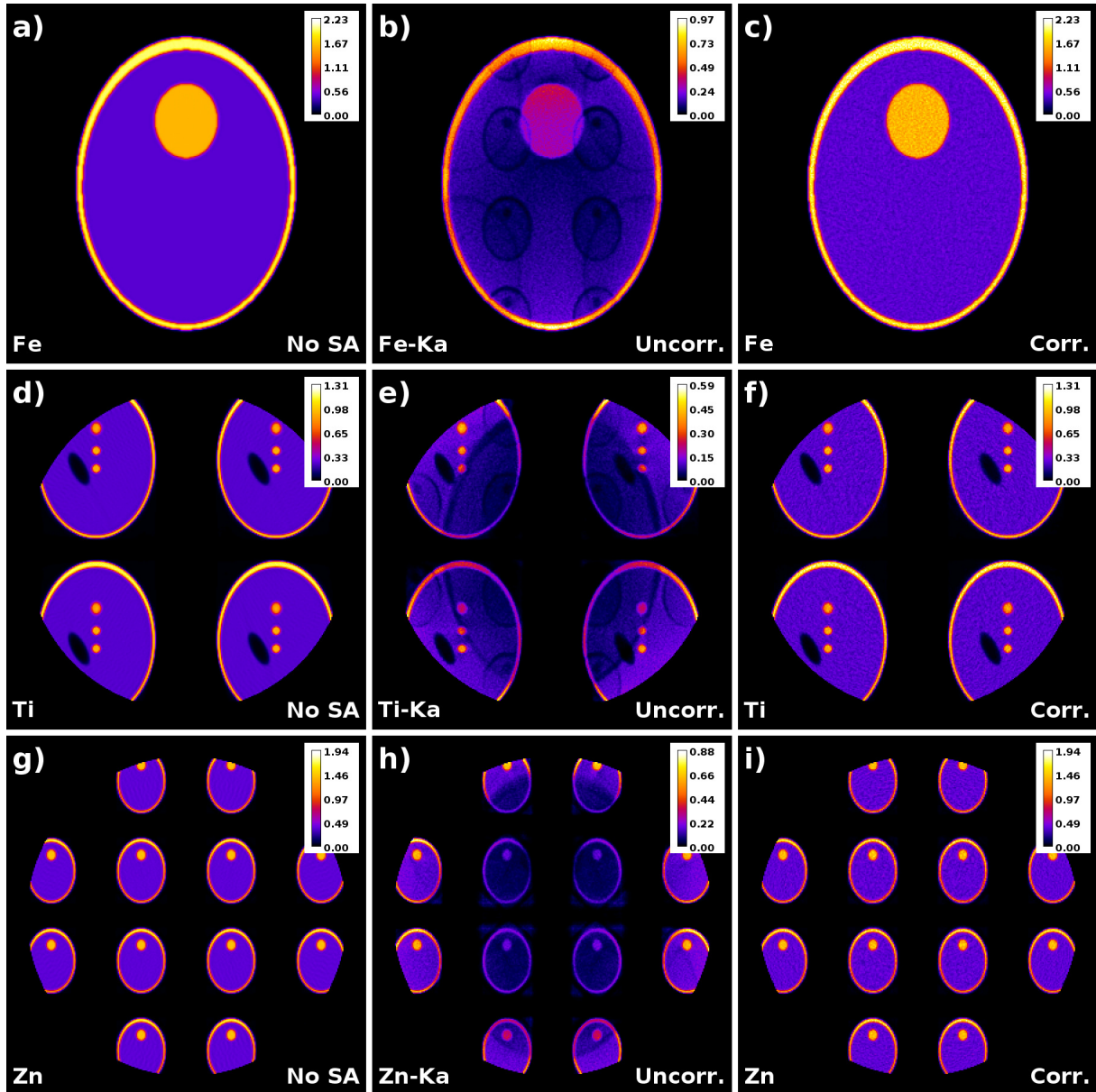


Figure S3: Ground truth, uncorrected ($K\alpha$) and corrected reconstruction of a)-c) Fe, d)-f) Ti and g)-i) Zn for the noisy multi-element simulation without background. For comparability reasons ground truth and corrected reconstruction are on an identical scale, while the uncorrected reconstruction is scaled separately for visibility. All values given in g/cm^3 .

Deadtime and Pile-Up Correction

Table S1: Parameters for the deadtime fits in figure 6.2 as well as for the pile-up fits in supplemental figure S4.

Detector	τ_P [s]	τ_N [s]	τ_T [s]	m_{pu} [s]
Channel 0	$1.7512 \cdot 10^{-7}$	$2.8565 \cdot 10^{-7}$	$1.7628 \cdot 10^{-7}$	$1.0111 \cdot 10^{-7}$
Channel 2	$4.0437 \cdot 10^{-7}$	$5.9493 \cdot 10^{-7}$	$2.7398 \cdot 10^{-7}$	$8.5582 \cdot 10^{-8}$

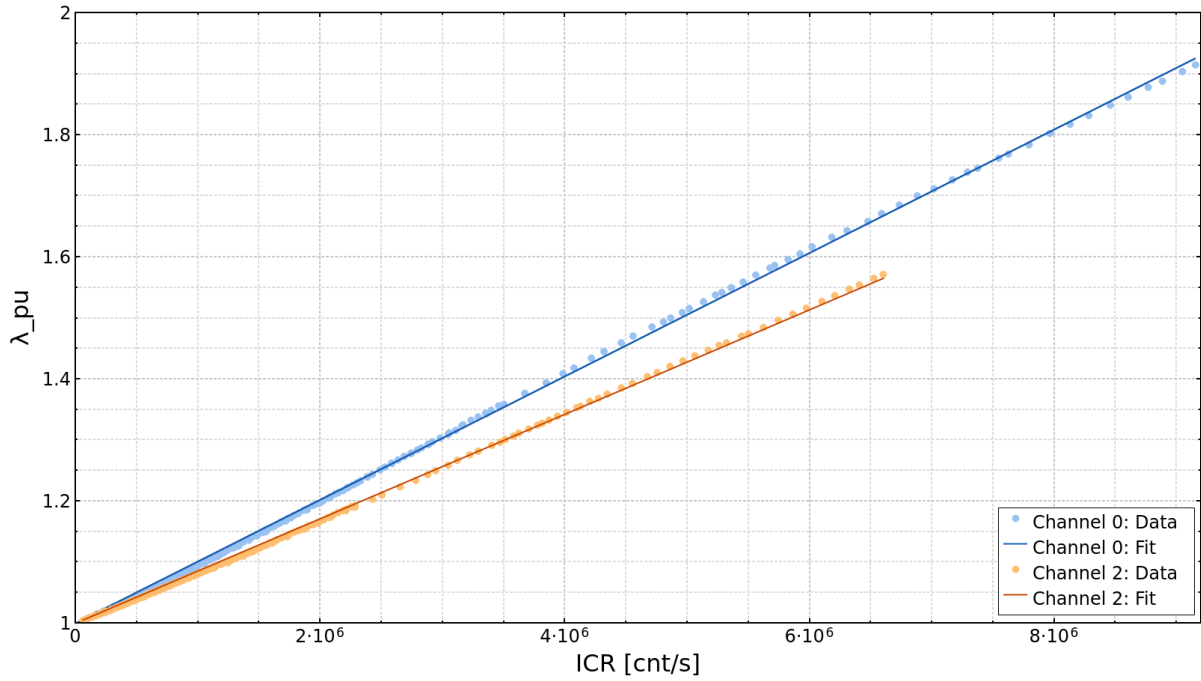


Figure S4: Plot and fit (eq. 6.2) of the λ_{pu} over ICR data that was recorded using Mn-foils. The fit parameter for both detectors can be found in supplementary table S1.

Calibration Factors

Table S2: Calibration foils. Tilt of 45° already included in area mass density.

Element	ρ_{2D} [g/cm ²]	$N_A \sigma_{xrf, K\alpha}(E_0)/M_Z$ [cm ² /g]
Cr	$62.51 \cdot 10^{-6}$	6.154
Fe	$77.78 \cdot 10^{-6}$	9.434
Ni	$70.71 \cdot 10^{-6}$	13.94
Cu	$67.74 \cdot 10^{-6}$	15.76

Table S3: Intermediate values for the calculation of the experimental calibration constant.

Line	$\hat{R}_{K\alpha,d}^{\text{det0}}$	$\hat{R}_{K\alpha,s}^{\text{det0}}/\rho_{2D}$ [cm ² /g]	$\hat{R}_{K\alpha,d}^{\text{det2}}$	$\hat{R}_{K\alpha,s}^{\text{det2}}/\rho_{2D}$ [cm ² /g]
Cr-K α	$1.735 \cdot 10^{-3}$	32.66	$1.618 \cdot 10^{-3}$	30.45
Fe-K α	$4.224 \cdot 10^{-3}$	59.93	$3.997 \cdot 10^{-3}$	56.71
Ni-K α	$5.197 \cdot 10^{-3}$	78.34	$4.902 \cdot 10^{-3}$	73.89
Cu-K α	$5.766 \cdot 10^{-3}$	90.01	$5.431 \cdot 10^{-3}$	84.78

Table S4: Elemental calibration factors $P_{cal,L}$ used for the self-absorption corrected tomographic reconstruction of the micrometeorite data.

Line	Channel 0	Channel 2
Cr-K α	$3.323 \cdot 10^{-2}$	$3.525 \cdot 10^{-2}$
Mn-K α	$2.622 \cdot 10^{-2}$	$2.782 \cdot 10^{-2}$
Fe-K α	$2.033 \cdot 10^{-2}$	$2.157 \cdot 10^{-2}$
Ni-K α	$1.330 \cdot 10^{-2}$	$1.410 \cdot 10^{-2}$
As-K α	$7.556 \cdot 10^{-3}$	$8.016 \cdot 10^{-3}$
Sr-K α	$6.814 \cdot 10^{-3}$	$7.228 \cdot 10^{-3}$

Resolution

Fit function for line profile:

$$f(x) = y_0 + A \operatorname{erf}\left(\frac{(x-x_c)}{\sigma}\right) \quad (\text{S.1})$$

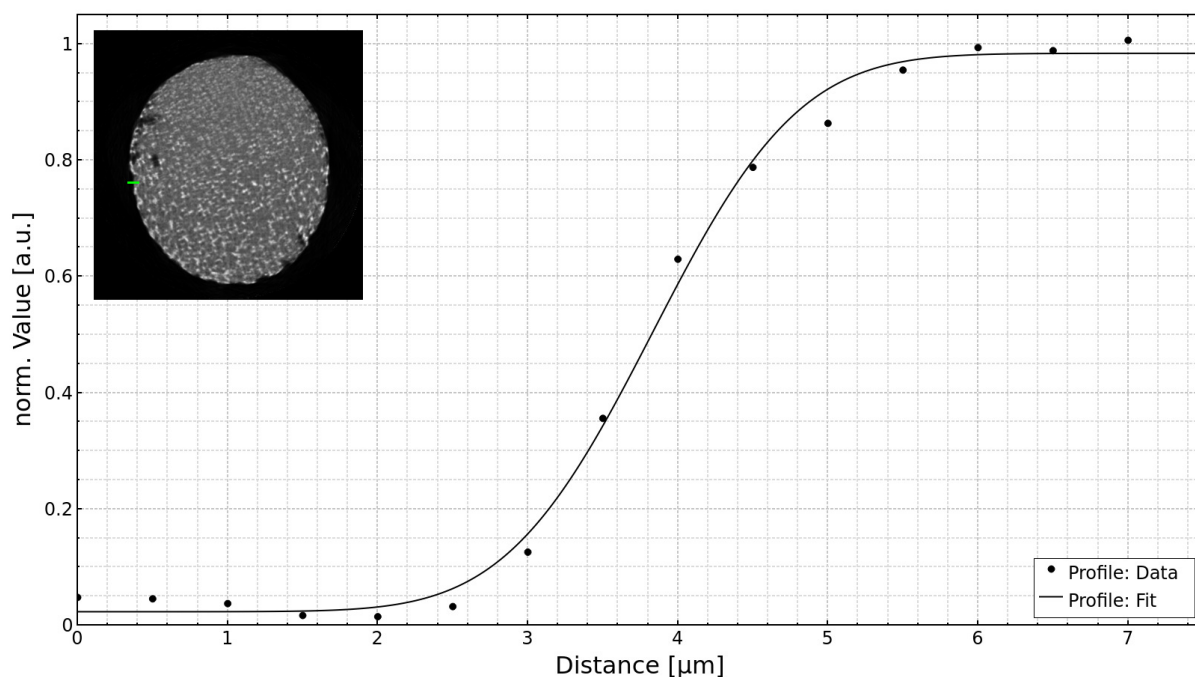


Figure S5: Plot and fit (supp. eq. S.1) of an absorption volume line profile (green line in inset). The fit parameters can be found in supplementary table S5.

Table S5: Parameters for the fit in supplementary figure S5.

Parameter	Value	Error
Range	[1.5, 6.5]	-
R^2	0.9964	-
y_0	0.5035	0.000265
A	0.4803	0.000286
x_c	3.831	0.00129
σ	1.086	0.00246

Info 1: The values of σ and x_c are given in microns.

Info 2: $\text{FWHM} = 2\sqrt{2\ln 2}\sigma$

Bibliography

- [ANM11] J. Als-Nielsen and D. McMorrow. *Elements of Modern X-ray Physics*. John Wiley & Sons, Hoboken, 2nd edition, 2011.
- [AR97] S. Alenius and U. Ruotsalainen. “Bayesian image reconstruction for emission tomography based on median root prior”. *Eur. J. Nucl. Med.*, **24**(3):258–265, 1997. <http://dx.doi.org/10.1007/BF01728761>.
- [AR02] S. Alenius and U. Ruotsalainen. “Generalization of median root prior reconstruction”. *IEEE Trans. Med. Imaging*, **21**(11):1413–1420, 2002. <http://dx.doi.org/10.1109/TMI.2002.806415>.
- [ARA97] S. Alenius, U. Ruotsalainen, and J. Astola. “Using local median as the location of the prior distribution in iterative emission tomography image reconstruction”. In *1997 IEEE Nuclear Science Symposium Conference Record*, volume 2, pages 1726–1730, 1997. <http://dx.doi.org/10.1109/NSSMIC.1997.670650>.
- [Att99] D. Attwood. *Soft X-Rays and Extreme Ultraviolet Radiation*. Cambridge University Press, 1999.
- [BBC⁺20] A.-L. Bulin, M. Broekgaarden, F. Chaput, V. Baisamy, J. Garrevoet, B. Busser, D. Brueckner, A. Youssef, J.-L. Ravanat, C. Dujardin, V. Motto-Ros, F. Lerouge, S. Bohic, L. Sancey, and H. Elleaume. “Radiation Dose-Enhancement Is a Potent Radiotherapeutic Effect of Rare-Earth Composite Nanoscintillators in Preclinical Models of Glioblastoma”. *Advanced Science*, **7**(20):2001675, 2020. <http://dx.doi.org/10.1002/advs.202001675>.
- [BFG⁺19] M. Bordessoule, E. Fonda, N. Guignot, J. P. Itie, C. Meneglier, and F. Orsini. “Performance of spectroscopy detectors and associated electronics measured at SOLEIL synchrotron”. *AIP Conference Proceedings*, **2054**(1):060070, 2019. <https://doi.org/10.1063/1.5084701>.
- [Bru02] P. P. Bruyant. “Analytic and Iterative Reconstruction Algorithms in SPECT”. *J. Nucl. Med.*, **43**(10):1343–1358, 2002.

- [CCC⁺14] C.-C. Cheng, C.-C. Chien, H.-H. Chen, Y. Hwu, and Y.-T. Ching. “Image Alignment for Tomography Reconstruction from Synchrotron X-Ray Microscopic Images”. *Plos ONE*, **9**(1):e84675, 2014. <http://dx.doi.org/10.1371/journal.pone.0084675>.
- [DCH⁺17] Z. W. Di, S. Chen, Y. P. Hong, C. Jacobsen, S. Leyffer, and S. M. Wild. “Joint reconstruction of x-ray fluorescence and transmission tomography”. *Opt. Express*, **25**(12):13107–13124, 2017. <http://dx.doi.org/10.1364/OE.25.013107>.
- [dJRJ14] M. D. de Jonge, C. G. Ryan, and C. J. Jacobsen. “X-ray nanoprobe and diffraction-limited storage rings: opportunities and challenges of fluorescence tomography of biological specimens”. *J. Synchrotron Rad.*, **21**(5):1031–1047, 2014. <http://dx.doi.org/10.1107/S160057751401621X>.
- [DNC⁺15] J. Deng, Y. S. G. Nashed, S. Chen, N. W. Phillips, T. Peterka, R. Ross, S. Vogt, C. Jacobsen, and D. J. Vine. “Continuous motion scan ptychography: characterization for increased speed in coherent x-ray imaging”. *Opt. Express*, **23**(5):5438–5451, 2015. <http://dx.doi.org/10.1364/OE.23.005438>.
- [dSBvM⁺20] B. de Samber, M. Bensellam, S. J. M. van Malderen, F. Seiboth, D. Brückner, J. Garrevoet, G. Falkenberg, J.-C. Jonas, and L. Vincze. “Proof-of-concept for 2D/CT element analysis of entire cryofrozen islets of Langerhans using a cryo-loop synchrotron X-ray fluorescence setup”. *J. Anal. At. Spectrom.*, **35**:1368–1379, 2020. <http://dx.doi.org/10.1039/D0JA00067A>.
- [Fal15] G. Falkenberg. “The Maia detection system at P06”. <http://www.esrf.eu/files/live/sites/www/files/events/conferences/2015/ParisSpectroscopy/PDF/Falkenberg.pdf> (Last access: 03.07.2021), 2015. X-ray Spectroscopy Detectors for Present and Future Synchrotron, Paris.
- [FC15] L. Folco and C. Cordier. “Micrometeorites”. In *Planetary Mineralogy*, pages 253–297. European Mineralogical Union, 2015. <http://dx.doi.org/10.1180/EMU-notes.15.9>.
- [GEGT08] M. J. Genge, C. Engrand, M. Gounelle, and S. Taylor. “The classification of micrometeorites”. *Meteoritics & Planetary Science*, **43**(3):497–515, 2008. <http://dx.doi.org/10.1111/j.1945-5100.2008.tb00668.x>.
- [GLD⁺20] B. Gao, B. Laforce, J. Dhaene, L. Vincze, L. Van Hoorebeke, and M. N. Boone. “An analytical simulation method for X-ray fluorescence computed tomography”. *Radiation Physics and Chemistry*, **170**:108622, 2020. <http://dx.doi.org/10.1016/j.radphyschem.2019.108622>.

- [GSDH⁺11] M. Guizar-Sicairos, A. Diaz, M. Holler, M. S. Lucas, A. Menzel, R. A. Wepf, and O. Bunk. “Phase tomography from x-ray coherent diffractive imaging projections”. *Opt. Express*, **19**(22):21345–21357, 2011. <http://dx.doi.org/10.1364/OE.19.021345>.
- [GVF⁺20] M. Gambino, M. Veselý, M. Filez, R. Oord, D. Ferreira Sanchez, D. Grolimund, N. Nesterenko, D. Minoux, M. Maquet, F. Meirer, and B. M. Weckhuysen. “Nickel Poisoning of a Cracking Catalyst Unravelling by Single-Particle X-ray Fluorescence-Diffraction-Absorption Tomography”. *Angew. Chem. Int. Ed.*, **59**(10):3922–3927, 2020. <http://dx.doi.org/10.1002/anie.201914950>.
- [HLR17] R. Huang, K. Limburg, and M. Rohtla. “Quantitative X-ray fluorescence computed tomography for low-Z samples using an iterative absorption correction algorithm”. *AIP Advances*, **7**(5):055111, 2017. <http://dx.doi.org/10.1063/1.4983804>.
- [Kau87] L. Kaufman. “Implementing and Accelerating the EM Algorithm for Positron Emission Tomography”. *IEEE Trans. Med. Imaging*, **6**(1):37–51, 1987. <http://dx.doi.org/10.1109/TMI.1987.4307796>.
- [KS88] A. C. Kak and M. Slaney. *Principles of Computerized Tomographic Imaging*. IEEE PRESS, New York, 1988. <http://www.slaney.org/pct/pct-toc.html>.
- [LC84] K. Lange and R. Carson. “EM reconstruction algorithms for emission and transmission tomography”. *J. Comput. Assist. Tomogr.*, **8**(2):306–316, 1984.
- [Ler61] J. Leroux. “Method for Finding Mass-Absorption Coefficients by Empirical Equations and Graphs”. *Advances in X-ray Analysis*, **5**:153–160, 1961. <https://doi.org/10.1154/S037603080000152X>.
- [Lim12] A. Limaye. “Drishti: a volume exploration and presentation tool”. *Proc. SPIE*, **8506**(85060X), 2012. <http://dx.doi.org/10.1117/12.935640>.
- [LYQ⁺15] L. Long, H. Yang, X. Qing, Y. Ling-Tong, L. Li, F. Song-Lin, and F. Xiang-Qian. “Attenuation correction of L-shell X-ray fluorescence computed tomography imaging”. *Chinese Phys. C*, **39**(3):038203, 2015. <http://dx.doi.org/10.1088%2F1674-1137%2F39%2F3%2F038203>.
- [MMB⁺19] A. Mijovilovich, A. Mishra, D. Brückner, K. Spiers, E. Andresen, J. Garrevoet, G. Falkenberg, and H. Küpper. “MicroX-ray absorption near edge structure tomography reveals cell-specific changes of Zn ligands in leaves of turnip yellow mosaic virus infected plants”. *Spectrochim. Acta B*, **157**:53–62, 2019. <http://dx.doi.org/10.1016/j.sab.2019.05.005>.

- [PPK⁺14] M. Jake Pushie, I. J. Pickering, M. Korbas, M. J. Hackett, and G. N. George. “Elemental and Chemically Specific X-ray Fluorescence Imaging of Biological Systems”. *Chemical Reviews*, **114**(17):8499–8541, 2014. <http://dx.doi.org/10.1021/cr4007297>.
- [PRdAK18] M. S. Prasad, N. G. Rudraswami, A. A. de Araujo, and V. D. Khedekar. “Characterisation, Sources and Flux of Unmelted Micrometeorites on Earth During the Last 50,000 Years”. *Sci Rep*, **8**:8887, 2018. <http://dx.doi.org/10.1038/s41598-018-27158-x>.
- [RBV⁺06] P. J. La Rivière, D. M. Billmire, P. Vargas, M. L. Rivers, and S. R. Sutton. “Penalized-likelihood image reconstruction for x-ray fluorescence computed tomography”. *Optical Engineering*, **45**(7):077005, 2006. <http://dx.doi.org/10.1117/1.2227273>.
- [SBD⁺16] C. G. Schroer, C. Baumbach, R. Döhrmann, S. Hönig, R. Hoppe, M. Kahnt, J. Patommel, J. Reinhardt, D. Samberg, M. Scholz, A. Schropp, F. Seiboth, M. Seyrich, F. Wittwer, and G. Falkenberg. “Hard x-ray nanoprobe of beamline P06 at PETRA III”. *AIP Conference Proceedings*, **1741**(1):030007, 2016. <http://dx.doi.org/10.1063/1.4952830>.
- [SBF⁺10] C. G. Schroer, P. Boye, J. M. Feldkamp, J. Patommel, D. Samberg, A. Schropp, A. Schwab, S. Stephan, G. Falkenberg, G. Wellenreuther, and N. Reimers. “Hard X-ray nanoprobe at beamline P06 at PETRA III”. *Nucl. Instr. Meth. Phys. Res. A*, **616**(2-3):93–97, 2010. <http://dx.doi.org/10.1016/j.nima.2009.10.094>.
- [SBG⁺02] C. G. Schroer, B. Benner, T. F. Günzler, M. Kuhlmann, B. Lengeler, W. H. Schröder, A. J. Kuhn, A. S. Simionovici, A. Snigirev, and I. Snigireva. “High Resolution Element Mapping Inside Biological Samples using Fluorescence Microtomography”. *Proc. SPIE*, **4503**(230), 2002. <http://dx.doi.org/10.1117/12.452850>.
- [SBG⁺11] T. Schoonjans, A. Brunetti, B. Golosio, M. Sanchez del Rio, V. A. Solé, C. Ferrero, and L. Vincze. “The xraylib library for X-ray-matter interactions. Recent developments”. *Spectrochim. Acta B*, **66**(11):776–784, 2011. <https://doi.org/10.1016/j.sab.2011.09.011>.
- [Sch01] C. G. Schroer. “Reconstructing x-ray fluorescence microtomograms”. *Appl. Phys. Lett.*, **79**(12):1912–1915, 2001. <http://dx.doi.org/10.1063/1.1402643>.
- [SPC⁺07] V.A. Solé, E. Papillon, M. Cotte, Ph. Walter, and J. Susini. “A multiplatform code for the analysis of energy-dispersive X-ray fluorescence spectra”. *Spectrochim.*

- Acta B*, **62**(1):63–68, 2007. <http://dx.doi.org/10.1016/j.sab.2006.12.002>.
- [SV82] L. A. Shepp and Y. Vardi. “Maximum Likelihood Reconstruction for Emission Tomography”. *IEEE Trans. Med. Imaging*, **1**(2):113–122, 1982. <http://dx.doi.org/10.1109/TMI.1982.4307558>.
- [T⁺09] A. Thompson *et al.* *X-ray Data Booklet*. Lawrence Berkeley Laboratory, 2009. <http://cxro.lbl.gov/x-ray-data-booklet>.
- [UP18] S. Usman and A. Patil. “Radiation detector deadtime and pile up: A review of the status of science”. *Nuclear Engineering and Technology*, **50**(7):1006–1016, 2018. <https://doi.org/10.1016/j.net.2018.06.014>.
- [vdEdJS⁺20] A. van der Ent, M. D. de Jonge, K. M. Spiers, D. Brueckner, E. Montargès-Pelletier, G. Echevarria, X.-M. Wan, M. Lei, R. Mak, J. H. Lovett, and H. H. Harris. “Confocal Volumetric μ XRF and Fluorescence Computed μ -Tomography Reveals Arsenic Three-Dimensional Distribution within Intact *Pteris vittata* Fronds”. *Environmental Science & Technology*, **54**(2):745–757, 2020. <http://dx.doi.org/10.1021/acs.est.9b03878>.
- [vdESB⁺19] A. van der Ent, K. M. Spiers, D. Brueckner, G. Echevarria, M. G. M. Aarts, and E. Montargès-Pelletier. “Spatially-resolved localization and chemical speciation of nickel and zinc in *Noccaea tymphaea* and *Bornmuellera emarginata*”. *Metallomics*, **11**(12):2052–2065, 2019. <http://dx.doi.org/10.1039/c9mt00106a>.
- [VS18] N. R. Viganò and V. A. Solé. “Physically corrected forward operators for induced emission tomography: a simulation study”. *Meas. Sci. Technol.*, **29**(3):034005, 2018. <http://dx.doi.org/10.1088/1361-6501/aa9d54>.
- [YDD⁺14] Q. Yang, B. Deng, G. Du, H. Xie, G. Zhou, T. Xiao, and H. Xu. “X-ray fluorescence computed tomography with absorption correction for biomedical samples”. *X-Ray Spectrom.*, **43**:278–285, 2014. <http://dx.doi.org/10.1002/xrs.2550>.

Acknowledgments

At this point I want to acknowledge those who made this work possible.

First and foremost I would like to thank my *Doktorvater* Prof. Dr. Christian G. Schroer for supervising my PhD project, filling the role of first reviewer for my thesis and for being part of my examination commission. He took me into his group, not only for my PhD project but also for my master's project, and was always there to give scientific advice, even on busy days.

For his work as my mentor I would like to thank Dr. Gerald Falkenberg. He allowed me to be part of the P06 beamline team in all but name, enabling me to work at the beamline (including inhouse beamtime for my own reasearch), and gave valuable input during the writing of this thesis.

I would like to thank Jun.-Prof. Dr. Peter Modregger for being the second reviewer of my thesis and part of my examination commission.

For taking over the responsibility as leader of my examination commission I would like to thank Prof. Dr. Wolfgang J. Parak, especially because this was his first time filling this role as a professor of the University of Hamburg.

Furthermore, I would like to thank Prof. Dr. Florian Gruener and Prof. Dr. Daniela Pfannkuche for filling the last two slots and completing my examination commission.

Dr. Ir. Jan Garvoet and Dr. Stijn van Malderen deserve my thanks for their assistance at the beamline and their coding work. Jan's coding work is one of the things that keeps the beamline control of P06 running and Stijn's coding work was vital for the evaluation of the XRF data.

For introducing me to the topic of micrometeorites and providing the sample discussed in this thesis I would like to thank Dr. Andreas Schropp and Dr. Jenny Feige, respectively.

I would like to thank Vanessa Galbierz and Hendrik Lindemann for information on the technical side of the beamline as well as renderings of the beamline and scanning setup.

My office mates over the years, Maik Kahnt, Felix Wittwer, Martin Seyrich and Saba Alizadehfanaloo, deserve my thanks for creating a welcoming atmosphere in the office and interesting discussions.

In addition, I would like to thank all members of FS-PETRA and FS-P06 for accepting me into their groups and supporting me during my PhD project.

As science would not be possible without food on the table, I would also like to thank Prof. Dr. Axel Rosenhahn for funding the first years of my PhD project.

And last but not least I would like to thank my family for always supporting me.

I acknowledge DESY (Hamburg, Germany), a member of the Helmholtz Association HGF, for the provision of experimental facilities. Parts of this research were carried out at PETRA III beamline P06. Furthermore, this research was supported in part through the Maxwell computational resources operated at DESY and by core funding of the Helmholtz Imaging Platform (HIP), a platform of the Helmholtz Incubator on Information and Data Science.

Eidesstattliche Versicherung / Declaration on oath

Hiermit versichere ich an Eides statt, die vorliegende Dissertationsschrift selbst verfasst und keine anderen als die angegebenen Hilfsmittel und Quellen benutzt zu haben.

Die eingereichte schriftliche Fassung entspricht der auf dem elektronischen Speichermedium.

Die Dissertation wurde in der vorgelegten oder einer ähnlichen Form nicht schon einmal in einem früheren Promotionsverfahren angenommen oder als ungenügend beurteilt.

Ort, Datum

Unterschrift